

Ecole Doctorale Sciences Pour l'Ingénieur
Spécialité Mécanique, Génie Civil, Energétique, Matériaux

Université Lille 1 - Sciences et Technologies

Unité de Mécanique de Lille, EA 7512

Convection turbulente et changement de phase, avec applications à la modélisation des mares de fonte arctiques

Thèse de doctorat présentée par **Babak RABBANIPOUR ESFAHANI**

Soutenue publiquement le 23 Mars 2018 devant le jury composé de:

Rapporteurs	Dominique GOBIN	Directeur de recherche CNRS, Laboratoire EM2C, Paris
	Daniel HENRY	Directeur de recherche CNRS, LMFA, Université de Lyon
Examineurs	Anne SERGENT	MdC, LIMSI, Sorbonne Université
Invité	Martin VANCOPPENOLLE	Chercheur CNRS, LOCEAN-IPSL
Directeur de thèse	Mohamed-Najib OUARZAZI	PR, UML, Université de Lille
Co-encadrant	Enrico CALZAVARINI	MdC, UML, Université de Lille
	Silvia HIRATA	MdC, UML, Université de Lille

Doctoral School SPI – Sciences for Engineer
Mechanics, Civil Engineering, Energy, Materials

Lille University of Science and Technology

Lille Mechanics Unit, EA 7512

Turbulent convection and melting process with applications to sea ice melt ponds

PhD dissertation presented by **Babak RABBANIPOUR ESFAHANI**

Publicly defended in March 23rd, 2018 in the presence of the thesis jury members:

Reviewers	Dominique GOBIN Daniel HENRY	CNRS Research Director, EM2C, Paris CNRS Research Director, LMFA, University of Lyon
Examiners	Anne SERGENT	Assoc. Prof, LIMSI, Sorbonne University of Paris
Invited Director	Martin VANCOPPENOLLE Mohamed-Najib OUARAZI	CNRS Researcher, LOCEAN-IPSL Prof, ULM, University of Lille
Co-directors	Enrico CALZAVARINI Silvia HIRATA	Asst. Prof, ULM, University of Lille Asst. Prof, ULM, University of Lille

Abstract

Melting and solidification coupled with convective flows are fundamental processes in the geophysical context. Convective melting is thought to have played a major role in Earth's mantle formation and is commonly observed in magma chambers, lava lakes, and particularly the interest of this thesis, Arctic *melt-ponds*. All these systems are characterized by the presence of unsteady, chaotic and often turbulent flows. A key question related to these phenomena is the prediction of the evolution of the melting-rate, a quantity that is tightly connected to the heat-flux dynamics at the liquid-solid interface. This is, however, a complex problem because it couples the highly non-linear motion of fluid flow with a time evolving interface. Therefore in this regime, it is difficult to predict the exact dynamics, but what can be predicted is its average dynamics through scaling laws. In order to shed light on this process and in particular on its scaling laws, we study here the stages of the dynamics of a simplified model system.

This thesis begins with an overview of melt pond phenomenology and modeling from large to small scale. The idealized setup we consider, named convective melting system (CM), consists of a fluid layer heated from below and in contact with a solid-to-liquid melting interface on the top-side. Similar to the Rayleigh-Bénard (RB) system, for sufficiently large vertical temperature gaps a convective instability develops and the resulting flow exhibits a rich dynamics as the Rayleigh (Ra) number is increased, ultimately reaching a turbulent state. In the present case however, the interface melts at the pace of the local heat flux across the fluid layer, the resulting shape of the lead in turn modifies the organization of flow structures with a feedback on the heat transport.

We investigate such a model system by means of numerical tools. We perform Direct Numerical Simulations via an enthalpy based Lattice Boltzmann algorithm to address the long time dynamics, or equivalently the high Rayleigh number regime, both in two- and three-dimensional setups. We focus on the scaling of global quantities, Nusselt and Reynolds numbers, and on the characterization of geometrical properties of the melting interface.

We observe that the system self-organizes in convective cells that tend to have unit aspect-ratio and a vanishing corrugation as the convection intensity is increased. Furthermore, we show that the coupled convection and melting process only weakly enhances heat flux and the mixing in the system as compared to the RB setting. The observed differences in the 2D- and 3D-simulations follow similar trends as the ones already observed in the RB system and tend to vanish in the highly Rayleigh regime, beyond $Ra \sim 10^7$. Moreover, we show that the variation of the Stefan (St) number, which accounts for the material properties, has only a mild effect on the intensity and scaling of global quantities and on the geometrical features of the fluid-solid interface in the high- Ra regime.

As an extension to the CM system, two different setups are considered in this work. In the first configuration, we consider the effect of introducing a moving boundary, in or-



der to mimic wind effects on melt-ponds. We observe the onset of convection is delayed as the wall velocity increases. This observation is consistent with similar systems without melting condition, as the thermal Couette flow. Moreover, depending on the intensity of the wall velocity, the formation of convective rolls and consequently morphology of the solid-liquid interface undertakes significant changes. For the second configuration, we consider the effect of internally heating the CM system, representing bulk heating through solar radiation. Similar to the analysis of pure melting system, we consider heat budget and morphology of the solid-liquid interface.

Finally, we discuss possible implications of our study for more refined parametrization of melt-ponds in large-scale models and possible extensions of the current work.

Keywords: **Turbulent convection, Phase-change, Stefan problem, Melt ponds, Lattice Boltzmann method**



Résumé

La fusion et la solidification, couplées à des écoulements convectifs sont des processus fondamentaux dans le contexte géophysique, par exemple dans la formation des marées arctiques. Ce système se caractérise par la présence d'écoulements instationnaires, chaotiques et souvent turbulents. Ce travail est motivé par des observations indiquant une réduction de la glace de mer Arctique que le modèle global actuel n'était pas en mesure de prédire. Le but de ce travail est de fournir des informations sur les paramètres pertinents affectant la fusion/solidification dans les étangs de fonte des glaces de mer. La configuration idéalisée que nous considérerons consiste en une couche de fluide chauffée par le bas et en contact avec une interface de fusion solide-liquide du côté supérieur. Nous étudierons un tel système modèle grâce à des outils numériques. Nous effectuerons des simulations numériques directes par un algorithme Lattice Boltzmann basé sur l'enthalpie pour traiter la dynamique à long terme, ou de manière équivalente le régime à nombre élevé de Rayleigh, à la fois dans des configurations en deux et en trois dimensions. Nous montrerons que le processus de convection et de fusion couplé n'améliore que faiblement le flux de chaleur et le mélange dans le système par rapport au réglage de Rayleigh-Bénard. Nous considérerons l'effet de l'application de la vitesse sur la section liquide du système de fusion et l'effet de chauffage interne du système de fusion comme deux extensions au système de fusion.



Acknowledgements

Throughout these three years as a PhD student, there have been many people who have aided me in various ways. For this I am deeply grateful. I would have had a much harder time early on if *Kalyan Shrestha* had not spent many hours helping me to understand the lattice Boltzmann method. Similarly, my later work would have been much more difficult if not for the occasional comment from *Hamidreza Ardeshiri*. His deep insight and help has been invaluable to my personal life and my work.

There are many other researchers with whom I have had interesting and useful discussions on a wide variety of scientific topics. I would especially like to thank *Himani Garg*, *Jin Zhang*, *Xiaodan Cao*, *Sricharan Srinath*, and *Ilkay Solak*. Thanks to them, whose non-scientific aspects of companionship delighted my three years of working at L.M.L. Many thanks to *Jean Marc Foucaut*, *Jean-Philippe Laval* and *Thomas Gomez* who scientifically helped me understand fundamentals of fluid mechanics and turbulence by allowing me participate in their international master program.

I am grateful to *Mohamed-Najib Ouarzazi* and *Stefano Berti* for enlightening discussions, comments and suggestions in various occasions. Their deep insight has been invaluable to me and my work.

Finally, I would like to express all my gratitude to *Enrico Calzavarini* and *Silvia Hirata* who have not only been advisers any student could hope to have, but friends who supervised the present work with their kind supports in all the moments. I would like to thank them for being patient and for all the scientific discussions we had during the last three years.

To all of you: *Thank you.*

Hereby, I acknowledge the research leading to these results has received funding from the French National Agency for Research (ANR) under the grant SEAS (ANR-13-JS09-0010) and from European COST Action MP1305.

Babak Rabbanipour Esfahani
Lille, March 2018



Contents

Abstract	v
Résumé	vii
Acknowledgements	ix
Abbreviations	xv
Symbols	xvii
1 Introduction	1
1.1 Objectives of the present work	4
1.2 Structure of the present work	5
References	6
2 Overview on sea ice melt ponds in the Arctic	9
2.1 Albedo and melt-pond evolution	9
2.1.1 Melting processes on sea ice	11
2.2 Representing ponds in climate models	13
2.2.1 Large-scale models	13
2.2.2 Small scale models	19
2.3 Summary and open issues	20
References	21
3 Evolution equations for conduction, convection and phase-change	25
3.1 The mathematical model system	25
3.2 Conductive melting	27
3.2.1 One dimensional Stefan problem	28
3.2.2 The Stefan condition	29
3.2.3 One dimensional melting problem	31
3.2.4 Similarity Solution	31
3.3 Melting with an external moving boundary	33
3.3.1 Analytical solution for the velocity field	33
3.4 Rayleigh-Bénard convection	36
3.4.1 Governing equations	37
3.4.2 Non-dimensionalization	38
3.4.3 Nusselt number	39
3.4.4 Reynolds number	40
3.4.5 Scaling theories for global heat flux	40
3.4.6 Convection with a uniform volumetric heating	42



3.5	Natural convection coupled with phase-change	43
3.5.1	Enthalpy formulation for phase-change	43
3.5.2	Nusselt number in system melting	45
3.6	Summary	45
	References	45
4	Numerical simulation of convection coupled to melting process	49
4.1	The Lattice Boltzmann method	50
4.1.1	Lattice Boltzmann model	50
4.1.2	Advection-diffusion equation for the temperature field with the LB method	52
4.1.3	Boussinesq equation system with the LB method	53
4.1.4	Boundary conditions.	54
4.2	Validation	57
4.2.1	Melting in conductive condition	58
4.2.2	Rayleigh-Bénard convection	59
4.2.3	Conductive Rayleigh-Bénard system with internal heating.	60
4.2.4	Melting due to thermal convection.	61
4.3	Summary	62
	References	63
5	Convective melting system	67
5.1	Introduction	67
5.2	The horizontal convective melting system	68
5.2.1	Equations of motion for the convective melting system	68
5.3	Heat-flux	71
5.3.1	Global heat-flux balance	71
5.3.2	Scaling relations for the heat flux and melting rate	73
5.4	Discussion	74
5.5	Qualitative description of system dynamics	75
5.6	Scaling in the 2D system	76
5.7	Scaling in the 3D system	79
5.8	Morphology of the phase-change interface	82
5.9	Effect of Stefan number	86
5.10	Effect of aspect ratio	90
5.11	Conclusion	91
	References	92
6	Convective melting system with a moving boundary	95
6.1	Convective melting system with a moving boundary	95
6.1.1	Equation of motion for the phase-change problem: moving boundary formulation	95
6.2	Discussion	96
6.2.1	Results on global quantities	97
6.2.2	Morphology of the interface	102
6.3	Conclusion	105
	References	105



7	Convective melting with volumetric heat source	107
7.1	Convective melting system with volumetric heat source	109
7.1.1	Equations of motion	109
7.1.2	Global heat-flux balance	110
7.2	Discussion	111
7.2.1	Results on global quantities	113
7.2.2	Morphology of the interface	116
7.3	Conclusion	118
	References	119
8	Conclusion and perspectives	121
8.1	Future perspectives	125
	References	127
A	About the author	129



Abbreviations

DNS	D irect N umerical S imulation
LB	L attice B oltzmann
RB	R ayleigh B énard
LBM	L attice B oltzmann M ethod
BGK	B hatnagar G ross K rook
RBS	R ayleigh B énard S ystem
CM	C onvective M elting
NS	N avier- S tokes
RMS	R oot M ean S quare
LES	L arge E ddy S imulation
RANS	R eynolds A veraged N avier S tokes
FDM	F inite D ifference M ethod
FVM	F inite V olume M ethod
FEM	F inite E lement M ethod
PDE	P artial D ifferential E quation
FFT	F ast F ourier T ransform
IFFT	I nverse F ast F ourier T ransform
ODE	O rdinary D ifferential E quation
PDF	P robability D ensity F unction



Symbols

α	Absorption coefficient	m^{-1}
β	Volumetric thermal expansion coefficient	K^{-1}
Γ	Aspect ratio	
κ	Thermal diffusivity	m^2s^{-1}
Λ	Thermal conductivity	$\text{Wm}^{-1}\text{K}^{-1}$
μ	Dynamic viscosity	$\text{kg s}^{-1}\text{m}^{-1}$
ν	Kinematic viscosity	m^2s^{-1}
ϕ_l	Liquid fraction	
ρ	Mass density	kgm^{-3}
σ	Standard deviation	
c_p	Specific heat capacity	$\text{kgm}^2\text{K}^{-1}\text{s}^{-2}$
\mathcal{F}	Fourier operator	
\mathcal{F}^{-1}	Inverse Fourier operator	
\mathbf{g}	Gravitational acceleration	ms^{-2}
H_{max}	Total height of system	m
I_0	Irradiance	Wm^{-2}
$k_x \& k_y$	Wavenumbers	
L	Physical length scale	m
L_c	Correlation length	m
\mathcal{L}	Latent heat	kJkg^{-1}
p	Pressure	$\text{kgm}^{-1}\text{s}^{-2}$
q	Power per unit volume	Wm^{-3}
t	Time	s
T	Temperature	K
ΔT	Temperature difference	K
\mathbf{u}	velocity	ms^{-1}
u_{rms}	Field root mean square velocity	ms^{-1}
Pr	Prandtl number	
Ra	Rayleigh number	
Re	Reynolds number	
St	Stefan number	



*To my parents
and love of my life, Annemieke.*



1

Introduction

Since satellite observations started in 1979, the summer Arctic sea ice extent has declined by 12% per decade. As announced by the US National Snow and Ice Data Center (NSIDC), 2012 has marked the lowest on record. Arctic sea ice extent for December 2017 averaged 11.75 million square kilometers, the second lowest in the 1979 to 2017 satellite record. This was 1.09 million square kilometers below the 1981 to 2010 average and 280,000 square kilometers above the low-December-extent recorded in 2016 (Fig. 1.1). Moreover, the ice cover is also thinning, making it more vulnerable to warmer temperatures. Finally, the long-lived multi-year ice is progressively replaced by first-year ice due to the intensified summer melt. Most of the projections performed with Global Climate Models (GCMs) in the framework of the Intergovernmental Panel on Climate Change (IPCC), do not reliably predict the observed rapid sea ice retreat [1]. This shortcoming suggests a need for model improvements.

Global warming is intensified in polar regions mostly due to the albedo feedback mechanism [2]. *Albedo* is the measure of diffusive reflection of solar radiation out of the total solar radiation received by a body, for example a planetary body such as Earth. It is dimensionless and measured on a scale from zero (corresponding to a black body that absorbs all incident radiation) to one (corresponding to a body that reflects all incident radiation). When spring comes to the Arctic, the breakup of the cold winter ice sheets starts at the surface with the formation of melt ponds. These pools of melted snow and ice darken the surface of the ice, increasing the amount of solar energy the ice sheet absorbs and accelerating melt, a mechanism known as positive feedback of albedo.

The presently more prevalent first-year ice transmits more light to the upper ocean than multi-year ice due a larger pond coverage. Therefore, the melt rate beneath pond-covered ice can be 2 to 3 times greater than that of bare ice [3] and should be more intense today than in the past, due to the greater present pond coverage. The albedo of pond-covered ice (measured in the field) ranges from 0.1 to 0.5 (e.g. [4]), and is principally determined by the optical properties and electromagnetic properties of water (that absorbs much more than ice) and by the pond geometry (depth of water layer and its surface extension). These albedo values are much lower than bare ice and snow covered ice, which range from 0.52 to 0.87.



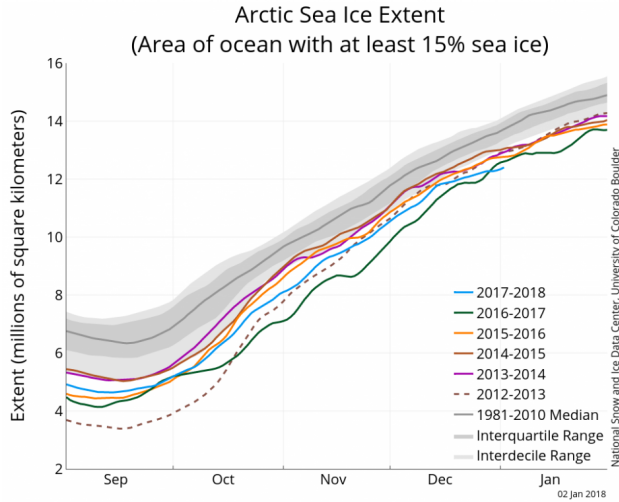


Figure 1.1 – The graph above shows Arctic sea ice extent as of January 2, 2018, along with daily ice extent data for five previous years. 2017 to 2018 is shown in blue, 2016 to 2017 in green, 2015 to 2016 in orange, 2014 to 2015 in brown, 2013 to 2014 in purple, and 2012 to 2013 in dotted brown.

The 1981 to 2010 median is in dark gray. The gray areas around the median line show the interquartile and interdecile ranges of the data. Credit: National Snow and Ice Data Center, University of Colorado Boulder

A good estimation of the area of the sea ice surface covered with melt ponds is needed to determine the large-scale albedo of the ice cover. However, the fractional pond coverage is a highly variable quantity, with values ranging from 5 to 80% depending upon various factors: time elapsed since the beginning of the melt season, surface roughness, snow cover, floe size, among others. In the melt season, melt ponds on average cover up to 60% of the sea ice surface [3].

Several field experiments and ship observations have been conducted on different locations in the Arctic Ocean to study albedo and spectral behaviour of melt ponds, as well as distribution and size of the ponds. Field observations, such as the Surface Heat Budget of the Arctic (SHEBA), provided information on how ponds form and evolve throughout the melt season, until they freeze over in autumn. Melt ponds are typically 5 to 10m wide and 15 to 50cm deep. The evolution of the melt pond cover, even on a particular floe, is highly variable since it is controlled by a number of competing factors. Based upon observations, Eicken *et al.* [5] divided the evolution of the melt pond cover into four main stages, revised by Polashenski *et al.* [6]:

- Ponds initially quickly expand following melt onset due to the rapid accumulation of snow meltwater in existing depressions and cracks. Meltwater accumulation is promoted by the generally low sea ice floe-scale permeability.
- Pond coverage then decreases due to drainage. This occurs for two reasons: an increase in floe-scale ice permeability due to the formation of meltwater chan-

nels; and an increasing static pressure head due to the rising ponds, promoted by continued meltwater production. The pond areal decrease slows down as the meltwater approaches sea level and reduces the pressure head.

- A second, slower increase in pond fraction occurs due to water supply from below. This occurs when the decrease in ice freeboard due to sea ice melt exposes new topographic local minima to water from below.
- Finally, melt ponds quickly disappear due to freezing at their top in early fall.

Observations indicate that accurate representation of the ice-albedo feedback is highly dependent on predicting the melt pond coverage and applying the correct pond albedo for each phase of the pond evolution. GCM simulations are still not able to properly represent melt ponds on the surface of sea ice. A comparison of observed pond coverage and GCM pond parametrizations is shown in Figure 1.2.

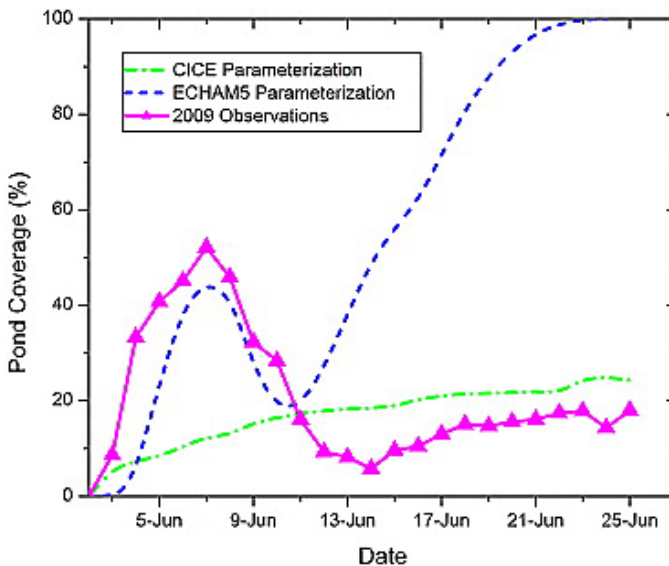


Figure 1.2 – Comparison of observed pond coverage and GCM pond parameterizations, taken from [7].

One example of a large-scale sea ice model is the Louvain-la-Neuve sea ice model (LIM)¹, designed for climate studies and operational oceanography. It is coupled to the ocean general circulation model OPA (Ocean Parallélisé) and is part of NEMO². LIM is used in several GCMs contributing to the assessment reports of the IPCC³ (Intergovernmental Panel on Climate Change) and in the operational oceanography system MERCA-

¹<http://www.climate.be/lim/>

²<http://www.nemo-ocean.eu/>

³<http://www.ipcc.ch/>

TOR⁴. A one-dimensional version (LIM1D⁵) has also been developed for process studies. LIM3 [8] is the most recent version of LIM. LIM model is able to reproduce the large-scale evolution of sea ice characteristics in reasonable agreement with field observations. However, presently the effect of melt ponds is not accounted for in LIM, and there are ongoing attempts to include such a parametrization.

Ensuring realistic prediction of albedo requires the incorporation of the mechanisms that drive pond coverage into models. A substantial effort is already being undertaken to do this by improving both small and medium scale models of melt pond coverage⁶ and incorporating explicit melt pond parameterizations into albedo calculations of GCMs [9]. In the absence of basin wide pond observations and long-term data sets, supporting these efforts to create computationally efficient, yet physically representative models, requires further advances in our understanding of the small-scale mechanisms driving the seasonal evolution of melt ponds.

1.1. Objectives of the present work

Features related to water ponds forming over melted ice are too small to be directly accounted for in large-scale sea ice and global climate models. How does the heat transfer occur in the ponds and to what an extent is fluid-dynamics involved into the process? How does the melt progresses on the bottom and on the lateral walls of the ponds? How does the topography of the ponds, their surface and depth, evolve in the course of the summer season? All the above questions have been overlooked in the present models. Presently, the main challenge in sea ice climate science is to physically improve the models in order to refine their predictive power.

This thesis, based on a funding from Agence Nationale de la Recherche (ANR), addresses the problem of the growth process of ice melt ponds in the Arctic during the summer season by focusing on the small-scale (~ few meters) mechanisms controlling the evolution of the basin topography of a single melt pond. In particular we study the phenomenology of the thermal convective flow in the pond, which is known unsteady or even turbulent [10], and its interaction with the phase-change mechanisms at the pond boundaries. The goal of the funded project is to reach a sound understanding on how fluid dynamics and phase-change processes contribute in determining the pond growth in order to provide useful guidelines for parametrizations in large-scale ice models.

The overall aim of the present thesis work is to propose a more realistic, physically-based model for the evolution of a melt pond. Such small-scale model, based on the conservation laws of fluid mechanics, will allow us to investigate the evolution of pond shape and size.

Previous studies considering melt ponds either neglect the turbulent convection of water in the pond, or make simplifying approximations in order to calculate average fluxes and/or melt rates. To the author's knowledge, this is the first study which adopts direct numerical simulation of a melt pond representing convection and phase-change within the ponds. Furthermore, in contrast with the large majority of the available stud-

⁴<http://www.mercator-ocean.fr/>

⁵<http://www.elic.ucl.ac.be/lim/index.php?id=50/>

⁶Reader is advised to refer to chapter 2 for the information about the existing models.

ies, a three-dimensional melt pond is considered.

Some intermediate goals are described below. We aim at providing information on the relevant parameters affecting the melting/solidification in sea ice melt ponds.

- Investigation of internal dynamics of melt-pond and the ice topography by considering two- and three-dimensional direct numerical simulation of melting system.
- Investigation of the influence of wind stress on the dynamics of melt-pond and the morphology of solid-liquid interface.
- Investigation of the influence of solar heat fluxes and better understanding of the transport of solar heat within melt ponds.

1.2. Structure of the present work

In Chapter 2, the phenomenology of melt pond will be described, together with the most used models for these phenomena, which we denote as state-of-the-art on melt pond modeling. Most of the models, presented in this chapter, address the distribution of melt-pond and its effect on total albedo in large scale. However, particular interests of this thesis are the aspect related to the internal dynamics of melt-ponds, in other words the processes connected to heat transfer through a fluid layer and the phase change process of the bottom of ponds.

The process of melting, from internal dynamics point of view, undertakes two stages of conduction and convection. In Chapter 3 we address the mathematical aspects of melting system with different configurations. This chapter starts with describing the mathematical equation of melting under the effect of thermal conduction, which is known as the Stefan problem [11]. The analytical solution for the Stefan problem is known and is described in detail in first part of the Chapter 3. The mathematical solution of the Stefan problem is a good starting point for validation of numerical computation, which is why we start our discussion with relatively simple case of conductive melting.

We continue the discussion of conductive melting by applying one more constraint on the flow: a moving boundary. A moving boundary in the configuration of melt pond can be seen as having wind draft on the water-air boundary (top of melt pond). Similar to merely conductive melting, solutions of melting system couple with moving boundary in conductive regime is also analytically computable, and can be used to validate more complicated numerical solutions.

When the depth of liquid layer is large enough, the buoyancy force plays distinct role in the internal dynamics of melting system. Due to density differences, that stems from temperature differences of near top warm water and cold water near the ice, the liquid part of the melting system shows convection. Through this convective behaviour, the heat-budget exchange in the liquid part will increase and more heat will reach the icy bottom of the melt pond. Consequently, one can expect difference in the rate of melting in convective regime.

Due to the nature of equations describing the system of melting, analytical solution for the convective melting system does not exist. However, one can estimate the solution through numerical simulations. Consequently, in order to step in the direct numerical

simulation, we continue the discussion of the chapter 3 by introducing the governing equations of system of melting.

In order to investigate the dynamics of convective melting system, numerical tool is needed. Thus, in Chapter 4, we describe the Lattice Boltzmann method, which is used in the direct numerical simulations performed in the present work. We chose the Lattice Boltzmann method for several reasons. First of all it is relatively easier to implement in parallel environment, which makes it much time-efficient for our large computation. Secondly, there are well-known methods to implement simulation of phase-change (solid-liquid interface) which are suitable with the Lattice Boltzmann method.

The results of simulations in two- and three-dimensional systems are presented and discussed in Chapter 5. Initially, we qualitatively describe the dynamics of system, and interpret and rationalize the observed trends in the scaling of the global quantities, such as Nusselt and Reynolds number. We specialize the discussion on the dimensional effect by analyzing the morphology of the melting front. Moreover, the effect of the Stefan control parameter on the rate of melting is studied. Finally, we study the effect of aspect ratio on the dynamical behaviour of system of melting.

In order to complete the discussion about melting system, we process in 6 and 7 with two different setups that are common in the process of melting in the Arctic; effect of moving boundary (shear velocity) and volumetric bulk heating.

In Chapter 6, we address the behaviour of two-dimensional system of melting with existence of moving boundary, which represents the effect of wind draft on Arctic melt-pond. Similar to Chapter 5, we try to rationalize the behaviour of scaling of global parameters for different intensity of wall velocities, which we address by properly specified dimensionless parameter. Moreover, we discuss the morphology of solid-liquid interface and its dimensional effect on the dynamics of melting-system coupled with moving boundary.

In Chapter 7, we investigate the two-dimensional system of melting heated internally through volumetric bulk heating, which can be seen as a simple modeling of warming the system by radiation. As the solar radiation hits the melted pond, it penetrates the surface of the pond. Therefore, through gradual absorption of radiation the liquid layer warms up internally. Similar to the trend of previous chapters, we interpret the dynamics of the system by considering scaling of global parameters for different intensity of volumetric heating. Finally, we address the morphology of the interface and its behaviour with existence of bulk-heating in the system of melting.

Finally, in Chapter 8, we conclude the present work by critically reviewing the results of the Chapters 5, 6 and 7 thoroughly, and state future prospective.

References

- [1] J. C. Stroeve, M. C. Serreze, M. M. Holland, J. E. Kay, J. Malanik, and A. P. Barrett, *The arctic's rapidly shrinking sea ice cover: a research synthesis*, Climatic Change **110**, 1005 (2012).
- [2] G. A. Meehl, T. F. Stocker, W. D. Collins, P. Friedlingstein, T. Gaye, J. M. Gregory, A. Kitoh, R. Knutti, J. M. Murphy, A. Noda, *et al.*, *Global climate projections*, (Cambridge, UK, Cambridge University Press, 2007).

- [3] F. Fetterer and N. Untersteiner, *Observations of melt ponds on arctic sea ice*, Journal of Geophysical Research: Oceans **103**, 24821 (1998).
- [4] T. C. Grenfell and G. A. Maykut, *The optical properties of ice and snow in the arctic basin*, Journal of Glaciology **18**, 445 (1977).
- [5] H. Eicken, H. Krouse, D. Kadko, and D. Perovich, *Tracer studies of pathways and rates of meltwater transport through arctic summer sea ice*, Journal of Geophysical Research: Oceans **107** (2002).
- [6] C. Polashenski, D. K. Perovich, and Z. Courville, *The mechanisms of sea ice melt pond formation and evolution*, Journal of Geophysical Research **117** (2012), doi:10.1029/2011JC007231.
- [7] D. K. Perovich and C. Polashenski, *Albedo evolution of seasonal arctic sea ice*, Geophysical Research Letters **39** (2012).
- [8] M. Vancoppenolle, T. Fichefet, H. Goosse, S. Bouillon, G. Madec, and M. A. M. Maqueda, *Simulating the mass balance and salinity of Arctic and Antarctic sea ice. 1. model description and validation*, Ocean Modelling **27**, 33 (2009).
- [9] D. Flocco, D. L. Feltham, and A. K. Turner, *Incorporation of a physically based melt pond scheme into the sea ice component of a climate model*, Journal of Geophysical Research: Oceans **115** (2010).
- [10] P. D. Taylor and D. L. Feltham, *A model of melt pond evolution on sea ice*, Journal of Geophysical Research: Oceans **109**, (2004), c12007.
- [11] J. Stefan, *Über die theorie der eisbildung, insbesondere über die eisbildung im polarmeere*, Annalen der Physik **278**, 269 (1891).



2

Overview on sea ice melt ponds in the Arctic

Due to the dynamic nature of the ocean, sea ice does not simply grow and melt in a single place. Instead, sea ice is constantly moving and changing location. One way of investigating the behaviour of sea ice and the process of melting is through modeling.

In the simplest sense, when the temperature of the ocean reaches the freezing point, ice begins to grow [1]. When the temperature rises above the freezing point, ice begins to melt. In reality, however, the amount and rates of growth and melt depend on the way heat is exchanged within the sea ice, as well as between the top (ice-atmosphere) and bottom (ice-ocean) of the ice. In the present chapter, we look into phenomenology of melt-ponds, and the efforts that have been made to scientifically model the process of melting in melt-pond, and quantify distribution of melt-ponds on the Arctic sea-ice.

2.1. Albedo and melt-pond evolution

Sea ice is a composite of small fractionated areas of melt ponds, leads, snow fields, and ridges on a scale of meters over tens of meters to hundreds of meters. This results in a very inhomogeneous surface (see Fig. 2.1). Additionally, sea ice is composed of first-year and multi-year ice. Multi-year ice has survived at least one melt season.

The optical properties of ice and snow are a strong function of the wavelength of the incident solar radiation as shown in Fig.2.2. Highest spectral albedo values (> 0.9) appear in short wavelength ranges from 400 to 600nm for dry snow. The spectral albedo decreases toward longer wavelengths at a rate which seems to be related to the liquid–water content of the surface layer [2]. At 500nm melt ponds have albedo values that can range between 0.6 for young and shallow ponds and 0.25 for matured ponds on multi-year ice. The variety of albedo values for ponds is caused by differences in depths and underlying surfaces (see Figs. 2.3).

The albedo is correlated to the amount of air bubbles and brine¹ inclusions in the

¹When frazil ice crystals form, salt accumulates into droplets called brine, which are typically expelled back into the ocean. This raises the salinity of the near-surface water. Some brine droplets become trapped in pockets between the ice crystals.





Figure 2.1 – Arctic sea ice surface covered with melt ponds displaying various characteristics. The photo was taken from a helicopter during the Polarstern cruise ARK-XXII/2 in 2007. Photo: Stefan Kern

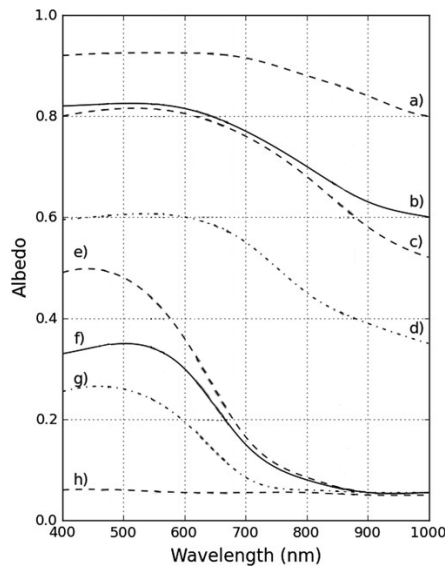


Figure 2.2 – Spectral albedo values for different surface types on Arctic sea ice: (a) snow-covered ice (dry snow), (b) cold bare ice, (c) wet snow, (d) melting first year ice, (e) young melt pond, (f) and (g) two types of mature melt ponds, and (h) open water. The figure is taken from T.Grenfell *et al.* [2] with some modifications.

sea ice. Hence, we can distinguish between albedo values of first-year ice and multi-year ice [3] the albedo of first-year ice is generally higher than the albedo of multi-year ice.

In literature many spectral and total albedo values for different surface types are



Figure 2.3 – Arctic sea ice surface covered with light blue shallow melt ponds (black star) and dark color deep melt ponds (white star). This photo shows a temporal ice station on a floe for measuring ice thickness. The photo is melt ponds on Arctic sea ice, copyright NASA Goddard Space Flight Center

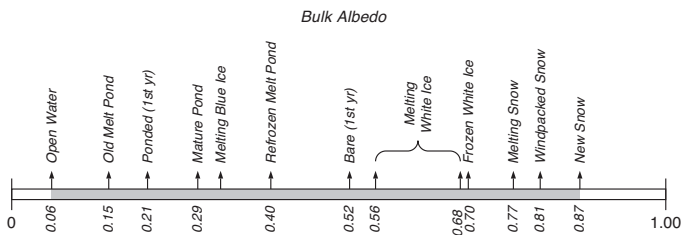


Figure 2.4 – Wavelength-integrated albedos for different surface types on Arctic sea ice.[3]

given [2–7]. Figure 2.4 shows some total albedo values published by Perovich [3]. The values are ranging from 0.06 for open water over 0.29 for mature melt ponds to 0.87 for new snow.

2.1.1.1. Melting processes on sea ice

To understand the evolution of sea ice throughout the melting season, it is necessary to distinguish between five distinct phases in the albedo evolution: dry snow, melting snow, pond formation, pond evolution, and refreezing [8].

In winter, most of the ice surface is covered with a dry snow layer of variable depth, building a more or less homogeneous surface with a high total albedo between 0.8 and 0.9 [8]. With onset of the summer melt season, the sea ice cover is subject to profound changes in its physical state and optical properties. The point in time when the melting process begins, strongly depends on the amount of solar energy absorbed before and during the melt season. It should be noted that early melt onset allows an earlier devel-

opment of open water areas, which then again enhance the ice-albedo feedback [9]. A trend to an earlier melt onset and a later freeze-up date in the entire Arctic region for the last three decades is described in literature [10]. The resulting longer melting periods are again a positive factor to the ice-albedo feedback mechanism.

Starting in April in sub-Arctic regions, dry snow wettens and begins to melt. Snow grains² transform and grain size generally increases [11]. Even these first melting processes can reduce the albedo of snowy surfaces by about 10 ~ 20%.

Snow melting processes depend on the properties of the snow cover, mainly on the snow depth. The variability of Arctic snow cover depth ranges from none to several meters in leeward sides of ridges or other obstacles. In the Central Arctic, snow cover usually disappears by the end of June [12]. Melt water of snow and ice accumulates in surface depressions and other surface deformation features. Compared to the much more irregular surface topography of multi-year ice; plane and flat surfaces of first-year ice have the potential to host large and extended melt pond areas [12, 13]. They can reach a coverage of over 50% of the total sea ice area [11]. On a flat topography of first-year level ice and in an early melt stage; the melt pond fraction can even rise up to 90% [14]. As melting develops, pond water drains through porous ice and cracks [15]. The pond properties and distribution on multi-year ice are described as smaller, deeper, and more numerous than on first-year ice [16].

The heat transfer due to convection in water exceeds the one of ice. Additionally, the lower albedo of ponded ice allows a higher penetration of heat into the ice. Both factors yield to a two to three times higher melt rate beneath ponds compared to the melt rate of bare ice [12]. Hence, the ponds deepen and can even melt through the ice layer. With the increasing depth of the ponds, also the diameter decreases [12]. On the one hand, spectral as well as total albedo of bare ice are fairly constant during the melting period. On the other hand, albedo of ponded ice depends on the pond depth and varies throughout the melting period [4].

Melt ponds are nearly salt free and the density maximum of the ponded water lies well above the freezing point [12]. Consequently, radiative heating favors convection within the pond: due to the density anomalies of water, the warmer water will sink down and thus causes further melting. Convection and mixing of the water is additionally enhanced by wind [15]. In late summer, melt ponds tend to melt down to sea level and drain towards the ocean.

Mature ponds are effective traps for the first drifting snow. Through the capillar effect, the water level of the pond rises. Therefore, it is less likely that this particular area will be pond covered in the next melting season [12]. Freeze-up starts in late August or early September, caused by low air temperatures. This results in a decreasing melt pond fraction. A snowfall event after freeze-up will cover the melt ponds, resulting in a higher surface albedo. The process of formation of melt-ponds is summarized in Fig (2.5).

The large inter-annual variability of the melt pond coverage can be caused by several factors: year-to-year variations of weather (mainly clouds and radiation), amount of melt water availability from snow, variable surface topography, floe size distribution,

²Snow grains are a form of precipitation. Snow grains are characterized as very small (< 1mm), white, opaque grains of ice that are fairly flat or elongated. Unlike snow pellets, snow grains do not bounce or break up on impact.

and their effect on runoff-pattern [12, 17].

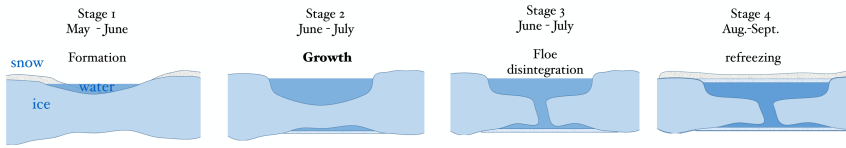


Figure 2.5 – Summary of melting and refreezing cycle of melt ponds in Arctic in one snapshot.

2.2. Representing ponds in climate models

In this section, we review most used models introduced over the last two decades. There was no pond parameterization in the early sea-ice thermodynamic models [18, 19]. However, observation of rapid reduction of summer Arctic sea ice suggested dynamic effects of melt ponds in the rate of melting of sea-ice.

The models, presented here, are described briefly together with the methods used to model melt ponds. In order to complete the discussion, we conclude by describing strengths and weaknesses of each model. These models are mainly about distribution of melt ponds, and internal dynamics of melt pond has been rarely taken into account. The order of introduction of models is from large-scale models to small-scale ones, and finally the models describing dynamics of single melt pond.

2.2.1. Large-scale models

Taylor and Feltham: Melt pond model

Taylor and Feltham [20] introduced a one-dimensional, thermodynamic melt-pond model that is based on two-stream radiation model³ instead of commonly used Beer-Lambert law⁴ representation of radiative transmission in sea ice. This model is advantageous in that the albedo can be calculated from the optical properties and ice thickness, whereas for Beer's law formulations, albedo is specified as an external parameter.

In the presence of melt ponds, a parameterization is used to simulate the variation of optical properties caused by morphological changes to the sea ice during summer. The governing equation for temperature is based upon the equation describing conservation of heat in a mushy layer. Mushy layers describe binary alloys, and consist of a solid matrix surrounded by its melt. For sea ice the solid matrix is composed of effectively pure ice, and the melt is brine.

The melt-pond model is primarily focused on Arctic sea ice, because the forcing data describe Arctic conditions; however, it is also applicable to melt ponds in the Antarctic.

³Two-stream radiation model allows albedo to be determined from bulk optical properties, and a parameterization of the summertime evolution of optical properties.

⁴The Beer-Lambert law is the linear relationship between absorbance and concentration of an absorbing species. The general Beer-Lambert law is usually written as $A = a(\lambda)bc$, where A is the measured absorbance, $a(\lambda)$ is a wavelength-dependent absorptivity coefficient, b is the path length, and c is the analyte concentration.

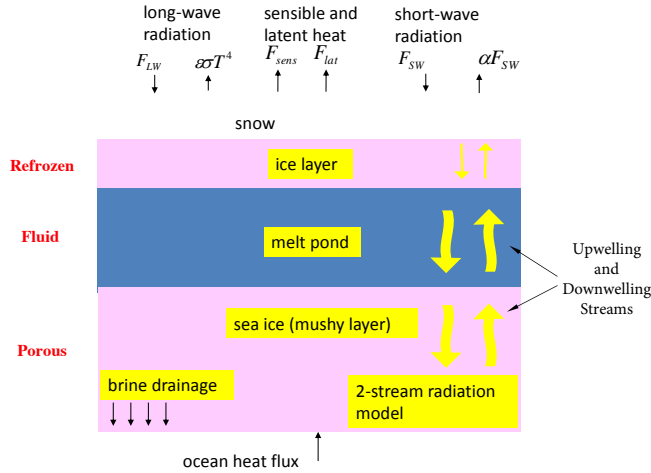


Figure 2.6 – One-dimensional melt pond-sea ice model of Taylor and Feltham [20]

With some straightforward modifications, the model could also be applied to other geophysical surface melt processes such as surface melting of glaciers.

As shown in Fig. 2.6, the model uses a three-layer, two-stream radiation model following Perovich [21], where the layers correspond to the melt pond, underlying sea ice and (where it exists) a layer of refrozen sea ice on top of the melt pond. The two-stream radiation model describes the radiation field in terms of an upwelling and downwelling stream.

The advantage of this model is that albedo can be explicitly determined, although it suffers from the assumption that the instantaneous radiation is uniform and scattering is isotropic. However Taylor and Feltham argue that as during summer, there is a high percentage of cloud cover [22], thus the assumption of diffuse incident radiation is approximately valid [21].

For computational convenience this model does not use spectral variation of the solar radiation or vertical variation of the optical properties in each layer, and it parameterizes the optical properties in the presence of melt ponds to obtain more accurate summertime temporal variation of albedo. Using wavelength integrated properties should not significantly affect the qualitative results, since most of the radiative energy in the sea ice is absorbed near the surface and this can be well represented using a single-band model [23].

This model consists of many features; for instance, heat transport within sea ice, melt pond and internal region, and snow layer, and finally drainage of ponds. However, the problem with this model is considering constant rate of melting for ice (in which the solid-liquid interface grows with a constant velocity), and independence of liquid layer height.

Melt ponds evolution coupled with CICE model

The Los Alamos CICE⁵ model is based on sea ice conditions and topology of the surface sea ice and was introduced by Flocco *et al* [24]. When meltwater forms due to snow and surface ice melt, it runs downhill under the influence of gravity. Thus, the topography of the ice cover plays a crucial role in determining the melt pond cover (e.g., [13, 25, 26]). CICE uses a discretized ice thickness distribution function [27] with five ice categories in the reference configuration. In this model it is assumed that each sea ice thickness category is in hydrostatic equilibrium at the beginning of the melt season, so that the sea ice thickness distribution function can be split into a surface height and basal depth distribution. For melt pond parameterization, the model calculates the position of sea level assuming that the ice in the whole grid cell is rigid and in hydrostatic equilibrium. The principle for meltwater distribution within a given grid cell and time step is, then, to take the volume of meltwater and cover the ice thickness categories in order of increasing surface height [28].

In general, the climatology of the reference CICE simulation with this melt pond scheme is in good agreement with observed ice extent and concentration and in reasonable agreement with observed ice thickness. The largest discrepancies occur in the Fram Strait, where the ice is too thin and drifts too fast, and in the Barents Sea. But these regions are of minor importance for studying the impact of melt ponds.

The impact of this melt pond scheme can be understood through comparison with three different melt pond approaches. First, artificially pond area and volume is set to zero. Second, this model applies the CCSM3 (Community Climate System Model [29]) radiation scheme instead of the Delta-Eddington radiation scheme [30]. Melt ponds are not explicitly accounted for, but the albedo is adjusted to observations (e.g., SHEBA experiment [31]) that include ponds. Third, this model applies the semi-empirical Bailey scheme [32] in which pond area and depth are parameterized as a function of the volume of meltwater and the change of meltwater volume as a function of surface temperature [28].

Apart from effectiveness of this model on well predicting the behaviour of Arctic sea-ice, this model does not deal with physical behaviour of ponds, and therefore, further investigation for understanding the dynamics of ponds is needed.

Lüthje: Modeling sea ice ponds

Lüthje *et al.* [25] developed a mathematical model to help understand the relative importance of melting and drainage processes to the summer evolution of the sea-ice cover. Different topographies, unponded ice melt rates, melt rates beneath melt ponds, vertical drainage rates, and horizontal permeabilities were tested. Despite the simplicity of the model physics, the model is able to quantitatively capture the main features of melt-pond formation, spreading and drainage.

⁵The Los Alamos sea ice model (CICE) is the result of an effort to develop a computationally efficient sea ice component for use in fully coupled, atmosphere-ice-ocean-land global circulation models, and it was originally developed to be compatible with the Parallel Ocean Program (POP). The name CICE is derived from "sea ice" and further information about it can be found at <http://oceans11.lanl.gov/trac/CICE>

The model consists of a volume element containing part of the surface of the sea-ice cover. The volume element is in the shape of a square prism with horizontal edges parallel to the axes of a Cartesian coordinate system fixed in space. The upper surface of the sea ice is given with respect to a fixed plane (for instance $z = 0$) and the depth of the layer of meltwater on top of the sea ice is denoted initially.

Initially, the surface topography is given together with the depth of the sea ice. The surface of the melt pond will lower after a time interval owing to vertical seepage, and the upper surface of the sea ice will lower owing to melting. The horizontal fluxes of meltwater into or out of the volume element per unit cross-sectional area are measured and used to compute volumetric changes of simulated melt ponds. As vertical seepage occurs more rapidly than horizontal redistribution through the surface layer, in each time step of the numerical calculations, the model apply the horizontal flux of meltwater into, or out of, a grid cell only if there is meltwater left after vertical seepage has taken place.

Calculations using their model give new insight into processes important for melt pond development. In particular, topography, vertical seepage rate, and unponded ice melt rate turned out to be the most important unknowns in determining the total summer-time surface ablation of sea ice. However, the treatment of meltwater flow was relatively crude and the model does not explicitly treat a snow cover. The role of snow and the importance of hydrodynamic processes to determining melt pond evolution is described by Eicken *et al.* [13, 15]. On this basis, one can speculate about the typical role of snow in a model of melt pond evolution. In particular, as the snow cover melts before the ice beneath it, the distribution of snow will largely determine the initial source of meltwater at the beginning of the melt season. Since, at this time, the sea ice is relatively cold and therefore relatively impermeable, one would expect lateral spreading of melt ponds to dominate vertical drainage into the underlying ocean. This is especially true of flatter, first-year sea ice as the meltwater is not trapped in depressions. The lateral spread of melt ponds might be expected to lead to enhanced melt at the peak in solar radiation, leading to entire melt through of sea ice in places, draining meltwater from a surrounding catchment area. The net effect of this may well be to reduce total ablation as predicted by this model.

Although, this model considers the drainage of melt pond in the process of formation, however, the dynamics of melt pond is not taken into account. Moreover, the model can simulate physical area of order 100 meters which compared to the area of Arctic sea ice is quite small.

Continuum model of melt pond evolution

This model is chosen to determine a model of the melt pond cover through a consideration of the physical processes that have been observed to determine pond evolution [33]. It make use of the sea ice thickness distribution function of Thorndike *et al.* [27], which was in use until recently in the latest generation of climate models, for example, HadGEM (the UK climate model), the Community Climate System Model (CCSM) at the US National Center for Atmospheric Research, and the Los Alamos CICE sea ice model component.

In the sea ice component of climate models, the thickness distribution function is

discretized, so that the area fractions of a small number of thickness classes are calculated and the evolution equation is solved in stages, using operator decomposition [34]. When solving the thermodynamic part of the evolution equation, the presence of melt ponds on the ice should be taken into account because the melt ponds significantly increase the melting rate of the ice they cover during the melt season and provide a store of latent heat that retards freezing during fall and winter.

The basic continuum hypothesis, in this model, is that within the horizontal grid cell of a sea ice model, ice of varying thickness is distributed uniformly, with relative abundance determined by the thickness distribution function. In particular, ice with different surface heights are distributed uniformly with relative abundance. This model uses the surface height distribution function to determine the redistribution of meltwater: at the beginning of a time step in numerical model, meltwater is generated and, at the end of the same time step, this meltwater is distributed so that it first covers ice of lowest surface height, and subsequently covers ice of increasing surface height. The meltwater is distributed such that the pond surface height is the same on all pond-covered surface ice height classes. Since the hypothesis is that sea ice of different surface heights are distributed uniformly over the grid cell, the meltwater does not need to travel far horizontally in order to accumulate on the lower ice surface.

One of the drawbacks of this model is the inability to explicitly model horizontal transport of meltwater upon or within sea ice in the model because generally the topography of the ice surface is unknown. For the same reason, this model is unable to distinguish between one large pond or a collection of ponds with the same total area and volume.

Another disadvantage of this model is that it does not explicitly treat the heat balance in the model. However, it uses a simple parameterization for the melting rate of ponded ice, with constant surface melting rate for bare ice and constant basal melting rate. These assumptions were made to simplify the calculations and isolate the physics of the pond formation and evolution.

Using this model, calculations have revealed that during the early part of the melt season, the pond coverage is dominated by snowmelt and accumulation of water with a positive hydraulic head. However, by about day 10 into the simulation, the ice cover becomes sufficiently porous that the pond surface drains to sea level within a few hours.

The model is based on many necessary assumptions. However, the model provides a realistic simulation of the fraction of the ice surface covered melt-ponds and maximum pond depth.

Ising model for melt

To address the fundamental problem of the evolution of the melt ponds in polar climate science, this model introduces a two dimensional random field Ising model ⁶ for melt

⁶The Ising model, named after the physicist Ernst Ising, is a mathematical model of ferromagnetism in statistical mechanics. The model consists of discrete variables that represent magnetic dipole moments of atomic spins that can be in one of two states (+1 or -1). The spins are arranged in a graph, usually a lattice, allowing each spin to interact with its neighbors. The model allows the identification of phase transitions, as a simplified model of reality. The two-dimensional square-lattice Ising model is one of the simplest statistical models to show a phase

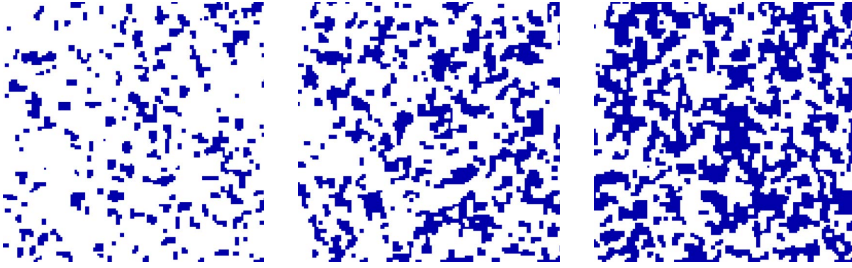


Figure 2.7 – Melt ponds as metastable islands of like spins in a random field Ising model. [35]

ponds [35]. The ponds are identified as metastable states [36–38] of the system, where the binary spin variable corresponds to the presence of melt water or ice on the sea ice surface. With only a minimal set of physical parameters, the model predictions agree very closely with observed power law scaling of the pond size distribution [8] and critical length scale where melt ponds undergo a transition in fractal geometry [39].

To describe nontrivial spin clustering at zero temperature, the H_i and/or J_{ij} are chosen as random variables; the resulting models are collectively known as disordered Ising models [40]. In particular, one recovers the classical random field Ising model (RFIM) if the H_i are independent random variables and the $J_{ij} = J$ are constant. At zero temperature, the system is usually assumed to follow Glauber single spin-flip dynamics [41] at each update step, the flip is accepted if \mathcal{H} decreases and rejected if \mathcal{H} increases. The system eventually converges to a local minimum of \mathcal{H} , known as a metastable state.

Metastable states are especially relevant to physical systems near phase transitions, including supercooled liquids [42] and atmospheric aerosol particles [43]. For disordered Ising models they have been realized experimentally in, for example, doped manganites [44] and colossal magnetoresistive manganites [45]. Despite their importance, metastable states are not completely understood theoretically [41], with analytical results largely restricted to 1D [46] and many intricate issues remaining in 2D [47].

The key factor controlling melt pond configurations is the pre-melt ice topography, represented by random variables h_i . In the spirit of creating order from disorder, these variables are assumed to be independent Gaussian with zero mean and unit variance. The lattice constant $a = 0.85m$ is specified as the length scale above which important spatially correlated fluctuations occur in the power spectrum of sea ice topography. The model uses the following update rule for Glauber dynamics, depending on whether there is a majority among the four neighbors of a chosen site. If a majority exists, the site is updated to align with the majority because of heat diffusion between neighboring sites. Otherwise, a *tiebreaker* rule is introduced that describes the tendency for water to fill troughs: the chosen site is updated to ice if its pre-melt ice height is positive, and water otherwise; see Fig. 2.7. Note that this update rule does not depend on any parameters other than h_i .

Minimal models such as the RFIM necessarily have limitations. In particular, the RFIM has a percolation threshold very close to 0.5 at $H = 0$. This threshold decreases

transition.

as H decreases, but likely always exceeds the value for real melt ponds. This discrepancy may be attributed to unresolved processes at smaller scales, and/or the observed pre-melt ice topography being spatially correlated rather than completely random. This can be anticipated that, based on a significant amount of observational data, a detailed scheme for choosing the initial spin configuration and update sequence may be formulated.

The interpretation of complex Arctic melt ponds in terms of a simple disordered system may well advance the ability to model the future trajectory of the Arctic sea ice pack, *e.g.*, through parameterizations in global climate models [28].

2.2.2. Small scale models

Single melt pond model

Skyllingstad *et al.* [48] investigate the thermodynamic behaviour of melt ponds using two modeling approaches. First approach addresses the heat budget of a melt pond using a large-eddy simulation (LES) model that can directly simulate the motion of water within a melt pond. Use of the LES model allows to estimate the importance of wind-forcing and heat transport within the pond. However, because of the high computational cost of LES, they could only examine the heat transport processes over periods of a few hours. In addition, three basic pond configurations were considered in the LES experiments, each designed to test the importance of the pond horizontal area versus perimeter. (Fig. 2.8)

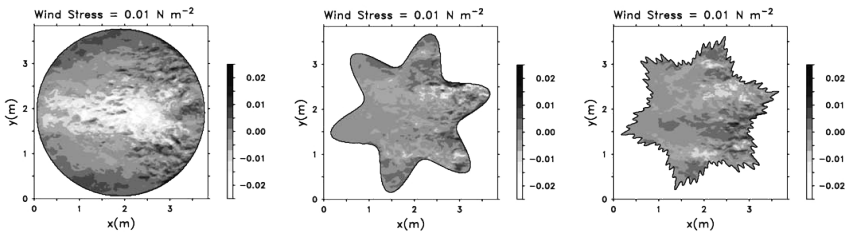


Figure 2.8 – Horizontal velocity for 4 – m pond with different configurations. Courtesy of Skyllingstad *et al.* [48]

To examine longer-term pond behaviour, a less complicated bulk model is developed, which concentrates on the radiative heating within the pond. The bulk model simulates pond growth by treating the pond as well mixed and tracks the width, length, and depth of the pond as a function of time. This method differs from previous bulk models by considering the pond size and applying the pond budget equation with a depth-dependent solar flux. The model provides a useful tool that can bridge the gap between expensive, high-resolution LES and single layer ice models as described by Taylor and Feltham [20]. In both the LES and bulk models, they do not account for fluxes of heat and water from lateral transport through porous ice. These factors require a more complete ice model and surface process model.

In their model, they address the uncertainties in modeling melt ponds in quantify-

ing how solar heat is transferred. To estimate the relative importance of side versus edge melting, they apply an LES model that directly simulates the motion of water throughout the pond and the transport of heat from the pond interior to the bottom and sides. The LES model is based on the filtered nonhydrostatic, Navier-Stokes equations with a subgrid-scale closure provided by Ducros *et al.* [49]. Pond boundaries are simulated using a volume of fluid approach following Steppeler *et al.* [50] and Adcroft *et al.* [51]. The equations of motion are defined using an enstrophy conserving scheme following Tripoli [52].

Results from the LES pond model indicate that ponds are very likely to develop well-mixed conditions even when ponds begin with significant stratification. Simulations show that very light winds ($2 \sim 3 \text{ m/s}$) are able to move pond water vertically, causing transport of heat throughout the pond system. When stratified with a 4 psu salinity gradient, the model predicts a delay in pond mixing of several hours, but still develops a well-mixed equilibrium state.

Well-mixed conditions in ponds suggest that heat will transfer equally to the side and bottom of the pond. For the most part, their experiments support this hypothesis; however, pond shape does limit the movement of water even when well mixed. Simulations with a variety of pond shapes and sizes show that the basic ratio of sidewall area to bottom area, can be used to characterize most ponds. For example, as pond size increases, the bottom area increases in relation to the side area. Consequently, relatively small ponds have a larger lateral growth rate from melting in comparison with large ponds.

The drawback of this model is that the experiments performed by the model are only able to give estimates of the pond melting rates and do not address pond evolution forced by water inflow and outflow from the surrounding ice. Clearly, these aspects of pond behaviour are also a key element in controlling the ice-albedo feedback. Moreover, the sizes of experiments are independent of internal dynamics of the simulation, *i.e.* time independent. In addition, the rate of melting is considered constant and set to that suggested by McPhee *et al.* [53].

Considering the present model, the necessity of investigating the internal dynamics of melt-pond is undeniable. Therefore, in our model we consider the problem of melting through simulation of complete melting process. Similarly, we consider different aspects, *e.g.* moving boundary and volumetric bulk heating.

2.3. Summary and open issues

Melt ponds are pools of open water that form on sea ice in the warmer months of spring and summer. The ponds are also found on glacial ice and ice shelves. Ponds of melted water can also develop under the ice.

Melt ponds are usually darker than the surrounding ice, and their distribution and size is highly variable. They absorb solar radiation rather than reflecting it as ice does and, thereby, have a significant influence on Earth's radiation balance. This differential, which had not been scientifically investigated until recently, has a large effect on the rate of ice melting and the extent of ice cover.

Through this chapter, we described the mechanism that involves formation of melt ponds. Furthermore, we talked about albedo (a measure for reflectance or optical brightness), and effect of melt ponds in reduction of surface albedo of sea ice, which in advance

results in absorption of more solar radiation and consequently warmer environment.

Several models have been developed over last two decades to simulate the distribution of melt ponds in sea ice, and investigate the mechanism of growth of melt pond at large scale, that we briefly mentioned in this chapter. However, there are several questions that still needed to be answered:

- i) What are the processes involved in the dynamics of a melt pond, and how do melt ponds evolve?
- ii) What is heat flux intensity behaviour with respect to the geometry of melt pond, and how it is linked with the melt rate?
- iii) How can one characterize the corrugation and morphology of bottom melt pond (ice-water) interface ?
- iv) How solid liquid interface does interact with internal dynamics of melt pond?
- v) What effects do other constrains, such as internal heating and moving boundary, have on the rate of melting and total heat budget?

In the next part, we try to answer these questions and understand the internal dynamics of melt ponds through the numerical simulation of the melting system. Furthermore, the micro-scale study performed here can be used to parametrize the influence of melt pond in large scale.

References

- [1] O. I. Mamayev, *Temperature-salinity analysis of world ocean waters*, Vol. 11 (Elsevier, 2010).
- [2] T. C. Grenfell and G. A. Maykut, *The optical properties of ice and snow in the arctic basin*, *Journal of Glaciology* **18**, 445 (1977).
- [3] D. K. Perovich, *The optical properties of sea ice.*, Tech. Rep. (COLD REGIONS RESEARCH AND ENGINEERING LAB HANOVER NH, 1996).
- [4] D. Perovich, T. Grenfell, B. Light, and P. Hobbs, *Seasonal evolution of the albedo of multiyear arctic sea ice*, *Journal of Geophysical Research: Oceans* **107** (2002).
- [5] R. E. Brandt, S. G. Warren, A. P. Worby, and T. C. Grenfell, *Surface albedo of the antarctic sea ice zone*, *Journal of Climate* **18**, 3606 (2005).
- [6] T. C. Grenfell and D. K. Perovich, *Spectral albedos of sea ice and incident solar irradiance in the southern beaufort sea*, *Journal of Geophysical Research: Oceans* **89**, 3573 (1984).
- [7] S. G. Warren, *Optical properties of snow*, *Reviews of Geophysics* **20**, 67 (1982).
- [8] D. Perovich, W. Tucker, and K. Ligett, *Aerial observations of the evolution of ice surface conditions during summer*, *Journal of Geophysical Research: Oceans* **107** (2002).
- [9] D. K. Perovich, B. Light, H. Eicken, K. F. Jones, K. Runciman, and S. V. Nghiem, *Increasing solar heating of the arctic ocean and adjacent seas, 1979–2005: Attribution and role in the ice-albedo feedback*, *Geophysical Research Letters* **34** (2007).

- [10] T. Markus, J. C. Stroeve, and J. Miller, *Recent changes in arctic sea ice melt onset, freezeup, and melt season length*, *Journal of Geophysical Research: Oceans* **114** (2009).
- [11] T. C. Grenfell and D. K. Perovich, *Seasonal and spatial evolution of albedo in a snow-ice-land-ocean environment*, *Journal of Geophysical Research: Oceans* **109** (2004).
- [12] F. Fetterer and N. Untersteiner, *Observations of melt ponds on arctic sea ice*, *Journal of Geophysical Research: Oceans* **103**, 24821 (1998).
- [13] H. Eicken, T. Grenfell, D. Perovich, J. Richter-Menge, and K. Frey, *Hydraulic controls of summer arctic pack ice albedo*, *Journal of Geophysical Research: Oceans* **109** (2004).
- [14] D. Perovich, K. Jones, B. Light, H. Eicken, T. Markus, J. Stroeve, and R. Lindsay, *Solar partitioning in a changing arctic sea-ice cover*, *Annals of Glaciology* **52**, 192 (2011).
- [15] H. Eicken, H. Krouse, D. Kadko, and D. Perovich, *Tracer studies of pathways and rates of meltwater transport through arctic summer sea ice*, *Journal of Geophysical Research: Oceans* **107** (2002).
- [16] J. J. Yackel and D. G. Barber, *Melt ponds on sea ice in the canadian archipelago: 2. on the use of radarsat-1 synthetic aperture radar for geophysical inversion*, *Journal of Geophysical Research: Oceans* **105**, 22061 (2000).
- [17] M. G. Serreze, J. A. Maslanik, G. R. Scharfen, R. G. Barry, and D. A. Robinson, *Inter-annual variations in snow melt over arctic sea ice and relationships to atmospheric forcings*, *Annals of Glaciology* **17**, 327 (1993).
- [18] G. A. Maykut and N. Untersteiner, *Some results from a time-dependent thermodynamic model of sea ice*, *Journal of Geophysical Research* **76**, 1550 (1971).
- [19] A. J. Semtner Jr, *A model for the thermodynamic growth of sea ice in numerical investigations of climate*, *Journal of Physical Oceanography* **6**, 379 (1976).
- [20] P. D. Taylor and D. L. Feltham, *A model of melt pond evolution on sea ice*, *Journal of Geophysical Research: Oceans* **109**, (2004), c12007.
- [21] D. K. Perovich, *Theoretical estimates of light reflection and transmission by spatially complex and temporally varying sea ice covers*, *Journal of Geophysical Research: Oceans* **95**, 9557 (1990).
- [22] A. P. Makshtas, E. L. Andreas, P. N. Svyashchennikov, and V. F. Timachev, *Accounting for clouds in sea ice models*, *Atmospheric research* **52**, 77 (1999).
- [23] P. D. Taylor, *Mathematical modelling the formation and evolution of melt ponds on sea ice* (University of London, University College London, 2003).
- [24] D. Flocco, D. Schroeder, D. L. Feltham, and E. C. Hunke, *Impact of melt ponds on arctic sea ice simulations from 1990 to 2007*, *Journal of Geophysical Research: Oceans* **117** (2012).
- [25] M. Lüthje, D. Feltham, P. Taylor, and M. Worster, *Modeling the summertime evolution of sea-ice melt ponds*, *Journal of Geophysical Research: Oceans* **111** (2006).
- [26] F. Scott and D. Feltham, *A model of the three-dimensional evolution of arctic melt ponds on first-year and multiyear sea ice*, *Journal of Geophysical Research: Oceans* **115** (2010).
- [27] A. Thorndike, D. Rothrock, G. Maykut, and R. Colony, *The thickness distribution of sea ice*, *Journal of Geophysical Research* **80**, 4501 (1975).

- [28] D. Flocco, D. L. Feltham, and A. K. Turner, *Incorporation of a physically based melt pond scheme into the sea ice component of a climate model*, Journal of Geophysical Research: Oceans **115** (2010).
- [29] W. D. Collins, C. M. Bitz, M. L. Blackmon, G. B. Bonan, C. S. Bretherton, J. A. Carton, P. Chang, S. C. Doney, J. J. Hack, T. B. Henderson, *et al.*, *The community climate system model version 3 (ccsm3)*, Journal of Climate **19**, 2122 (2006).
- [30] B. Briegleb and B. Light, *A delta-eddington multiple scattering parameterization for solar radiation in the sea ice component of the community climate system model*, NCAR Tech. Note NCAR/TN-472+ STR , 1 (2007).
- [31] J. Curry, J. Schramm, D. Perovich, and J. Pinto, *Applications of sheba/fire data to evaluation of snow/ice albedo parameterizations*, Journal of Geophysical Research: Atmospheres **106**, 15345 (2001).
- [32] M. M. Holland, D. A. Bailey, B. P. Briegleb, B. Light, and E. Hunke, *Improved sea ice shortwave radiation physics in ccsm4: The impact of melt ponds and aerosols on arctic sea ice*, Journal of Climate **25**, 1413 (2012).
- [33] D. Flocco and D. L. Feltham, *A continuum model of melt pond evolution on Arctic sea ice*, Journal of Geophysical Research: Oceans **112**, (2007), c08016.
- [34] W. H. Lipscomb, *Remapping the thickness distribution in sea ice models*, Journal of Geophysical Research: Oceans **106**, 13989 (2001).
- [35] Y.-P. Ma, I. Sudakov, and K. M. Golden, *Ising model for melt ponds on arctic sea ice*, arXiv preprint arXiv:1408.2487 (2014).
- [36] D. Andelman and J.-F. Joanny, *Metastability in the random-field ising model*, Physical Review B **32**, 4818 (1985).
- [37] J. Ehrig, E. P. Petrov, and P. Schwille, *Near-critical fluctuations and cytoskeleton-assisted phase separation lead to subdiffusion in cell membranes*, Biophysical journal **100**, 80 (2011).
- [38] F. J. Perez-Reche, M. L. Rosinberg, and G. Tarjus, *Numerical approach to metastable states in the zero-temperature random-field ising model*, Physical Review B **77**, 064422 (2008).
- [39] C. Hohenegger, B. Alali, K. Steffen, D. Perovich, and K. Golden, *Transition in the fractal geometry of arctic melt ponds*, The Cryosphere **6**, 1157 (2012).
- [40] A. P. Young, *Spin glasses and random fields*, Vol. 12 (World Scientific, 1998).
- [41] P. L. Krapivsky, S. Redner, and E. Ben-Naim, *A kinetic view of statistical physics* (Cambridge University Press, 2010).
- [42] S. Büchner and A. Heuer, *Metastable states as a key to the dynamics of supercooled liquids*, Physical review letters **84**, 2168 (2000).
- [43] M. Rood, M. Shaw, T. Larson, and D. Covert, *Ubiquitous nature of ambient metastable aerosol*, Nature **337**, 537 (1989).
- [44] A. Moreo, M. Mayr, A. Feiguin, S. Yunoki, and E. Dagotto, *Giant cluster coexistence in doped manganites and other compounds*, Physical Review Letters **84**, 5568 (2000).
- [45] W. Wu, C. Israel, N. Hur, S. Park, S.-W. Cheong, and A. De Lozanne, *Magnetic imaging of a supercooling glass transition in a weakly disordered ferromagnet*, Nature materials **5**, 881 (2006).
- [46] B. Derrida and E. Gardner, *Metastable states of a spin glass chain at 0 temperature*, Journal de physique **47**, 959 (1986).

- [47] C. Newman and D. Stein, *Metastable states in spin glasses and disordered ferromagnets*, *Physical Review E* **60**, 5244 (1999).
- [48] E. D. Skillingstad and C. A. Paulson, *A numerical study of melt ponds*, *Journal of Geophysical Research: Oceans* **112** (2007).
- [49] F. Ducros, P. Comte, and M. Lesieur, *Large-eddy simulation of transition to turbulence in a boundary layer developing spatially over a flat plate*, *Journal of Fluid Mechanics* **326**, 1 (1996).
- [50] J. Steppeler, H.-W. Bitzer, M. Minotte, and L. Bonaventura, *Nonhydrostatic atmospheric modeling using az-coordinate representation*, *Monthly weather review* **130**, 2143 (2002).
- [51] A. Adcroft, C. Hill, and J. Marshall, *Representation of topography by shaved cells in a height coordinate ocean model*, *Monthly Weather Review* **125**, 2293 (1997).
- [52] G. J. Tripoli, *A nonhydrostatic mesoscale model designed to simulate scale interaction*, *Monthly Weather Review* **120**, 1342 (1992).
- [53] M. G. McPhee, G. A. Maykut, and J. H. Morison, *Dynamics and thermodynamics of the ice/upper ocean system in the marginal ice zone of the greenland sea*, *Journal of Geophysical Research: Oceans* **92**, 7017 (1987).



3

Evolution equations for conduction, convection and phase-change

This chapter is dedicated to the mathematical modeling of conductive and convective melting. The problem of conductive melting of a pure substance, known as Stefan Problem, is introduced first. Then, the same problem coupled with moving boundary is considered, which will account for wind effects in the melt-pond. The numerical results of melting system coupled with moving boundary is presented in chapter 6.

Following the solution of the Stefan problem, we continue with describing system of natural thermal convection between two horizontal plates with temperature gradient, which is known as Rayleigh-Bénard system. Finally, bulk-heating is considered in order to account for solar radiation effects in melt pond simulation presented in chapter 7.

3.1. The mathematical model system

The model system considered in this study consists of a solid layer of a pure substance of thickness H_{max} initially at a constant uniform temperature, T_m , equal to the phase-change (melting) temperature. At time $t \geq 0$ the bottom boundary of the solid is heated at a constant temperature $T_0 > T_m$ and a melted fluid layer begins to grow from below. The solid starts to melt and during the process of melting the system goes through stages of conductive and convective melting, based on the height of liquid fraction.

We shall note that our model system is dynamically equivalent to the setting mentioned earlier of an Arctic melt pond, although it is an upside-down representation. In order to better explain this equivalency one has to consider the special behaviour of the density profile of water and its anomaly at 4°C as shown in Fig.3.1a. Such an anomaly is absent in most of materials (such as wax, glycerol, *etc.* used in solidification experiments), where increasing the temperature of a substance decreases its density by increasing its volume. This tendency of matter to change in shape, area, and volume in response to a change in temperature is known as thermal expansion.

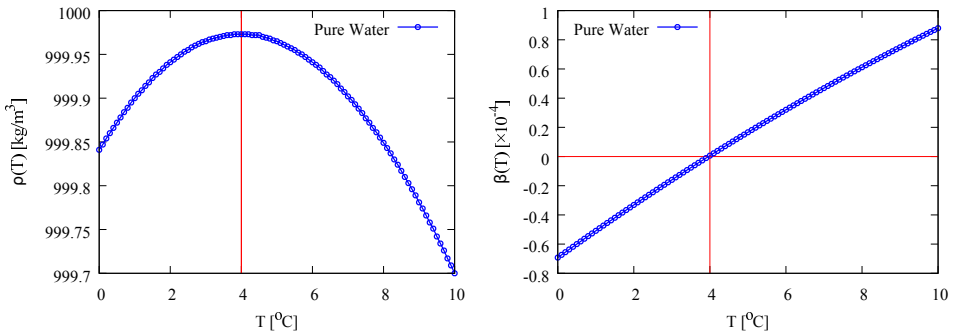
A number of materials contract on heating within certain temperature ranges; this is usually called negative thermal expansion, rather than "thermal contraction" ($\beta < 0$).



For example, the coefficient of thermal expansion of water drops to zero as it is cooled to 3.983°C and then becomes negative below this temperature; this means that water has a maximum density at this temperature (see Fig. 3.1a and 3.1b).

In most materials, heating the bottom of a fluid results in convection of the heat from the bottom to the top, due to the decrease in the density of the heated fluid. This causes it to rise relative to more dense unheated material. However, due to the thermal contraction property (negative thermal expansion) of water below 4 degrees, lighter water at the bottom of melt pond and at the temperature of melting (0°C), rises to the warmer surface of melt-pond.

3



(a) Density profile of water from $0 \sim 10^\circ\text{C}$ and its anomaly at $T < 4^\circ\text{C}$.

(b) Coefficient of thermal expansion of water from 0°C to 10°C . Water below 4°C shows thermal contraction ($\beta < 0$), whereas above 4°C it shows expansion ($\beta > 0$)

Figure 3.1 – Plots of density profile and thermal expansion coefficient of pure water from $0 \sim 10^\circ\text{C}$.

The temperature difference that we are interested in and has been addressed in this work is also $\Delta T = 1^\circ\text{C}$. Therefore, as we can see in Fig. 3.1a, in the range between 0°C and 1°C , density-temperature relation of water is reversal to most material where the density decreases with the increase of the temperature. Moreover, as one can see in Fig. 3.1a, in the range 0°C to 1°C , the density profile of water can be considered linear.

The reason for choosing such a configuration for our model is its universality, and the fact that the comparison between this model and its corresponding Rayleigh-Bénard is easier.

To summarize, in ice-ponds, as we already mentioned, the heating occurs at the top rather than the bottom but buoyancy force is pointing downward for warmer parcels of water, the two effects compensate leading to the same driving convective forcing of the above described model system. The visualization of equivalency of dynamics of melt-pond heated from above and simulations heated from bottom is shown in Fig. 3.2. Panel 3.2a shows thermal contraction of water below 4 degrees, whereas panel 3.2b shows thermal expanding material (water above 4, and majority of other materials).

In the following sections, we introduce governing equations for system of conduc-

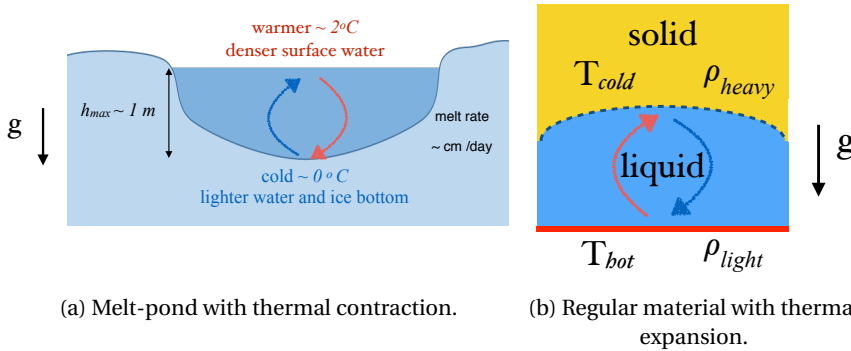


Figure 3.2 – Visualization of equivalency of dynamics of melt-pond heated from above and simulations heated from bottom.

tive melting and convective one. Moreover, two constraints of moving boundary and bulk heating will be introduced. In each case, if the analytical solution exists, we will introduce it completely. The analytical solutions will be used later to validate the numerical code we developed to investigate system of melting.

3.2. Conductive melting

The melting of ice and solidification of water are two examples of a phenomenon called a phase transformation, which is a discontinuous change of the properties in the substance. The different states of aggregation are called phases and they share the same physical properties (for instance density and chemical composition), therefore a phase is more specific than a state of matter. As a phase transition occurs, there will appear a latent heat which either is absorbed or released by the body/thermodynamic system without changing the temperature.

The model system is a solid layer at the temperature of melting T_m heated from the bottom with temperature T_0 . The heat starts to melt the solid layer and form a liquid layer. The heat continues to transfer through the liquid layer by the mean of conduction and melts the solid layer. A schematic of the model system is shown in Fig. 3.3, the coordinate frame is fixed at the bottom boundary, and the position of the solid/liquid interface is moving in the z -direction.

The first known paper about diffusion of heat in a medium with a change of phase state was published by the French mathematicians Gabriel Lamé and Benoît Paul Émile Clapeyron in 1831 [1]. The stated problem was to cool a liquid filling the half-space $x > 0$ and determine the thickness of the generated solid crust, with an imposed temperature at $x = 0$. They discovered that the thickness of the crust is proportional to the square root of time, but no determination of the coefficient of proportionality was attached.

Almost 60 years later in 1889 was this question picked up and stated in a more general form by the physicist and mathematician Joseph Stefan [2]. Joseph Stefan described a mathematical model for real physical problems with a phase-change [3]. This was the first general study of this type of problem, and since then free boundary problems are

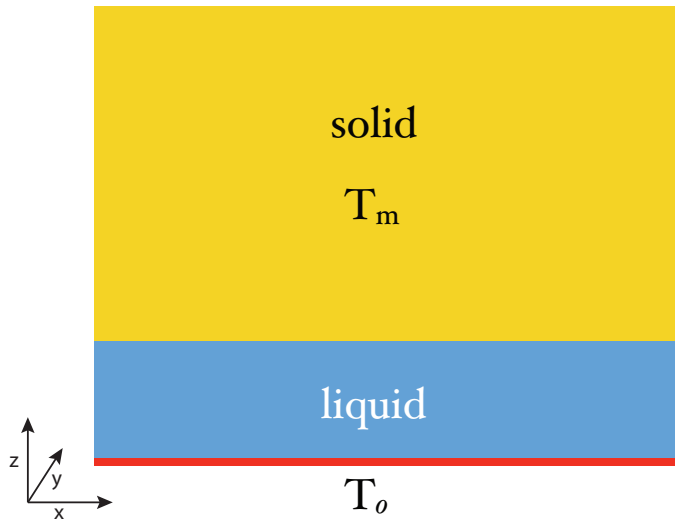


Figure 3.3 – Schematic diagram of the melting system. The system is filled with a pure solid at the temperature of melting (T_m). The temperature at the bottom (T_0) is higher than the melting temperature, consequently the solid turns into liquid for $t > 0$. Due to the thermal conduction through the liquid layer, the solid continues to melt over time. The local height of interface is denoted with z_m , in general it is a function of spatial coordinates x, y and of time t .

called Stefan problems. The given mathematical solution was actually found earlier by the German physicist and mathematician Franz Ernst Neumann in 1860. It is called the Neumann solution [4].

3.2.1. One dimensional Stefan problem

The Stefan problem is a specific type of boundary value problem for a partial differential equation concerning heat distribution in a phase changing medium. Since the evolution of the interface is a priori unknown, a part of the solution will be to determine the boundary. An example is the diffusion of heat in the melting of ice, and as the melting occurs the boundary of the ice will be changing position. The problem is by some authors denoted as a "free boundary value problem" due to the fact that the boundary of the domain is a priori unknown [5–7]. To distinguish the case of a moving boundary (associated with a time-dependent problem) from the problem with fixed boundaries, a few authors denote the former as a "moving boundary problem" [8]. To stick with the common notation, the term "free boundary problem" will be used in this thesis and denote both the time-dependent and the stationary boundary.

To achieve a unique solution for the Stefan problem, two boundary conditions are needed; one to determine the moving boundary itself and one is as usual a suitable condition on the fixed boundary. The natural occurrence of the Stefan problem is mostly associated with the melting and solidification problems, however there also exist some Stefan-like problems, for instance the fluid flow in porous media or even shock waves in

gas dynamics [2].

In this section, we formulate the most simple form of a mathematical model describing phase transitions. The classical Stefan problem is a solidification and a melting problem, for example the transition between ice and water. To acquire a solution for the classical Stefan problem, the heat equation needs to be solved. As mentioned before, a boundary condition on the evolving boundary is needed to get a unique solution. It is called "the Stefan condition" and will be derived below. The result of analytical solutions of this section will later be used in order to validate our DNS results.

3.2.2. The Stefan condition

The evolving unknown interface is denoted as $H(t)$, where z is the position in space and t is the time. To derive the Stefan condition we need to make some assumptions. As the transitions occur there will be a small volume change due to different density of solid and liquid; although here, we will ignore this property for simplicity. By physical reason the temperature should be continuous at the interface $H(t)$ between the phases:

$$\lim_{z \rightarrow H(t)^+} T_s(z, t) = \lim_{z \rightarrow H(t)^-} T_l(z, t) = T_m \quad \text{for all } t. \quad (3.1)$$

The phase-change temperature between the two phases is assumed to be of constant value, T_m . At a fixed time $t = t_0$ consider a domain Ω with two different phases separated at $z = H(t_0)$ (Fig. 3.4). We assume plane symmetry (in other direction except z) to have the temperature T depending only on t and z .

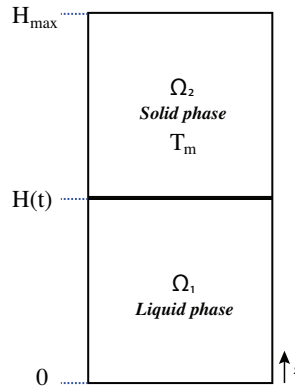


Figure 3.4 – Domain Ω separated into two phases at $H(t)$ which are $\Omega_1 = \Omega \cap \{z < H(t)\}$ and $\Omega_2 = \Omega \cap \{z > H(t)\}$.

Assume the case of the interface evolving to the top, *i.e.*, when the solid is melting. Thus we should expect that $T \geq T_m$ in the liquid phase and $T \leq T_m$ in the solid phase. At time $t = t_0$ consider a portion of the interface, for simplicity in the shape of a disk with area A . Later at time $t_1 > t_0$ the position of the interface has changed to $H(t_1) > H(t_0)$. Meanwhile a cylinder of volume $A \times (H(t_1) - H(t_0))$ has melted and therefore released a quantity of heat Q :

$$Q = A \times (H(t_1) - H(t_0)) \times \rho \mathcal{L}, \quad (3.2)$$

where \mathcal{L} and ρ are the specific latent heat and the density, respectively. We can define the heat flux in liquid and solid as

$$\Phi_l = -\Lambda_l \nabla T_l, \quad (3.3)$$

$$\Phi_s = -\Lambda_s \nabla T_s, \quad (3.4)$$

where K_i is the material's conductivity. By the mean conservation of energy, equation (3.2) reads:

$$\begin{aligned} Q &= \int_{t_0}^{t_1} \int_A [\Phi_l \cdot \hat{\mathbf{z}} - \Phi_s \cdot \hat{\mathbf{z}}] dA d\tau \\ &= \int_{t_0}^{t_1} \int_A [-\Lambda_l \nabla T_l \cdot \hat{\mathbf{z}} + \Lambda_s \nabla T_s \cdot \hat{\mathbf{z}}] dA d\tau, \\ &= A \int_{t_0}^{t_1} [-\Lambda_l \frac{\partial T_l}{\partial z}(H(\tau), \tau) + \Lambda_s \frac{\partial T_s}{\partial z}(H(\tau), \tau)] d\tau, \end{aligned} \quad (3.5)$$

where $\hat{\mathbf{z}}$ is unit vector in z -direction. By using equation (3.2) we have

$$\rho \mathcal{L} (H(t_1) - H(t_0)) = \int_{t_0}^{t_1} [-\Lambda_l \frac{\partial T_l}{\partial z}(H(\tau), \tau) + \Lambda_s \frac{dT_s}{dz}(H(\tau), \tau)] d\tau, \quad (3.6)$$

which by dividing by $(t_1 - t_0)$ and take the limit as $t_1 \rightarrow t_0$ we get

$$\rho \mathcal{L} \lim_{t_1 \rightarrow t_0} \frac{H(t_1) - H(t_0)}{t_1 - t_0} = \lim_{t_1 \rightarrow t_0} \frac{1}{t_1 - t_0} \int_{t_0}^{t_1} [-\Lambda_l \frac{dT_l}{dz}(H(\tau), \tau) + \Lambda_s \frac{dT_s}{dz}(H(\tau), \tau)] d\tau. \quad (3.7)$$

The Mean-Value theory for integral states that there exists a value $c \in [t_0, t_1]$ where

$$\rho \mathcal{L} \frac{dH(t_0)}{dt} = \lim_{t_1 \rightarrow t_0} \frac{1}{t_1 - t_0} \times (t_1 - t_0) f(c), \quad (3.8)$$

where for simplicity we introduced a new function

$$f(c) \equiv -\Lambda_l \frac{dT}{dz}(H(c), c) + \Lambda_s \frac{dT}{dz}(H(c), c). \quad (3.9)$$

However, as $t_1 \rightarrow t_0$ and $f(c)$ is continuous, we can conclude that

$$\rho \mathcal{L} \frac{dH(t_0)}{dt} = f(t_0), \quad (3.10)$$

which is valid for any arbitrary time t_0 and consequently for any t . Expanding the equation and substituting $f(t)$ we have

$$\rho \mathcal{L} \frac{dH(t)}{dt} = -\Lambda_l T(H(t); t) + \Lambda_s T(H(t); t), \quad (3.11)$$

which is known as the *Stefan condition* and is a boundary condition for liquid-solid interface [7].

3.2.3. One dimensional melting problem

The one-dimensional phase problem could be represented as a semi-infinite solid, for instance a thick block of ice occupying $0 \leq z < \infty$ at the solidification temperature $T = T_m$. One assumption is needed which states that we ignore any volume change in the solidification. At the fixed boundary of the thick block of ice $z = 0$ there could be many different type of boundary conditions. For instance, we could have a constant temperature which is above the solidification temperature *i.e.* $T_0 > T_m$, or a function depending on time ($f(t)$). We assume that the temperature in the solid phase is constant. Thus the problem is to find the temperature distribution in the liquid phase and the location of the free boundary $H(t)$ (which here is the melting front position and later in convective regime is the average of the interface). Even if there will be two phases present, the problem is called a one-phase problem since it is only the liquid phase which is unknown. The governing equations and boundary condition for the one dimensional melting problem can be summarized as following:

Liquid region,	$0 \leq z < H(t),$
$\frac{\partial T}{\partial t} = \frac{\Lambda_l}{c_p \rho} \frac{\partial^2 T}{\partial z^2} = \kappa \frac{\partial^2 T}{\partial z^2},$	The heat equation $0 < z < H(t), t > 0,$
$T(0, t) = f(t),$	Bottom boundary condition $t > 0,$
$T(z, 0) = T_m,$	Initial condition,
Free boundary condition,	$z = H(t),$
$\frac{dH(t)}{dt} = -\kappa \frac{c_p}{\mathcal{L}} \left. \frac{dT}{dz} \right _{z=H(t)},$	Stefan condition,
$H(0) = 0,$	Initial position of melting interface,
$T(H(t), t) = T_m,$	Dirichlet condition at the interface,
Solid region,	$H(t) < z < \infty,$
$T(z, t) = T_m,$	Solid at the uniform temperature of melting, $z \geq H(t).$

The boundary condition for temperature at $z = 0$ is considered here as a constant temperature ($f(t) = T_0$). Furthermore, without loosing the generality one can subtract T_m from the whole system and have $T_0 = \Delta T$ and $T_m = 0$.

3.2.4. Similarity Solution

In this part, we consider the Stefan problem with initial and boundary conditions we stated before and try to derive an explicit expression for the solution. By considering the ordinary rescaled heat equation $T_t - T_{zz} = 0$, one can find the solution by change of variable and introducing the similarity variable

$$\zeta = \frac{z}{\sqrt{t}}, \quad (3.12)$$

and thus seeks a solution of the form

$$T(z, t) = F(\zeta(z, t)), \quad (3.13)$$

where $F(\zeta)$ is an unknown function yet to be found. Substituting (3.13) into the heat equation gives

$$\frac{\partial T}{\partial t}(z, t) = \frac{dF}{d\zeta} \frac{\partial \zeta}{\partial t} = \frac{-z}{2t\sqrt{t}} \frac{dF}{d\zeta}, \quad (3.14)$$

$$\frac{\partial T}{\partial z}(z, t) = \frac{dF}{d\zeta} \frac{\partial \zeta}{\partial z} = \frac{1}{\sqrt{t}} \frac{dF}{d\zeta}, \quad (3.15)$$

$$\frac{\partial^2 T}{\partial z^2}(z, t) = \frac{1}{t} \frac{d^2 F}{d\zeta^2}, \quad (3.16)$$

which consequently gives:

$$\frac{d^2 F}{d\zeta^2} + \frac{\zeta}{2\kappa} \frac{dF}{d\zeta} = 0. \quad (3.17)$$

The equation (3.17) is a second order differential equation with solution of the form

$$F(\zeta) = A_1 \operatorname{erf}\left(\frac{\zeta}{2\sqrt{\kappa}}\right) + A_2, \quad (3.18)$$

where A_1 and A_2 are constant and are determined by boundary conditions. Using the definition of similarity variable ζ , we have

$$T(z, t) = A_1 \operatorname{erf}\left(\frac{z}{2\sqrt{\kappa t}}\right) + A_2. \quad (3.19)$$

By using the boundary conditions at $z = 0$ and $z = H(t)$ we have

$$A_1 = \frac{-\Delta T}{\operatorname{erf}(\lambda)}, \quad (3.20)$$

$$A_2 = \Delta T, \quad (3.21)$$

where

$$\lambda \equiv \frac{H(t)}{2\sqrt{\kappa t}}. \quad (3.22)$$

Since A_1 is a constant, it follows that λ must also be constant, thus

$$H(t) = 2\lambda\sqrt{\kappa t}. \quad (3.23)$$

Having the position of solid-liquid interface and temperature profile, one can compute

$$\frac{dH(t)}{dt} = \lambda \frac{\sqrt{\kappa}}{\sqrt{t}} \quad (3.24)$$

$$\frac{dT}{dz}(H(t), t) = -\frac{\Delta T}{\operatorname{erf}(\lambda)} \frac{\exp(-\lambda^2)}{\sqrt{\pi}\sqrt{\kappa t}}, \quad (3.25)$$

which by substituting in the Stefan condition gives

$$\lambda \exp(\lambda^2) \operatorname{erf}(\lambda) = \frac{c_p \Delta T}{\sqrt{\pi} \mathcal{L}} \equiv \frac{St}{\sqrt{\pi}}, \quad (3.26)$$

3.3. Melting with an external moving boundary

where St is the Stefan number [5]. By adding back T_m to the solution of the system and considering $H(t)$ and λ , the solution for Stefan problem can be summarized as

$$T(z, t) = T_0 - \Delta T \frac{\operatorname{erf}\left(\frac{z\lambda}{H(t)}\right)}{\operatorname{erf}(\lambda)}, \quad (3.27)$$

$$H(t) = 2\lambda\sqrt{\kappa t}, \quad (3.28)$$

$$\lambda \exp(\lambda^2) \operatorname{erf}(\lambda) = \frac{St}{\sqrt{\pi}}. \quad (3.29)$$

It should be noted that this is a solution of a one-dimensional problem. In a multidimensional, 2D or 3D systems, the phase-change boundary will stay flat (and horizontal in our setting) at every instant of time along respectively a line or a plane.

Stefan number (St)	Latent Heat (\mathcal{L})	Specific Heat (c_p)	λ
0.01	100.0	1.0	0.070593
0.1	10.0	1.0	0.220016
1.0	1.0	1.0	0.620063
10.0	1.0	10.0	1.256972

Table 3.1 – Table of melting rates (St) used in this research, and corresponding λ for each Stefan number.

The Stefan number (St) is a positive number that requires special attention. It is one of the control parameters of the melting system, and is ratio of the sensible heat to the latent heat. For small St the advancement of solid-liquid is slow, while the rate of melting increases with St . The Stefan number with temperature difference $\Delta T = 1^\circ\text{C}$ of some materials is listed in table 3.2.

3.3. Melting with an external moving boundary

The model system is similar to the Stefan problem, a solid layer at the temperature of melting T_m heated from bottom with temperature T_0 , and with a constant velocity V_x on the warm boundary. Similar to the Stefan problem, heat starts to melt the solid layer and forms a liquid layer. Later, heat continues to transfer through the liquid layer and melt the solid layer. A schematic of the model system is shown in Fig. 3.5, the coordinate frame is fixed at the bottom boundary, and the position of the solid/liquid interface is moving in the vertical direction.

3.3.1. Analytical solution for the velocity field

In this section we derive an analytical solution for the velocity profile for the system of parallel melting coupled with an external moving boundary. As the height of the melting system advances with time, it is logical to consider the effect of viscous dissipation when the height of the liquid layer is very small. However, the effect of viscous dissipation fades away as the height of the melting-front increases. Moreover, at the onset of melting, even the solution of the Stefan problem shows singularity (infinite velocity of the interface).

Substance	Melting ($^{\circ}\text{C}$)	\mathcal{L} (kJ/kg)	c_p (J/kg·K)	St ($\Delta T = 1$)
copper	1083	207	387	0.001869565
silver	962	111	235	0.002117117
aluminum	659	399	900	0.002255639
lead	328	23	128	0.005565217
water	0	335	2060	0.006149254
mercury	-39	11	138	0.012545455
ethyl alcohol	-114	108	2450	0.022685185
oxygen	-219	14	912	0.065142857

Table 3.2 – List of Stefan number for temperature difference $\Delta T = 1^{\circ}\text{C}$ of some materials in the nature. For instance, heating water (ice) at the temperature of melting (0°C) with 1°C results in $St \approx 0.012$.

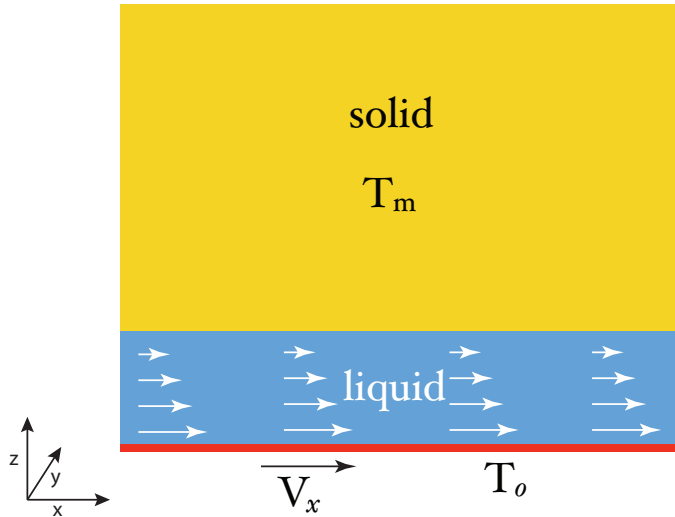


Figure 3.5 – Schematic diagram of the melting system with a moving boundary. The system is filled with a pure solid at the temperature of melting (T_m), heated from the bottom with temperature T_0 higher than the melting temperature. Furthermore, the bottom boundary moves with a constant velocity V_x in the x direction.

Therefore, we neglect the effect of viscous dissipation in our computations. Therefore, the equations describing the system of melting with an external moving boundary are similar to the Stefan problem (temperature field and the height of liquid layer), however with a non-zero velocity field in the liquid layer, which is originated from the applied velocity at the bottom boundary. Therefore, for velocity field we have

$$\frac{\partial u}{\partial t} = v \frac{\partial^2 u}{\partial z^2}, \quad (3.30)$$

3.3. Melting with an external moving boundary

with boundary conditions

$$u(z=0, t) = V_x, \quad (3.31)$$

$$u(z=H(t), t) = 0. \quad (3.32)$$

The equations governing the system of the conductive melting with a moving boundary can be summarized as

Liquid region,	$0 \leq z < H(t),$
$\frac{\partial T}{\partial t} = \kappa \frac{\partial^2 T}{\partial z^2},$	The heat equation $0 < z < H(t), t > 0,$
$\frac{\partial u}{\partial t} = \nu \frac{\partial^2 u}{\partial z^2},$	The equation velocity $0 < z < H(t), t > 0,$
$T(0, t) = f(t),$	Bottom boundary condition for temperature $t > 0,$
$u(0, t) = V_x,$	Bottom boundary condition for velocity $t > 0,$
$T(z, 0) = T_m,$	Initial condition,
Free boundary condition,	$z = H(t),$
$\frac{dH(t)}{dt} = -\kappa \frac{c_p}{\mathcal{L}} \frac{dT}{dz} \Big _{z=H(t)},$	Stefan condition,
$H(0) = 0,$	Initial position of melting interface,
$T(H(t), t) = T_m,$	Dirichlet condition at the interface,
$u(H(t), t) = 0,$	No-slip boundary condition at the interface,
Solid region,	$H(t) < z < \infty,$
$T(z, t) = T_m,$	Solid at the temperature of melting, $z \geq H(t),$
$u(z, t) = 0,$	No displacement in the solid, $z \geq H(t).$

The solution for the temperature field is exactly the same as Stefan Problem (Eqs. 3.27 & 3.28), with the same definition for λ .

However, for velocity field we use similar idea of using similarity variable $\eta = z/H(t)$. Therefore, we have

$$\frac{\partial \eta}{\partial t} = -\frac{z}{H^2(t)} \frac{dH(t)}{dt} = -\frac{2\lambda^2 \kappa}{H^2(t)} \eta, \quad 0 \leq \eta \leq 1. \quad (3.33)$$

Substituting η in Eq. 3.30 results in the ordinary differential equation

$$\frac{d^2 u}{d\eta^2} + \frac{2\lambda^2 \kappa}{\nu} \eta \frac{du}{d\eta} = 0. \quad (3.34)$$

together with boundary conditions

$$u(\eta)|_{\eta=0} = V_x, \quad u(\eta)|_{\eta=1} = 0, \quad (3.35)$$

which can be solved analytically, and the solution is

$$u(z; t) = V_x \left[1 - \frac{\operatorname{erf}\left(\frac{\lambda}{\sqrt{\operatorname{Pr}}} \frac{z}{H(t)}\right)}{\operatorname{erf}\left(\frac{\lambda}{\sqrt{\operatorname{Pr}}}\right)} \right], \quad (3.36)$$

with Pr the Prandtl number.

The profile of velocity is not linear contrary to the case of fully developed Couette flow¹. Instead, velocity profile is in form of error function.

¹In fluid dynamics, Couette flow is the flow of a viscous fluid in the space between two surfaces, one of which is moving tangentially relative to the other.

3.4. Rayleigh-Bénard convection

The problem of convection is quite old (Hadley, Lomonosov, Rumford,...). However, around 1900, Henri Bénard [9] was the first to perform systematic controlled experiments on the convection. He found that the convective motions organized themselves in regular stable cellular patterns, which is now known as Bénard cells, with polygonal shapes, predominantly hexagonal (Fig. 3.6). In his experiment, he used a thin liquid layer with a thickness of the order of a millimeter and with a free upper surface. Observation of depression of the upper free surface of the fluid at each cell center, leads Bénard to speculate about the role of surface tension. Initially it was thought that these instabilities were buoyancy driven.

Rayleigh [10], who was intrigued by the Bénard regular hexagonal cells, studied purely thermally driven flow theoretically to explain Bénard's results. Rayleigh investigated a fluid layer subjected to an unstable vertical temperature gradient, i.e. imposing a bottom temperature superior to the top temperature. He determined a critical temperature difference across the liquid necessary for the convective motion to start, and postulated a dimensionless number associated with buoyancy-driven flow. Using a stability analysis, Rayleigh also obtained a critical wavelength of convective cells. He, however, noticed that his theory did not match quantitatively the results of Bénard.

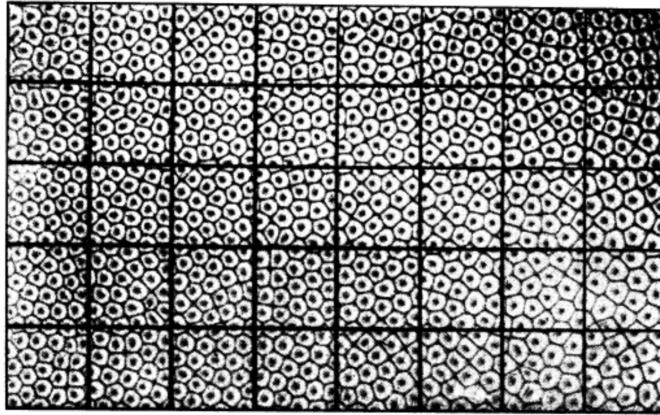


Figure 3.6 – Stabilized regular polygonal convective patterns observed by Bénard [9]. Thin liquid layer (thickness of the order of millimeter) is heated from below with free upper surface. A network of squares with surface 1cm^2 is plotted in the image.

It was not until the second half of the 20th century that Bénard's observations have been explained in the works of Block [11], Pearson [12] and Nield [13]. The convective motion in a layer with free surface was caused by the thermally induced surface tension gradients (the Marangoni effect).

Convection occurring in a horizontal layer heated from below is now called Rayleigh-Bénard convection. In this section, we present its governing equations.

3.4.1. Governing equations

The dynamics of the fluid is described by the basic set of conservation equations (e.g. Landau and Lifshitz [14]); conservation of mass, momentum and energy, which we recall briefly here.

Conservation of mass

The differential form of the continuity equation for mass is

$$\frac{\partial \rho}{\partial t} + \nabla \cdot (\rho \mathbf{u}) = 0, \quad (3.37)$$

where ρ is density and \mathbf{u} is velocity. In case of an incompressible fluid, ρ is constant and mass conservation simplifies to

$$\nabla \cdot \mathbf{u} = 0, \quad (3.38)$$

which is also known as continuity condition.

Conservation of momentum

Momentum conservation equation is given by

$$\rho_0 \left(\frac{\partial \mathbf{u}}{\partial t} + (\mathbf{u} \cdot \nabla) \mathbf{u} \right) = -\nabla P + \mu \nabla^2 \mathbf{u} + \rho \mathbf{g}, \quad (3.39)$$

where \mathbf{g} and P are the gravitational acceleration and the pressure, respectively.

According to the Boussinesq approximation [15], variations in density have no effect on the flow field, except that they give rise to buoyancy forces; and it states that

$$\rho = \rho_0 (1 - \beta(T - T_0)), \quad (3.40)$$

where β is the thermal coefficient of expansion. Therefore, substituting Eq. 3.40 in Eq. 3.39 leads to:

$$\rho_0 \left(\frac{\partial \mathbf{u}}{\partial t} + (\mathbf{u} \cdot \nabla) \mathbf{u} \right) = -\nabla p + \mu \nabla^2 \mathbf{u} + \rho_0 \beta (T - T_0) \mathbf{g} \mathbf{e}_z, \quad (3.41)$$

where \mathbf{e}_z is unit vector in vertical direction, and p is the sum of the dynamic and the hydrostatic pressures $p = P + \rho_0 g z$.

Conservation of energy

By neglecting the viscosity dissipation, conservation of energy equation is given by

$$\rho_0 c_p \left(\frac{\partial T}{\partial t} + (\mathbf{u} \cdot \nabla) T \right) = \nabla \cdot (\Lambda \nabla T), \quad (3.42)$$

where T is the temperature, c_p is the heat capacity at constant pressure, and Λ is the thermal conductivity. By considering constant thermal conductivity, the equation of energy conservation can be simplified to

$$\frac{\partial T}{\partial t} + (\mathbf{u} \cdot \nabla) T = \kappa \nabla^2 T, \quad (3.43)$$

where $\kappa = \frac{\Lambda}{\rho_0 c_p}$ is the thermal diffusivity.

The boundary conditions for the RB system are no-slip velocities and constant temperature at the top and bottom boundaries, and periodic lateral boundary conditions, *i.e.*

$$\mathbf{u}(z=0; t) = \mathbf{u}(z=H; t) = \mathbf{0}, \quad T(z=0; t) = T_0, \quad T(z=H; t) = T_1. \quad (3.44)$$

3.4.2. Non-dimensionalization

Several choices of scaling parameters can be found in the literature and we use the following transformations; for the length $\nabla = \tilde{\nabla}/H$ and $\nabla^2 = \tilde{\nabla}^2/H^2$, the time $t = H^2/\kappa \tilde{t}$, the temperature $T = \Delta T \tilde{T} + T_0$ where $\Delta T = T_1 - T_0$, the velocity $v = \kappa/H \tilde{v}$, and the pressure $p = P_0 \tilde{p} = \kappa^2 \rho/H^2 \tilde{p}$ with P_0 the reference pressure. Dimensionless temperature and length are thus bounded between 0 and 1 in the computational domain. Tilded ($\tilde{}$) variable without physical dimension and we drop it immediately for the sake of simplicity. All scaling parameters are given in Tab. 3.3

Variable	Scaling	
Length	H	Thickness of the system under study (time independent unlike)
Time	$\frac{H^2}{\kappa}$	Conduction time over the thickness H
Velocity	$\frac{\kappa}{H}$	Diffusion velocity
Pressure	$P_0 = \frac{\kappa^2 \rho_0}{H^2}$	Reference pressure
Temperature	ΔT	Temperature difference ($\Delta T = T_1 - T_0$) across H

Table 3.3 – Scaling parameters of different variables.

Substituting dimensionless parameters in Eqs. 3.38, 3.41 and 3.43 gives

$$\begin{cases} \nabla \cdot \mathbf{u} = 0, \\ \left(\frac{\partial \mathbf{u}}{\partial t} + (\mathbf{u} \cdot \nabla) \mathbf{u} \right) = -\nabla p + \text{Pr} \nabla^2 \mathbf{u} + \text{Pr} \text{Ra} T \mathbf{e}_z, \\ \left(\frac{\partial T}{\partial t} + (\mathbf{u} \cdot \nabla) T \right) = \nabla^2 T. \end{cases} \quad (3.45)$$

Two dimensionless numbers appear in Eq. 3.45 which are,

- 1) The Prandtl number Pr which relates the kinematic fluid viscosity ($\nu = \mu/\rho_0$) to the thermal diffusivity (κ):

$$\text{Pr} = \frac{\nu}{\kappa}. \quad (3.46)$$

- 2) The Rayleigh number Ra that compares the driving mechanisms (buoyancy) to dissipative processes (dissipation of heat and momentum):

$$\text{Ra} = \frac{\rho_0 \beta g \Delta T H^3}{\kappa \mu}. \quad (3.47)$$

As it is visible from the definition of the control parameters, the value of the Prandtl number (for a given fluid) is based only on its physical properties, whereas Rayleigh number depends on the parameters of the system as its thickness and ΔT .

3.4. Rayleigh-Bénard convection

Typical values of Rayleigh and Prandtl numbers for water in melt ponds and melted rocks, e.g. lava and magma, are given in Table 3.4. Furthermore, Table 3.5 gives properties of pure water.

Material	Prandtl number	Rayleigh number
For water in melt ponds	7	$O(10^{3-9})$
For melted rocks (lava, magma)	$O(10^{4-8})$	$O(10^{9-17})$

Table 3.4 – Non-dimensional numbers for water in melt ponds and melted rocks, e.g. lava and magma.

Finally, the boundary conditions in non-dimensional form are given by

$$T(\tilde{z} = 0, t) = 1, \quad T(\tilde{z} = 1, t) = 0, \quad (3.48)$$

$$\mathbf{u}(\tilde{z} = 0, t) = \mathbf{u}(\tilde{z} = 1, t) = 0. \quad (3.49)$$

Parameter	Notation	Value	Unit
Boiling temperature (at 101.325 kPa)		99.974	$^{\circ}\text{C}$
Dynamic viscosity	μ	1.787×10^{-3}	$\text{kg s}^{-1} \text{m}^{-1}$
Gravitational acceleration	g	9.8	m s^{-2}
Kinematic viscosity	ν	1.787×10^{-6}	$\text{m}^2 \text{s}^{-1}$
Latent heat of melting	\mathcal{L}	334	kJ/kg
Maximum density (at 4°C)	ρ	999.975	kg m^{-3}
Melting temperature (at 101.325 kPa)		0	$^{\circ}\text{C}$
Specific heat of water (at 0.01°C)	c_p	4.217	kJ/kgK
Specific heat of water (at 5°C)	c_p	4.205	kJ/kgK
Specific heat of water (at 10°C)	c_p	4.194	kJ/kgK
Specific heat of ice		2.108	kJ/kgK
Specific heat of water vapor		1.996	kJ/kgK
Thermal coefficient of expansion	β	2.14×10^{-4}	K^{-1}
Thermal diffusivity	κ	0.143×10^{-6}	m^2/s

Table 3.5 – Parameters and properties of pure water taken from 'www.engineeringtoolbox.com'.

3.4.3. Nusselt number

In the applications, it is of interest to measure the effectiveness of the motion. The most natural and accepted measure that quantifies the enhancement of vertical heat flux due to convection is the Nusselt number, which is the ratio of total heat transfer by conduction and convection (Q_T) over heat transfer by conduction (Q_C). The definition of the Nusselt number is given by

$$Nu = \frac{Q_T}{Q_C} = \frac{Q_T}{-\Lambda \left(\frac{\partial T}{\partial z} \Big|_{z=0} \right)_A}, \quad (3.50)$$

where $\langle \cdot \rangle_A$ denotes the average over horizontal plane and time.

In a convective system bounded by horizontal parallel plates with different temperatures, the Eq. 3.50 takes the following form

$$Nu = \frac{\langle u_z T \rangle_A - \kappa \langle \frac{\partial T}{\partial z} \rangle_A}{\kappa \frac{\Delta T}{H}}, \quad (3.51)$$

where the volumetric heat capacity (ρc_p) has been factorized. Note that, as a consequence of energy conservation, the average ($\langle \cdot \cdot \rangle$) can be taken over any horizontal plane of the system.

3.4.4. Reynolds number

The Reynolds number (Re) is an important dimensionless quantity in fluid mechanics used to predict flow patterns in different fluid flow situations. At low Reynolds numbers flow tends to be dominated by laminar (sheet-like) flow, but at high Reynolds numbers turbulence results from differences in the fluid's speed and direction, which may sometimes intersect or even move counter to the overall direction of the flow (eddy currents).

The Reynolds number is the ratio of inertial forces to viscous forces within a fluid which is subjected to relative internal movement due to different fluid velocities. This relative movement generates fluid friction, which is a factor in developing turbulent flow. Counteracting this effect is the viscosity of the fluid, which as it increases, progressively inhibits turbulence, as more kinetic energy is absorbed by a more viscous fluid. The Reynolds number quantifies the relative importance of these two types of forces for given flow conditions, and is a guide to when turbulent flow will occur in a particular situation.

The Reynolds number is defined as

$$Re = \frac{\rho u H}{\mu} = \frac{u H}{\nu} \quad (3.52)$$

where ρ is the density, u is the velocity of the fluid, H is a characteristic length, μ is the dynamic viscosity, and ν is the kinematic viscosity of the fluid.

In the RB system, as the velocity is not constant, one can use the root mean square of velocity field, which is defined as

$$u_{rms} = \sqrt{\langle u^2 \rangle}. \quad (3.53)$$

In this case, Re is defined as

$$Re = \frac{u_{rms} H}{\nu} \quad (3.54)$$

3.4.5. Scaling theories for global heat flux

For very many years, scientists have studied the motion of enclosed fluids heated from below and cooled from above. At the lowest heating rates, there is no motion. Then, as the heating rate is increased, one sees successively a steady motion, a periodic oscillation, and a chaotic domain. At yet higher heating rates, one finds turbulent motion in which the fluid swirls in highly structured but never-repeating patterns (see figure 3.7).

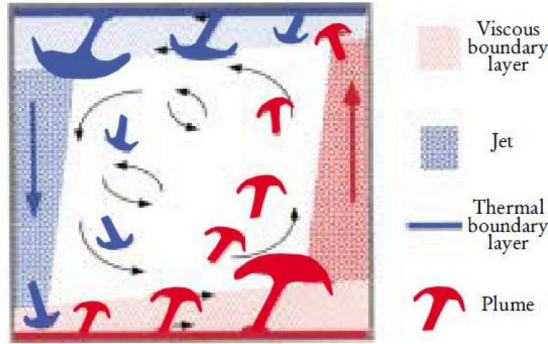


Figure 3.7 – The Rayleigh-Bénard as a machine, schematically drawn. The red-shaded areas of the cell show regions with hot fluid, while the blue areas indicate cold fluid. The arrows give the direction of fluid flow. A major point of this illustration is to list and show the many different structures that work together to make the intricate motion of the convective system. The illustration is from a schematic in [16]

Since the convective fluid flow increases the vertical heat transport beyond the purely conductive flux, our challenge is to determine the relationship

$$Nu = Nu(Ra, Pr), \quad (3.55)$$

from the equations of motion.

In 1954 W.V.R Malkus [17] predicted the scaling law

$$Nu \sim Ra^{\frac{1}{3}}, \quad (3.56)$$

by a marginally stable boundary layer argument, based on the concept that the boundary layer thickness δ adjust itself so as to be, as a convection layer, marginally stable.

The scaling

$$Nu \sim Pr^{\frac{1}{2}} Ra^{\frac{1}{2}}, \quad (3.57)$$

has been postulated (Kraichnan (1962) [18] and Spiegel (1971) [19]) as an asymptotic regime.

Given the increasing richness and precision of experimental and numerical data for $Nu(Ra, Pr)$ and $Re = (Ra, Pr)$, it became clear near the end of the last decade that none of the theories developed up to then could offer a unifying view, accounting for all data. In particular, the predicted Prandtl-number dependencies of Nu [20, 21] are in disagreement with measured and calculated data. Therefore in a series of papers, Grossmann and Lohse [22–26] tried to develop a unifying theory to account for $Nu = (Ra, Pr)$ and $Re = (Ra, Pr)$ over wide parameter ranges.

They postulated that when putting the splitting and modeling assumptions together, one can finally obtain two implicit equations for $Nu = (Ra, Pr)$ and $Re = (Ra, Pr)$ with

six free parameters a , Re_c , and c_i , $i = 1, 2, 3, 4$:

$$\begin{aligned} (Nu-1)RaPr^{-2} &= c_1 \frac{Re^2}{g(\sqrt{Re_c/Re})} + c_2 Re^3, \\ (Nu-1) &= c_3 Re^{1/2} Pr^{1/2} \left\{ f \left[\frac{2aNu}{\sqrt{Re_c}} g \left(\sqrt{\frac{Re_c}{Re}} \right) \right] \right\}^{1/2} \\ &\quad + c_4 Pr Re f \left[\frac{2aNu}{\sqrt{Re_c}} g \left(\sqrt{\frac{Re_c}{Re}} \right) \right], \end{aligned} \quad (3.58)$$

with

$$f(x) = (1+x^4)^{-1/4}, \quad (3.59)$$

$$g(x) = x(1+x^4)^{-1/4}. \quad (3.60)$$

The six parameters in Eq. 3.58 were adjusted so as to provide a fit to 155 data points for $Nu = (Ra, Pr)$ from Ahlers and Xu [27], which results in $a = 0.482$, $c_1 = 8.7$, $c_2 = 1.45$, $c_3 = 0.46$, $c_4 = 0.013$, and $Re_c = 1.0$.

3.4.6. Convection with a uniform volumetric heating

In the process of heating the system in the presence of a uniform volumetric heating, the momentum equation of velocity field is the same as in the RB system. However, the equation of temperature receives an additional term, and is in the form of

$$\partial_t T + (\mathbf{u} \cdot \nabla) T = \kappa \nabla^2 T + \frac{q}{\rho_0 c_p}, \quad (3.61)$$

where q is the power per unit volume.

By non-dimensionalizing the equation (3.61) by using references defined in Table.3.3, we have:

$$\partial_{\tilde{t}} \tilde{T} + (\tilde{\mathbf{u}} \cdot \tilde{\nabla}) \tilde{T} = \tilde{\nabla}^2 \tilde{T} + Q, \quad (3.62)$$

where $Q = qH_{max}^2 / \rho_0 c_p \kappa \Delta T$ is radiative over conductive flux ratio.

In order to validate our numerical system, we focus on a simpler system in conductive regime, where velocity field is zero, and the temperature depends only on the vertical coordinate. Eq. 3.62 can be simplified to

$$\kappa \frac{d^2 T}{dz^2} + \frac{q}{\rho_0 c_p} = 0. \quad (3.63)$$

By using boundary conditions at the bottom ($T = T_0$) and the top ($T = T_1$), the analytical solution for Eq. 3.63 is

$$T(z) = T_0 - \Delta T \frac{z}{H} - \frac{qH^2}{2\rho_0 c_p \kappa} \left(\left(\frac{z}{H} \right)^2 - \frac{z}{H} \right), \quad (3.64)$$

As we can see, the above solution is a sum of two terms. The first one is a result of the external imposed temperature gradient, while the second stems from the contribution of the uniform volumetric heating source.

3.5. Natural convection coupled with phase-change

In this section, we introduce the system of melting coupled with natural convection, due to temperature differences between bottom boundary and the temperature of solid. The model system here is a solid layer at the temperature of melting T_m heated from bottom with temperature T_0 and a melted fluid layer begins to grow from below. The density of the fluid is assumed to be a decreasing function of temperature, therefore the bottom heating produces an unstable stratification of the fluid layer. A schematic of the model system is shown in Fig. 3.8, the coordinate frame is fixed at the bottom boundary, and the position of the solid/liquid interface is moving in the positive vertical z -direction.

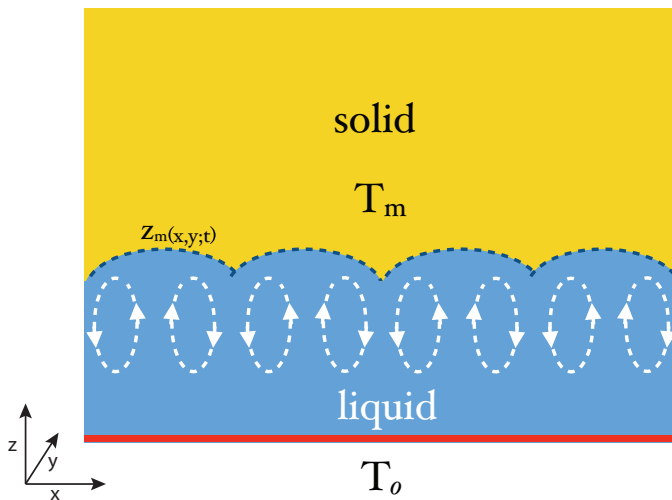


Figure 3.8 – Schematic diagram of the melting system. The system is filled with a pure solid at the temperature of melting (T_m). The temperature at the bottom (T_0) is higher than the melting temperature, consequently the solid turns into liquid for $t > 0$. Due to the thermal expansion coefficient of the liquid, a convection flow may develop in the fluid layer. The local height of interface is denoted with z_m ; in general it is a function of spatial coordinates x, y and of time t .

Due to the strong nonlinearity of solid-liquid phase-change phenomena and the moving boundary, the problems that can be solved via the analytical method are very limited. The limitation of these methods is that they apply to conduction-controlled one-dimensional problems. Although some investigators have attempted to solve two-dimensional phase-change problems by using analytical methods [28–30], the cases investigated represented very simple and special geometries, such as a semi-infinite corner or a semi-infinite wedge.

3.5.1. Enthalpy formulation for phase-change

In this methodology, the governing energy equation is written for the entire region of the phase-change material, including solid and liquid phases and the interface. The enthalpy method is introduced by analyzing a conduction-controlled, two-region melting problem in a finite slab. It is assumed that the densities of the liquid and solid phase are

identical ($\rho_s = \rho_l$). In the enthalpy formulation approach, the energy equation is initially expressed in terms of the total enthalpy. The governing equation for a heat conduction problem can thus be cast in the form

$$\rho \frac{\partial h}{\partial t} = \frac{\partial}{\partial z} \left(k \frac{\partial T}{\partial z} \right). \quad (3.65)$$

The total enthalpy, h , is further split into the sensible enthalpy and the latent heat for the phase-change problem [31]. In this manner, the phase boundary can be solved naturally and determined as part of the solution [32]. h can be written as

$$h = c_p T + \phi_l \mathcal{L}, \quad (3.66)$$

where c_p and L represent the constant-pressure specific heat and the latent heat of phase-change; ϕ_l is the volume-phase fraction of the liquid phase and is zero for the solid region and unity for the liquid region. The phase fraction lies between zero and unity when the region being considered is undergoing phase-change. Substituting Eq. (3.66) into Eq. (3.65) yields

$$\rho \frac{\partial c_p T}{\partial t} = \frac{\partial}{\partial z} \left(\Lambda \frac{\partial T}{\partial z} \right) - \mathcal{L} \rho \frac{\partial \phi_l}{\partial t}. \quad (3.67)$$

where the latent heat appears as a heat source term in the governing equation. If the specific heat c_p are explicitly independent of time, and the thermal conductivity k is independent of position, Eq. (3.67) can be written as

$$\frac{\partial T}{\partial t} = \kappa \frac{\partial^2 T}{\partial z^2} - \frac{L}{c_p} \frac{\partial \phi_l}{\partial t}. \quad (3.68)$$

Equation (3.68) in dimensionless form reads

$$\frac{\partial T}{\partial t} = \frac{\partial^2 T}{\partial z^2} - \frac{1}{St} \frac{\partial \phi_l}{\partial t}, \quad (3.69)$$

where St is the Stefan number.

Finally, to complete the physical model described by Eqs. (3.68) and (3.66), liquid fraction should be computed. One common way is by estimating liquid fraction through linear interpolation of enthalpy difference of solid ($h_s = c_p T$) and liquid ($h_l = h_s + L$) by

$$\phi_l = \begin{cases} 0 & h < h_s, \\ \frac{h-h_s}{h_l-h_s} & h_s \leq h \leq h_l, \\ 1 & h_l < h. \end{cases} \quad (3.70)$$

In order to increase the accuracy of estimation, one can repeat Eqs. (3.66), (3.68) and (3.70) until the melt fraction field converge to within a set tolerance. However, it has been observed that using one iteration has negligible effects, but becomes valuable for the computationally intensive convection melting problems. [33]

3.5.2. Nusselt number in system melting

For the system of melting, computation of Nusselt from equations (3.51) and (??) is difficult, because the average should be taken over liquid fraction, and the solid-liquid interface is versatile and time dependent. One approach can be measuring heat flux at the bottom warm boundary. Nevertheless, Nusselt number can be defined as dimensionless heat flux entering the system from bottom.

While the velocity at the bottom layer is zero (due to no-slip boundary condition for velocity), the heat flux from equation (??) gives

$$Q = -\kappa \left\langle \frac{\partial T}{\partial z} \right\rangle_A \Big|_{z=0}. \quad (3.71)$$

Non-dimensionalizing heat flux (Q) by $\kappa \Delta T / H(t)$, temperature by ΔT , and space by H_{max} (total height of the system), dimensionless Nusselt number is defined as

$$Nu = - \left\langle \frac{\partial \tilde{T}}{\partial \tilde{z}} \right\rangle_A \Big|_{\tilde{z}=0}, \quad (3.72)$$

where tilded (\sim) quantities are dimensionless and $\langle \cdot \rangle_A$ denotes the average over horizontal plane and time.

3.6. Summary

In this chapter, we presented a model system, which is dynamically equivalent to the one of the Arctic melt pond. The proposed equivalent model in this study consists of a solid layer of a pure substance, initially at a constant temperature, T_m , equal to the phase-change (melting) temperature. The solid is heated at a constant temperature $T_0 > T_m$ from the bottom. Therefore, the solid starts to melt and during the process of melting it goes through stages of conductive and convective melting. In the conduction regime with and without a bottom moving boundary, we recalled the solution of Stefan problem which depends on the similarity variable $\zeta = z / \sqrt{t}$.

In the convective regime, the mathematical formulation of phase-change problem is considered by using enthalpy formulation. In particular, the enthalpy formulation takes into account the volume-phase fraction of the liquid phase.

For reference purpose, we gave a review on the most important features of the Rayleigh-Bénard system without a phase-change. In particular, we presented an overview of some scaling laws proposed in the literature concerning the dependency of the Nusselt number on Rayleigh and Prandtl numbers.

Finally, we introduced the governing equations of the Rayleigh-Bénard system in the presence of a uniform volumetric heat source. The conductive solution is derived and will be used to validate the numerical simulations of the same problem.

References

- [1] G. Lamé and B. Clapeyron, *Mémoire sur la solidification par refroidissement d'un globe liquide*, in *Annales Chimie Physique*, Vol. 47 (1831) pp. 250–256.
- [2] L. Rubinstein, *The stefan problem american mathematical society*, Providence, Rhode Island (1971).

- [3] J. Stefan, *Über die theorie der eisbildung, insbesondere über die eisbildung im polarmeere*, *Annalen der Physik* **278**, 269 (1891).
- [4] C. Vuik, *Some historical notes about the Stefan problem* (Delft University of Technology, Faculty of Technical Mathematics and Informatics, 1993).
- [5] V. Alexiades and A. D. Solomon, *Mathematical modeling of melting and freezing processes, hemisphere publ.*, (1993).
- [6] A. Friedman, *Partial differential equations of parabolic type prentice-hall inc*, Englewood Cliffs, NJ (1964).
- [7] S. C. Gupta, *The classical Stefan problem: basic concepts, modelling and analysis*, Vol. 45 (Elsevier, 2003).
- [8] J. Crank, *Free and moving boundary problems*, Oxford Science Publications (1987).
- [9] H. Bénard, *Les tourbillons cellulaires dans une nappe liquide*, *Revue générale des Sciences pures et appliquées* **11**, 1261 (1900).
- [10] L. Rayleigh, *Lix. on convection currents in a horizontal layer of fluid, when the higher temperature is on the under side*, *The London, Edinburgh, and Dublin Philosophical Magazine and Journal of Science* **32**, 529 (1916).
- [11] M. J. Block, *Surface tension as the cause of Bénard cells and surface deformation in a liquid film*, *Nature* **178**, 650 (1956).
- [12] J. Pearson, *On convection cells induced by surface tension*, *Journal of fluid mechanics* **4**, 489 (1958).
- [13] D. Nield, *Surface tension and buoyancy effects in cellular convection*, *Journal of Fluid Mechanics* **19**, 341 (1964).
- [14] L. Landau and E. Lifshitz, *fluid mechanics*, *Course of Theoretical Physics* **6** (1959).
- [15] J. Boussinesq, *Théorie de l'écoulement tourbillonnant et tumultueux des liquides dans les lits rectilignes à grande section*, Vol. 1 (Gauthier-Villars, 1897).
- [16] L. P. Kadanoff, *Turbulent heat flow: Structures and scaling*, *Physics today* **54**, 34 (2001).
- [17] W. V. Malkus, *The heat transport and spectrum of thermal turbulence*, *Physical and Engineering Sciences* **225**, 196 (1954).
- [18] R. H. Kraichnan, *Turbulent thermal convection at arbitrary Prandtl number*, *The Physics of Fluids* **5**, 1374 (1962).
- [19] E. A. Spiegel, *Convection in stars i. basic Boussinesq convection*, *Annual review of astronomy and astrophysics* **9**, 323 (1971).
- [20] B. I. Shraiman and E. D. Siggia, *Heat transport in high-Rayleigh-number convection*, *Phys. Rev. A* **42**, 3650 (1990).
- [21] S. Cioni, S. Ciliberto, and J. Sommeria, *Strongly turbulent Rayleigh–Bénard convection in mercury: comparison with results at moderate Prandtl number*, *Journal of Fluid Mechanics* **335**, 111 (1997).
- [22] S. Grossmann and D. Lohse, *Scaling in thermal convection: a unifying theory*, *Journal of Fluid Mechanics* **407**, 27 (2000).
- [23] S. Grossmann and D. Lohse, *Thermal convection for large Prandtl numbers*, *Physical Review Letters* **86**, 3316 (2001).
- [24] S. Grossmann and D. Lohse, *Prandtl and Rayleigh number dependence of the Reynolds number in turbulent thermal convection*, *Physical Review E* **66**, 016305 (2002).

- [25] S. Grossmann and D. Lohse, *Fluctuations in turbulent Rayleigh–Bénard convection: the role of plumes*, *Physics of Fluids* **16**, 4462 (2004).
- [26] G. Ahlers, S. Grossmann, and D. Lohse, *Heat transfer and large scale dynamics in turbulent Rayleigh–Bénard convection*, *Reviews of modern physics* **81**, 503 (2009).
- [27] G. Ahlers and X. Xu, *Prandtl-number dependence of heat transport in turbulent Rayleigh–Bénard convection*, *Physical review letters* **86**, 3320 (2001).
- [28] G. Poots, *An approximate treatment of a heat conduction problem involving a two-dimensional solidification front*, *International Journal of Heat and Mass Transfer* **5**, 339 (1962).
- [29] K. A. Rathjen and L. M. Jiji, *Heat conduction with melting or freezing in a corner*, *Journal of Heat Transfer* **93**, 101 (1971).
- [30] H. Budhia and F. Kreith, *Heat transfer with melting or freezing in a wedge*, *International Journal of Heat and Mass Transfer* **16**, 195 (1973).
- [31] V. Voller, M. Cross, and N. Markatos, *An enthalpy method for convection/diffusion phase change*, *International journal for numerical methods in engineering* **24**, 271 (1987).
- [32] W. Shyy, H. Udaykumar, M. Rao, and R. Smith, *Computational fluid dynamics with moving boundaries* *tailor and francis: Washington*, (1996).
- [33] C. Huber, A. Parmigiani, B. Chopard, M. Manga, and O. Bachmann, *Lattice Boltzmann model for melting with natural convection*, *International Journal of Heat and Fluid Flow* **29**, 1469 (2008).



4

Numerical simulation of convection coupled to melting process

In this chapter, we briefly describe the Lattice Boltzmann (LB) method which we use to develop a numerical toolkit for simulating the melting problem. However, no solver can be trusted without proper validation. Therefore, in second part of this chapter, we validate our code with analytical solution presented in the previous chapter and simulations done by other researchers.

Everyone agrees that lattice Boltzmann is different from classical CFD, at the level of theory, code implementation, and the look and feel of applications. But why would we actually choose lattice Boltzmann over another approach? Opinions are a bit more divergent about this point. From our experience, we believe that the fundamental advantage of lattice Boltzmann is efficiency. The method was designed since the beginning to run on high performance hardware, and it accommodates for complex physics or sophisticated algorithms. Efficiency leads to a qualitatively new user experience when it allows to solve problems that could not be approached before, or only with insufficient accuracy. Typical achievements of a lattice Boltzmann code are

- Data pre-processing and mesh generation in a time that accounts for a small fraction of the total simulation only.
- Parallel data analysis, post-processing and evaluation, which is not something specific of the LB method.
- Fully resolved flow through complex geometries and porous media.
- Complex, coupled flow with heat transfer and chemical reactions.

Lattice Boltzmann also offers advantages at the level of the modeling approach. The method is in some sense hybrid, because the solver is mesh based (as usual in CFD), but also inherits some aspects of a particle based method, due to its origins from Cellular Automata. It is therefore easy to couple it with embedded particle methods, for sediment transport or other phenomena.



Despite the increasing popularity of LBM in simulating complex fluid systems, this novel approach has some limitations. For instance, presently high-Mach number flows in aerodynamics are still difficult for LBM. However, as with Navier–Stokes based CFD, LBM has been successfully coupled to thermal-specific solutions to enable heat transfer (solids-based conduction, convection and radiation) simulation capability.

4.1. The Lattice Boltzmann method

During the last two decades, the Lattice Boltzmann method (LB) has developed as a promising tool for modelling the Navier–Stokes equations and simulating complex fluid flows. Primarily, the LB method developed from lattice gas automata [1], however later, it established as an independent numerical method driven from direct discretization of Boltzmann - BGK¹ equation [2]. LB is based on microscopic models and mesoscopic kinetic equations. However, the central topic of the theoretical background for the lattice Boltzmann method is how to derive from the kinetic Boltzmann - BGK equation formulated for particle distribution function to macroscopic conservation equations with thermodynamic variables such as density, momentum and energy [3].

In some perspective, the LB method can be viewed as a finite difference method for solving the Boltzmann transport equation. The Navier–Stokes equations can be recovered by the LB method with a proper choice of the collision operator [4].

The materials described in this section are fundamentals of the LB method and used in order to develop a code simulating melting process and fluids flow. Reader is advised to refer to more complete sources, *e.g.* "The Lattice Boltzmann Equation for Fluid Dynamics and Beyond" by S. Succi [4].

4.1.1. Lattice Boltzmann model

The Lattice Boltzmann method [5–7] was originated from Ludwig Boltzmann's kinetic theory of gases. The fundamental idea is that gases/fluids can be imagined as consisting of a large number of small particles moving with random motions. The exchange of momentum and energy is achieved through streaming and collision of particles. This process can be modeled by the Boltzmann transport equation, which is

$$\frac{\partial f}{\partial t} + \mathbf{c} \cdot \nabla f = \Omega, \quad (4.1)$$

where $f(\mathbf{x}, t)$, \mathbf{c} and Ω are the particle distribution function, the particle velocity, and the collision operator respectively. For the simulations in the present study we consider for simplicity the collision operator proposed by BGK, which is given by

$$\Omega_i(f) = -\frac{\delta t}{\tau} (f_i - f_i^{eq}), \quad (4.2)$$

where f_i^{eq} is a local equilibrium value for the population of particles in the direction of link \mathbf{c}_i . The term τ is a relaxation time, and related to the viscosity.

The LBM simplifies Boltzmann's original idea of gas dynamics by reducing the number of particles and confining them to the nodes of a lattice. Particles are restricted to

¹Bhatnagar–Gross–Krook

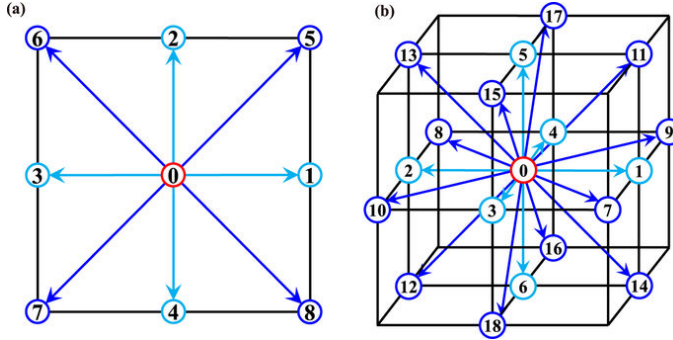


Figure 4.1 – Lattice in two-dimension (a) and three-dimension (b) used in our numerical method. The 2D has nine velocities, whereas 3D has nineteen. Colors indicates different velocities which are explained in the text.

stream in a possible of nine directions in the 2D configuration (D2Q9), and nineteen directions in 3D (D3Q19), including the one staying at rest. These velocities are referred to as the microscopic velocities and denoted by \vec{c}_i . Figure 4.1 shows two typical lattice node of D2Q9 and D3Q19 models, which we use in our simulation and they guaranty recovery of Navier-Stokes equation in the microscopic limit.

For each microscopic velocity vector on the lattice, we associate a discrete probability distribution function $f(\vec{x}, \vec{c}_i, t)$ or simply $f_i(\vec{x}, t)$, which describes the probability of streaming in one particular direction. With respect to $f_i(\vec{x}, t)$, the macroscopic quantities are given by moments of the distribution function. The macroscopic fluid density is defined as the first order moment, which is a summation of microscopic distribution function (population),

$$\rho(\vec{x}, t) = \sum_i f_i(\vec{x}, t). \quad (4.3)$$

Accordingly, the macroscopic momentum $\rho \vec{u}(\vec{x}, t)$ is an average of discrete velocities \vec{c}_i weighted by the distribution functions f_i ,

$$\rho \vec{u}(\vec{x}, t) = \sum_i f_i(\vec{x}, t) \vec{c}_i. \quad (4.4)$$

Lattice-Boltzmann algorithm is defined through two steps, collision and streaming. Theoretically, the collision step is when particles collide over a discrete lattice mesh, and is defined as

$$f_i^*(\vec{x}, t) = f_i(\vec{x}, t) + \frac{\delta t}{\tau_u} (f_i^{eq}(\vec{x}, t) - f_i(\vec{x}, t)), \quad (4.5)$$

where the * denotes the post collision discrete distribution function. After collision of fictive particles, they propagate over lattice mesh, which is known as streaming

$$f_i(\vec{x} + \vec{c}_i \delta t, t + \delta t) = f_i^*(\vec{x}, t). \quad (4.6)$$

In the collision term step, $f_i^{eq}(\vec{x}, t)$ is the equilibrium distribution, and τ_u is considered as the relaxation time towards local equilibrium. Equilibrium distribution is given

by:

$$f_i^{eq} = \rho w_i \left[1 + \frac{\bar{u} \cdot \bar{c}_i}{c_s^2} + \frac{(\bar{u} \cdot \bar{c}_i)^2}{2c_s^4} - \frac{\bar{u} \cdot \bar{u}}{2c_s^2} \right], \quad (4.7)$$

where \bar{c}_i and \bar{u}_i are the discrete and the microscopic fluid flow velocities, respectively.

The weights w_i depend on the set of velocities. The values of weights are tuned to recover the isotropy of the continuous Boltzmann equation, and are given by:

$$\begin{aligned} \text{D2Q9} \quad w_i &= \begin{cases} 4/9 & i = 0 \\ 1/9 & i = 1, \dots, 4 \\ 1/36 & i = 5, \dots, 8 \end{cases} \\ \text{D3Q19} \quad w_i &= \begin{cases} 1/3 & i = 0 \\ 1/18 & i = 1, \dots, 6 \\ 1/36 & i = 7, \dots, 18 \end{cases} \end{aligned}$$

With an appropriate equilibrium distribution function and defining $c_s^2 = (1/3)\delta x^2/\delta t^2$, in which c_s represents the isothermal model's speed of sound, one can recover the continuity and Navier-Stokes equation through a Chapman-Enskog expansion [8–10]. Accordingly, the pressure is defined as $p = \rho c_s^2$ and the kinematic viscosity is defined by

$$\nu = c_s^2 \left(\tau_u - \frac{\delta t}{2} \right), \quad (4.8)$$

where δt is the time step. Positive kinematic viscosity requires that $\tau_u > 0.5$. For further information, the reader is advised to refer to Lattice Boltzmann textbooks [4, 11, 12].

4.1.2. Advection-diffusion equation for the temperature field with the LB method

The third order moment of distribution function, which is the energy, can be used to describe the temperature. This method is called thermal Lattice Boltzmann and has been used relatively less than other methods. In the present work, however, we use multi-distribution function (MDF) approach [13, 14] to model natural convection. In MDF method, the thermal advection-diffusion is solved by introducing a second distribution function (g_i) whose evolution is also described by a LBGK dynamic.

$$g_i(\bar{x} + \bar{c}_i, t + 1) = g_i(\bar{x}, t) - \frac{\delta t}{\tau_t} (g_i(\bar{x}, t) - g_i^{eq}(\bar{x}, t)). \quad (4.9)$$

The LBGK model for g_i^{eq} is similar to f_i^{eq} and the equilibrium distribution function is

$$g_i^{eq} = T w_i \left[1 + \frac{\bar{u} \cdot \bar{c}_i}{c_s^2} + \frac{(\bar{u} \cdot \bar{c}_i)^2}{2c_s^4} - \frac{\bar{u} \cdot \bar{u}}{2c_s^2} \right], \quad (4.10)$$

where \bar{u} is the macroscopic fluid flow velocity. For simplicity, in our model we use the same LBGK model for fluid and thermal distributions, and thus, we have same weights w_i in both equilibrium equations.

At each lattice node, the macroscopic temperature is defined as

$$T = \sum_i g_i(\vec{x}, t), \quad (4.11)$$

and the thermal diffusivity (in lattice units) is related to the relaxation time

$$\kappa = c_s^2 \left(\tau_t - \frac{\delta t}{2} \right). \quad (4.12)$$

The MDF approach offers the possibility to vary the Prandtl number by adjusting the two relaxation times τ_u and τ_t ,

$$Pr = \frac{2\tau_u - \delta t}{2\tau_t - \delta t}. \quad (4.13)$$

Ideally, the incompressibility can be achieved only when the mass density becomes a constant. However, it is practically impossible to maintain a constant density in the LB models. Theoretically the LB equation always simulates the compressible Navier-Stokes equation instead of the incompressible one, because the spatial density variation is not zero in LBE simulations. In order to correctly simulate the incompressible Navier-Stokes equation in practice, one must ensure that the Mach number, and the density variation, $\delta\rho$, are of the order $O(\epsilon)$ and $O(\epsilon^2)$, respectively, where ϵ is the Knudsen number². [15]

4.1.3. Boussinesq equation system with the LB method

One of the most important applications of the advection-diffusion model is the thermal flows where the advection and diffusion of heat is coupled to the dynamics of the ambient fluid. In this case, the velocity \mathbf{u} is provided by a Navier-Stokes solver, e.g. the LBM, whereas temperature acts back on the fluid. This feedback is often modeled as, but not always limited to, a temperature-density coupling. For example, the Boussinesq approximation assumes a temperature-dependent fluid density that can be modeled as a buoyancy force instead of changing the simulation density. Therefore, in the Boussinesq system the temperature is not a passive scalar and it reacts to the fluid. Furthermore, the temperature may have source terms. Therefore, in order to treat this problems we use

$$f_i(\vec{x} + \vec{c}_i, t + \delta t) = f_i(\vec{x}, t) - \frac{1}{\tau_u} (f_i(\vec{x}, t) - f_i^{eq}(\vec{x}, t)) + \vec{F}_i, \quad (4.14)$$

with the forcing term F_i added to the equation for f_i in order to model the buoyancy force as represented in the Boussinesq approximation and is defined as

$$\vec{F}_i = \left(1 - \frac{1}{2\tau_u} \right) \rho w_i \left(\frac{c_i \cdot \vec{u}}{3} + \frac{(c_i \cdot \vec{u}) c_i}{9} \right) \beta (T - T_0) \vec{g}, \quad (4.15)$$

where T_0 is the reference temperature. Similarly, for temperature population we use

$$g_i(\vec{x} + \vec{c}_i, t + \delta t) = g_i(\vec{x}, t) - \frac{\delta t}{\tau_t} (g_i(\vec{x}, t) - g_i^{eq}(\vec{x}, t)) + \vec{Q}_i, \quad (4.16)$$

²The Knudsen number is a dimensionless number defined as the ratio of the molecular mean free path length to a representative physical length scale. This length scale could be, for example, the radius of a body in a fluid. The number is named after Danish physicist Martin Knudsen (1871-1949).

with Q_i , the temperature source term, can be internal heating or melting process, and corresponds to the source term q in

$$\frac{\partial T}{\partial t} + (\nabla \cdot \vec{u})T = \kappa \nabla^2 T + q, \quad (4.17)$$

and is defined [12] by

$$Q_i = w_i q. \quad (4.18)$$

4.1.4. Boundary conditions

Boundary conditions have to be treated carefully for conventional numerical methods, such as finite element method, to solve any differential system. In a similar way, imposing boundary conditions accurately is crucial for lattice Boltzmann method. There are two distinct kinds of boundary conditions for macroscopic system in our model. Dirichlet boundary conditions which specify the value of the field on the boundary and we use to specify no-slip boundary condition for velocity or constant temperatures at the bottom and top boundary, and the liquid-solid interface. For the latter, we use a numerical technique known as enthalpy method and we will describe it thoroughly later. Here, we describe briefly the implementation of Dirichlet and periodic boundary conditions.

No-slip boundary condition for velocity

Bounce-back BCs are typically used to implement no-slip conditions on the boundary. By the so-called bounce-back we mean that when a fluid particle (discrete distribution function) reaches a boundary node, the particle will scatter back to the fluid along with its incoming direction. Bounce-back BCs come in a few variants and we focus on two types of implementations: the on-grid and the mid-grid bounce-back [4].

The idea of the on-grid bounce-back is particularly simple and preserves a first-order space numerical accuracy. In this configuration, the boundary of the fluid domain is aligned with the lattice points. One can use a boolean mask for the boundary and the interior nodes. The incoming directions of the distribution functions are reversed when encountering a boundary node. This implementation does not distinguish the orientation of the boundaries and is ideal for simulating fluid flows in complex geometries, such as the porous media flow.

The configuration of the mid-grid bounce-back introduces fictitious nodes and places the boundary wall centered between fictitious nodes and boundary nodes of the fluid (see Figure 4.2). At a given time step t , the distribution functions with directions towards the boundary wall would leave the domain. Collision process is then applied and directions of these distribution functions are reversed and they bounce back to the boundary nodes. We point out that the distribution functions at the end of bounce-back in this configuration is the post-collision distribution functions.

Although the on-grid bounce-back is easy to implement, it has been verified that it is only first-order accurate in space due to its one-sided treatment on streaming at the boundary. However the centered nature of the mid-grid bounce-back leads to a second order of accuracy at the price of a modest complication.

The simplest way of implementing mid-grid bounce-back is to draw the boundary and then mark all links that are cut by this boundary. Such an implementation can be



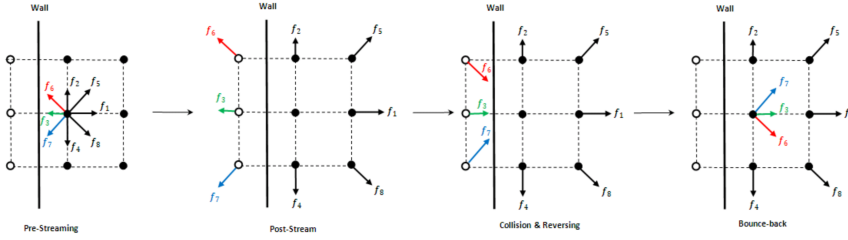


Figure 4.2 – Illustration of mid-grid bounce-back.

analytically summarized as

$$f_i(\vec{x}, t + \delta t) = f_{-i}(\vec{x}, t + \delta t), \quad (4.19)$$

where the velocity index $-i$ is defined through $c_{-i} = -c_i$. The effective boundary then lies halfway between the links.

Constant boundary conditions for velocity and temperature

In this section the boundary condition is described based on the idea of bounce-back of the non-equilibrium part. As an example, take the case of a bottom node in Fig. 4.1. The boundary is aligned with the x -direction with f_4, f_7, f_8 pointing into the wall. After streaming, $f_0, f_1, f_3, f_4, f_7, f_8$ are known. Suppose that u_x, u_y are specified on the wall and we want to use equations 4.3 and 4.4 to determine f_2, f_5, f_6 and ρ , which can be put into the form

$$f_2 + f_5 + f_6 = \rho - (f_0 + f_1 + f_3 + f_4 + f_7 + f_8), \quad (4.20)$$

$$f_5 - f_6 = \rho u_x - (f_1 - f_3 - f_7 + f_8), \quad (4.21)$$

$$f_2 + f_5 + f_6 = \rho u_y + (f_4 + f_7 + f_8). \quad (4.22)$$

Consistency of Eqs. 4.20 and 4.22 gives

$$\rho = \frac{1}{1 - u_y} (f_0 + f_1 + f_3 + 2(f_4 + f_7 + f_8)). \quad (4.23)$$

However, f_2, f_5 and f_6 remain undetermined. To close the system, we assume the bounce-back rule is still correct for the non-equilibrium part of the particle distribution normal to the boundary (in this case, $f_2 - f_2^{eq} = f_4 - f_4^{eq}$). With f_2 known, f_5, f_6 can be found, thus

$$f_2 = f_4 + \frac{2}{3}\rho u_y, \quad (4.24)$$

$$f_5 = f_7 - \frac{1}{2}(f_1 - f_3) + \frac{1}{2}\rho u_x + \frac{1}{6}\rho u_y, \quad (4.25)$$

$$f_6 = f_8 + \frac{1}{2}(f_1 - f_3) - \frac{1}{2}\rho u_x + \frac{1}{6}\rho u_y. \quad (4.26)$$

Finally, the collision step is applied to the boundary nodes also.

For imposed temperature boundary condition for the population g_i , we compute similarly

$$g_3 = T_0(w_5 + w_3) - g_5, \quad (4.27)$$

$$g_8 = T_0(w_6 + w_8) - g_6, \quad (4.28)$$

$$g_9 = T_0(w_7 + w_9) - g_7. \quad (4.29)$$

Simulation of phase-change process

There are many physical problems that involve multiphase systems, in which the interface between phases is clearly defined but not at a fixed location. The interface can be assumed to be a planar surface in these situations, and therefore a continuum approach is valid. In these problems, it is necessary to solve for both the phases as well as the interfacial location. These problems can be solved numerically on an Eulerian (front capturing fixed grid methods such as for instance the enthalpy method) or Lagrangian mesh (front tracking moving boundary methods).

An Eulerian mesh is stationary and defined prior to the start of a solution. When using an Eulerian mesh, the interface is tracked by solving an additional scalar equation. In the Lagrangian approach, a boundary of the mesh is aligned with the interface, and this boundary moves with the interface.

When thinking of a multiphase system from a continuum approach, in the bulk region a phase is continuous and is discontinuous at an interface between different phases. In general, the interface is free to deform based on the nature of the flow; therefore, it is difficult to efficiently capture an interface between phases with just one model. Consequently, there have been strong efforts to track an interface based on several different techniques. Each of these approaches has its own advantages, if front tracking allows in general for a smoother resolution of the interface, the enthalpy method has revealed to be simple in its implementations, particularly in three-dimensional setups.

For a benchmark review on the accuracy of the different methods one can see [16]. More recently Ulvrova *et al.* [17] have addressed the problem of basal melting in a geophysical context and have compared the performances of the two mentioned approaches. The studies mentioned so far were based on classical computational fluid dynamics approaches, based either on finite volumes or finite differences discretizations of the fluid-dynamics conservation equations.

In Lattice-boltzman method, many mesoscopic approaches have been proposed for the treatment of solid-liquid phase transition in the LB context. However, the method that we adopted in our work, is based on enthalpy method which is a microscopic method.

In this DNS model, we use a slightly modified version of the Jiaung *et al.* [18] melting scheme for the conduction case, using a $D2Q9$ and $D3Q19$ topology for respectively $2D$ and $3D$ system, which was first used by Huber *et al.* [19]. Jiaung *et al.* use an iterative enthalpy-based method to solve for both the temperature and melt fraction fields at each time step. The melting term is introduced as a source (crystallization) or sink (melting) term in the collision step. In summary, at the time-step n , the macroscopic temperature is calculated

$$T(t_n) = \sum_i g_i(t_n). \quad (4.30)$$

4.2. Validation

We proceed to the evaluation of the total local enthalpy:

$$\mathcal{H}(t_n) = c_p T(t_n) + \mathcal{L} \phi_l(t_{n-1}). \quad (4.31)$$

Such a quantity is used to estimate the melt fraction at time t_n through a linear interpolation:

$$\phi_l(t_n) = \begin{cases} 0 & \mathcal{H}(t_n) < \mathcal{H}_s, \\ \frac{\mathcal{H}(t_n) - \mathcal{H}_s}{\mathcal{L}} & \mathcal{H}_s \leq \mathcal{H}(t_n) \leq \mathcal{H}_l, \\ 1 & \mathcal{H}(t_n) > \mathcal{H}_l, \end{cases} \quad (4.32)$$

and finally the liquid fraction increment is estimated by a first-order finite difference

$$\frac{\partial \phi_l}{\partial t}(t_n) \simeq \frac{\phi_l(t_n) - \phi_l(t_{n-1})}{t_n - t_{n-1}}. \quad (4.33)$$

Such a term is used to define a source term in the temperature equation. Finally, in order to correct the temperature field, we use the LB algorithm for the temperature population. In order to increase the precision of such an algorithm, one could repeat the above procedure iteratively at time step t_n ; however, it has been shown in [19] that one iteration is sufficient to reach a good agreement with the known analytical conductive result.

In order to avoid the possibility to have deformation of the solid, due to the artificial creation of velocity in this part of the domain, we apply the following two corrections. First, all external fluid forces are weighted proportionally to the local liquid fraction ϕ_l . This means in the specific case that the buoyancy force does not act on the solid phase. Second, we apply a penalization force in the solid part, which acts as high viscosity, and is defined as

$$\mathbf{f}_p = -\chi(\phi_l)\mathbf{u}. \quad (4.34)$$

We have checked that the specific form of the penalisation mask $\chi(\phi_l)$ does not affect the results (we employed here $\chi(\phi_l) = 1 - \phi_l^2$). The penalisation method in the context of LB algorithm for phase-change has been proposed in [20]. Other authors, e.g. [17], have imposed viscosity strongly (i.e. exponentially) dependent on the liquid fraction.

In the following parts, we will validate our algorithm by thorough checks against known solutions for the Stefan problem, as well as comparison with other numerical results in configurations for convective melting with lateral heat source [21].

4.2. Validation

In this section we present the results of both conduction and convection melting with our lattice Boltzmann model and compare them with analytical solutions (for the conduction case) and with the scaling obtained by Gobin, et al. (2000) [22]. For all the test in this section, we use the thermal diffusivity set to value $\kappa = 0.02$ and the kinematic viscosity of $\nu = 0.2$, which corresponds to $Pr = 10$.

The simulations presented in this work have been computed by the mean of a code developed at the laboratory of mechanics and publicly accessible on [github](#).

4.2.1. Melting in conductive condition

A first test is the calculation of the Stefan conductive melting problem. Several simulations have been performed on a 2D domain of grid size $L_x \times L_y = 50 \times 50$. Specific heat $c_p = 1$, while the latent heat is set to three different values $\mathcal{L} = 100, 10, 1$, which lead to Stefan number values of $St = 0.01, 0.1, 1$. The temperature differences between plate and the temperature of solid is the same in all the cases and equal to $\Delta T = 1$.

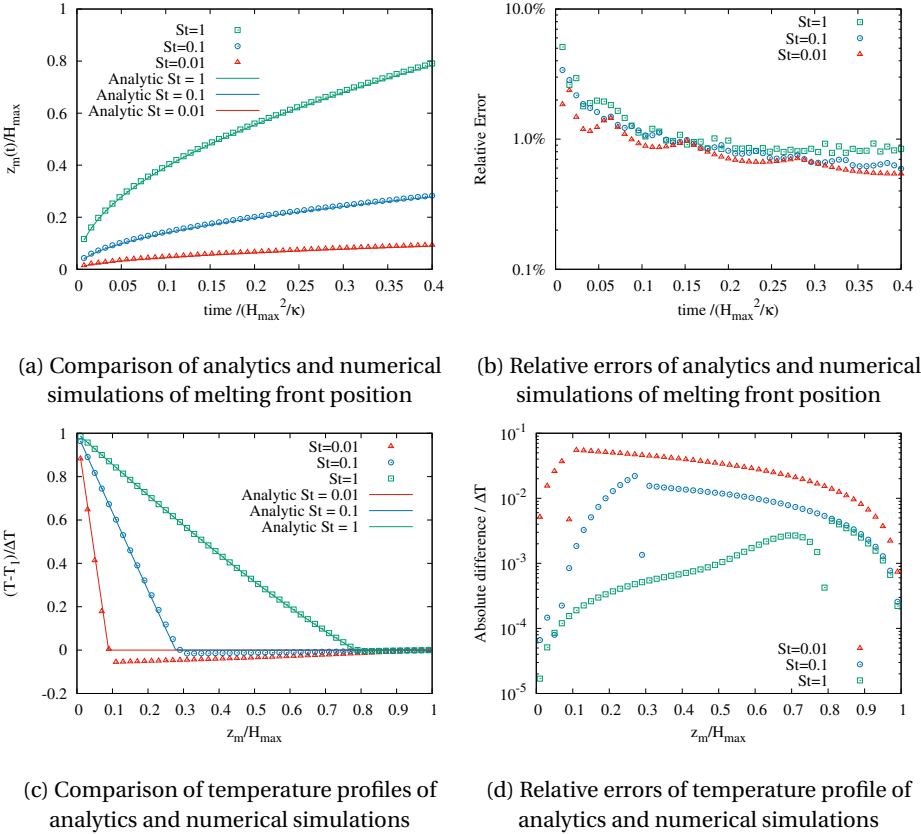


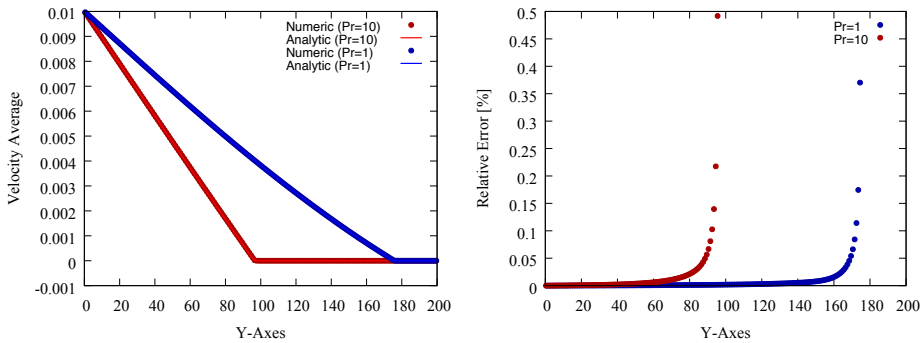
Figure 4.3 – Comparison of numerical and analytical results for the melting system in conductive conditions (Stefan problem)

In Fig. 4.3a we compare the position of the melting front $H(t)$ as a function of time with the analytical solution Eq. (3.28). The agreement with the analytical solution is overall good for all the St numbers. The relative error decreases with time, Fig 4.3b, however we observe a relatively large error in the initial stages of the simulation, particularly for the largest St number. This is expected because, according to the Stefan solution, the velocity of the front increases with St and, more importantly, it is singular (infinite) at the origin. Therefore, independently of the numerical method adopted, it is expected that in the initial stages of the simulations the error will be large.

Moreover, in Fig. 4.3c we compare the temperature profile normalized by the temperature difference as a function of time with the analytical solution Eq. (3.27). Similarly, the analytical solution is in good agreement for all the St numbers. Likewise, the relative error decreases with time, Fig 4.3d.

Similarly, we validate the DNS results of conduction melting with presence of slip velocity at the bottom boundary. The validation is for two Prandtl numbers ($Pr = 1$ and $Pr = 10$), for a 2D system of size 200×200 . In both cases, the specific and latent heat are $c_p = 1$ and $\mathcal{L} = 1$ which corresponds to the Stefan number $St = 1$, and the temperature difference is $\Delta T = 1$.

The analytical solutions for temperature and velocity field are Eqs. (3.27) and (3.36), respectively. As the solution of temperature field is the same as pure conductive melting and the validation of temperature field performed in previous part, there is no further need for comparison between analytical solution and numerical one. However, for the velocity field of numerical simulation, we take average over horizontal axes. The result of numerical simulations and analytical solutions is shown in Fig. 4.4a. As it can be observed, the numerical results and the analytical solutions are in good agreement.



(a) Comparison of analytics and numerical simulations of velocity average

(b) Relative errors of analytics and numerical simulations of velocity average

Figure 4.4 – Comparison of numerical and analytical results for the melting system coupled with moving boundary in conductive conditions.

Similarly to pure conductive case, one can look the relative errors of the two analytical solutions and numerical results, which are shown in Fig. 4.4b. The error increases near the melting front, however, one should notice that the analytical solution approaches zero near solid-liquid interface. Consequently, division by small number results in great error. In the solid part, the magnitude of velocity field is zero, and therefore theoretically the relative error is undefined.

4.2.2. Rayleigh-Bénard convection

The two-dimensional convection pattern characterized by the rolls is unstable at higher Rayleigh numbers (Fig. 4.5). As the Rayleigh number is increased, a series of transitions to more complicated states occur, and the form of the convection becomes time depen-

dent, and eventually turbulent at very high Rayleigh number. Detailed numerical simulation of all the complicated transitions and the different forms of convection requires a large amount of computation. This is because the form of the convection depends on both the initial condition (e.g. the initial perturbation) and the boundary conditions. A large number of runs have to be performed to cover the parameter space. In addition, the computation has to be carried out for a long time (turnover time) due to the large differences among the time scales in the problem. Here we only present the simulation results for a few typical situations at moderate Rayleigh numbers in order to validate the performance of our DNS code.

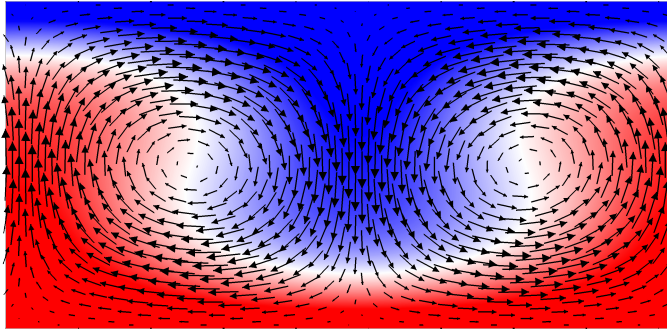


Figure 4.5 – Visualization of Rayleigh-Bénard system with periodic lateral boundary and Rayleigh number $Ra = 4552.7$

Several two-dimensional simulations with different Rayleigh numbers are performed on a 202×100 lattice with a Prandtl number $Pr = 1$. The lateral boundary conditions are periodic and the system is heated from below and cooled from top with temperature difference of $\Delta T = 1$.

A simulation was started from the static conductive state, beginning with $Ra = 2000$. After the steady state was reached, the Rayleigh number was raised step by step to higher values by increasing thermal coefficient of expansion (β). The Nusselt numbers measured at the steady states are plotted in Fig. 4.6 against the Rayleigh number. The simulation results of Clever and Busse [23], and LBE of Shan [13] are also plotted for comparison. The present results are in good agreement with the references.

4.2.3. Conductive Rayleigh-Bénard system with internal heating

In order to validate the numerical code for the case of volumetric bulk heating, we use the system of liquid heated from the bottom and cooled from the top with constant temperatures, and internally heated. The equation describing the temperature profile of such a system is Eq. (3.64).

For the numerical simulations, we use a system of 200×200 grid size in liquid state confined between two parallel plates, heated with constant temperature $T_0 = 1$ from the bottom, and cooled from the top with constant temperature $T_1 = 0$. We also use three different bulk-heating coefficients ($Q = 2, 10$ and 20). The plot of the average of the temperature field along the vertical direction is shown in Fig. 4.7. The magnitudes of internal

heating, which are presented here for the system with height $H = 200$, correspond to the same dimensional bulk-heating coefficients ($\frac{q}{\rho_0 c_p}$) we later present in chapter 7.

It is important to notice that Eq. (3.64) is the solution of the temperature profile of the mentioned numerical system. Therefore, the accuracy of results would increase with respect to the number of iterations in the numerical simulation. However, for the purpose of comparison, we choose one hundred thousand iterations in our simulations and the result is shown in Fig. 4.7a.

In order to quantitatively observe the accuracy of the numerical simulations, we consider the relative error of the numerical results to the analytical solution of the temperature profile, which is shown in Fig. 4.7b. As one can notice, the relative error increases with respect to magnitude of bulk-heating for the same number of iterations. However, for the largest internal heating, the relative error is always less than 0.7%.

4.2.4. Melting due to thermal convection

In this part, we compare the result of our DNS code in convective regime with results of Gobin et al. (2000) [22], which is a collection of results of thirteen contributors to an exercise covering a great variety of mathematical models and numerical procedures most commonly used in the field of fluid dynamics.

Convection simulation was performed for a square geometry, with the number of lattice points fixed by the value of the desired Rayleigh number. The grid size is $L_x \times L_y = 500 \times 500$ for the Rayleigh number $Ra = 10^7$, the Stefan number $St = 0.1$, and the Prandtl number $Pr = 50$. The visualization of the result is shown in Fig. 4.8.

The evolution of the average melting front position (Fig 4.9b) and the Nusselt number³ (Fig. 4.9a) are in good agreement with the main trend of results showed in Gobin et

³Nusselt number is computed using equation (3.72)

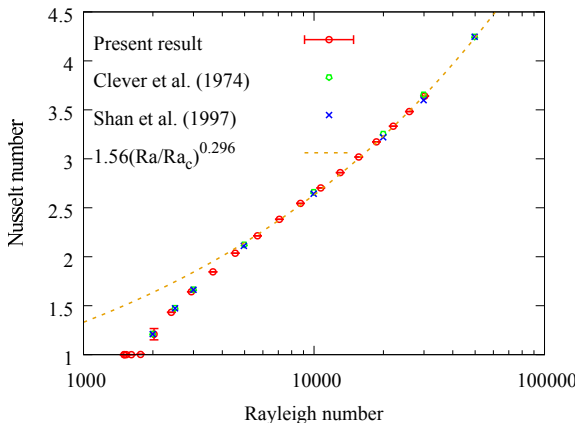


Figure 4.6 – The steady-state Nusselt number as a function of the Rayleigh number in 2D simulations. The results of the present study are in good agreement with those of Clever and Busse [23], and LBE of Shan [13].

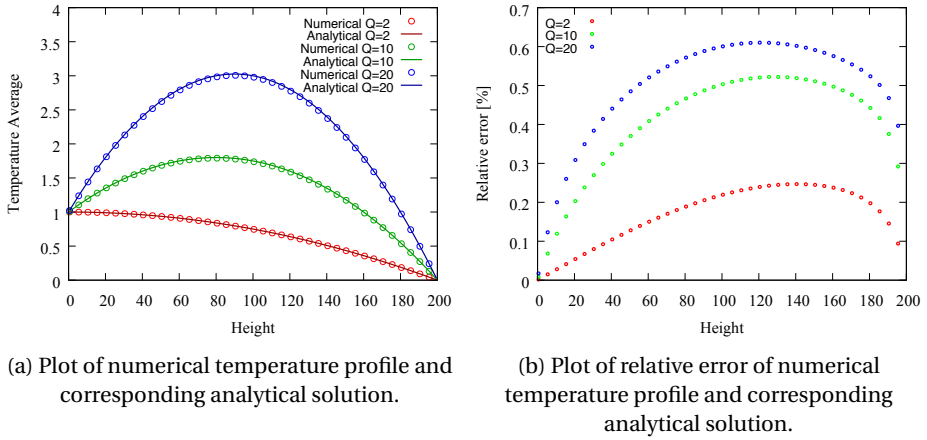


Figure 4.7 – Plots of temperature profile of numerical simulations of RB system with internal heating in conductive regime with three different bulk heating coefficients of $Q = 2, 10$ and 20 .

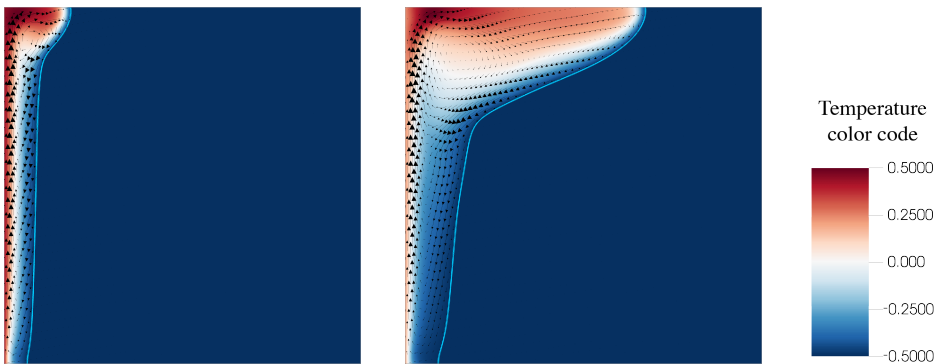


Figure 4.8 – Visualization of lateral melting for the square system of size 200 with $Ra = 10^7$, $Pr = 50$ and $St = 0.1$ at $\tilde{t} = 1$ and $\tilde{t} = 5$, where $\tilde{t} = \kappa t / H^2$. Red color ($T = 0.5$) is warm and blue ($T = -0.5$) represents cold temperature. The arrows are the velocity field.

al. The relatively high Nusselt number and oscillatory nature of the results are similar to the results of Gobin-Vieira and Couturier-Sadat listed in Gobin et al. (2000), where they attribute this behaviour to the full transient procedure and the evolution of the circulation cells as melting proceeds.

4.3. Summary

Through this chapter, we described the Lattice Boltzmann method, which is one of the well-known numerical method that has developed during the last two decades. Unlike the traditional CFD methods, which solve the conservation equations of macroscopic properties (*i.e.*, mass, momentum, and energy) numerically, LBM models the fluid con-

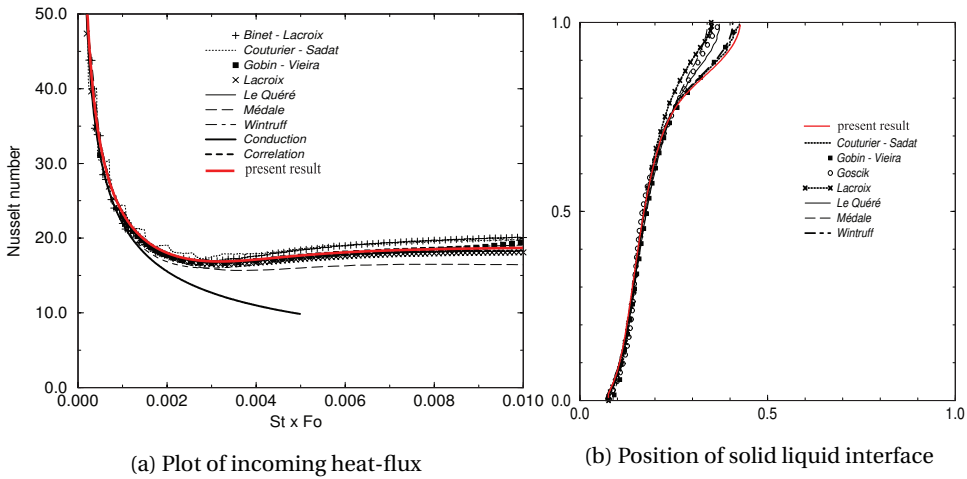


Figure 4.9 – Comparison of numerical results for the melting system in convective conditions with Gobin *et al.* [22] and Bertrand *et al.* [21]. In the panel (a), Fo is the Fourier Number, and in the panel (b), the width and height of the figure is normalized by the total length and height.

sisting of fictive particles, and such particles perform consecutive propagation and collision processes over a discrete lattice mesh. Due to its mesoscopic nature and local dynamics, LBM has several advantages over other conventional CFD methods, especially in dealing with complex boundaries, incorporating microscopic interactions, and parallelization of the algorithm. A different interpretation of the Lattice Boltzmann equation is that of a discrete-velocity Boltzmann equation. The numerical methods of solution of the system of partial differential equations then give rise to a discrete map, which can be interpreted as the propagation and collision of fictitious particles.

In the second part of this chapter, the DNS code, that is developed for simulation of melting system, is validated. The validation is for conductive melting, with and without moving boundary, by using comparison with the mathematical solution of the Stefan problem. For the case of natural convection (Rayleigh-Bénard system) and convective melting, the results of our simulations are validated through works of other researchers.

Having a direct numerical solver in hand, next step will be to analyze convective melting using our simulator. In the next chapter, we show the behaviour of melting system due to natural thermal convection.

References

- [1] F. Higuera and J. Jimenez, *Boltzmann approach to lattice gas simulations*, EPL (Europhysics Letters) **9**, 663 (1989).
- [2] X. He and L.-S. Luo, *Theory of the lattice Boltzmann method: From the Boltzmann equation to the lattice Boltzmann equation*, Physical Review E **56**, 6811 (1997).
- [3] X. Shan, X.-F. Yuan, and H. Chen, *Kinetic theory representation of hydrodynamics: a way beyond the Navier-Stokes equation*, Journal of Fluid Mechanics **550**, 413 (2006).

- [4] S. Succi, *The lattice Boltzmann equation: for fluid dynamics and beyond* (Oxford university press, 2001).
- [5] Z. Guo, B. Shi, and N. Wang, *Lattice bgk model for incompressible Navier-Stokes equation*, *Journal of Computational Physics* **165**, 288 (2000).
- [6] D. T. Thorne and C. Michael, *Lattice Boltzmann modeling: an introduction for geoscientists and engineers*, 2nd. ed. (2006).
- [7] R. Begum and M. A. Basit, *Lattice Boltzmann method and its applications to fluid flow problems*, *European Journal of Scientific Research* **22**, 216 (2008).
- [8] U. Frisch, B. Hasslacher, and Y. Pomeau, *Lattice-gas automata for the Navier-Stokes equation*, *Physical review letters* **56**, 1505 (1986).
- [9] Y. Qian, D. d'Humières, and P. Lallemand, *Lattice BGK models for Navier-Stokes equation*, *EPL (Europhysics Letters)* **17**, 479 (1992).
- [10] B. Chopard and M. Droz, *Cellular automata modeling of physical systems. collection aléa-saclay: Monographs and texts in statistical physics*, (1998).
- [11] D. A. Wolf-Gladrow, *Lattice-gas cellular automata and lattice Boltzmann models: an introduction* (Springer, 2004).
- [12] T. Krüger, *The lattice Boltzmann method : principles and practice* (Springer, Switzerland, 2016).
- [13] X. Shan, *Simulation of Rayleigh-Bénard convection using a lattice Boltzmann method*, *Physical Review E* **55**, 2780 (1997).
- [14] Z. Guo, B. Shi, and C. Zheng, *A coupled lattice bgk model for the boussinesq equations*, *International Journal for Numerical Methods in Fluids* **39**, 325 (2002).
- [15] X. He and L.-S. Luo, *Lattice Boltzmann model for the incompressible Navier-Stokes equation*, *Journal of statistical Physics* **88**, 927 (1997).
- [16] O. Bertrand, B. Binet, H. Combeau, S. Couturier, Y. Delannoy, D. Gobin, M. Lacroix, P. L. Quéré, M. Médale, J. Mencinger, H. Sadat, and G. Vieira, *Melting driven by natural convection a comparison exercise: first results*, *International Journal of Thermal Sciences* **38**, 5 (1999).
- [17] M. Ulvrová, S. Labrosse, N. Coltice, P. Råback, and P. Tackley, *Numerical modelling of convection interacting with a melting and solidification front: Application to the thermal evolution of the basal magma ocean*, *Physics of the Earth and Planetary Interiors* **206**, 51 (2012).
- [18] C.-P. K. Wen-Shu Jiaung, Jeng-Rong Ho, *Lattice Boltzmann method for the heat conduction problem with phase change*, *Numerical Heat Transfer, Part B: Fundamentals* **39**, 167 (2001).
- [19] C. Huber, A. Parmigiani, B. Chopard, M. Manga, and O. Bachmann, *Lattice Boltzmann model for melting with natural convection*, *International Journal of Heat and Fluid Flow* **29**, 1469 (2008).
- [20] D. Chatterjee and S. Chakraborty, *An enthalpy-based lattice Boltzmann model for diffusion dominated solid-liquid phase transformation*, *Physics Letters A* **341**, 320 (2005).
- [21] O. Bertrand, B. Binet, H. Combeau, S. Couturier, Y. Delannoy, D. Gobin, M. Lacroix, P. Le Quéré, M. Médale, J. Mencinger, *et al.*, *Melting driven by natural convection a comparison exercise: first results*, *International Journal of Thermal Sciences* **38**, 5 (1999).

- [22] D. Gobin and P. Le Quéré, *Melting from an isothermal vertical wall. synthesis of a numerical comparison exercise*, Computer Assisted Mechanics and Engineering Sciences **7**, 289 (2000).
- [23] R. Clever and F. Busse, *Transition to time-dependent convection*, Journal of Fluid Mechanics **65**, 625 (1974).



5

Convective melting system

5.1. Introduction

In the present chapter, we investigate the behaviour of a model system in which a pure substance initially in the solid state is progressively melted by a horizontal heat wall. The melt fluid layer is thermally unstable and quickly turns into a convective motion of progressively higher intensity as the depth of the melt layer increases. This simple realization of convective melting originated by a basal heating allows to analyse in a clear way the dependence between the properties of the global flow observables, such as the total heat-flux and the total kinetic energy, as a function of the depth of the melted fluid layer. It also reveals the possible links between the flow and phase-change interface which are shaped by it.

The structure of this chapter is as follows. In section 5.2, we present a model system together with its evolution equations. A discussion about the global heat-flux budget in the system with additional dimensional arguments for the heat-flux scaling behaviour in different flow regimes, is presented in section 5.3. The discussion section, Sect. 5.4, concisely presents the numerical simulation, which are implemented via the LB method presented in chapter 4.

The results of simulations in two- and three-dimensional systems are presented and discussed according to the following plan. Initially, we qualitatively describe the dynamics of system in section 5.5. To interpret and rationalize the observed trends in the scaling of global quantities, such as Nusselt and Reynolds number, we specialize the discussion on the dimensional effect 5.6 and 5.7 and by analyzing the morphology of melting front, in section 5.8. Moreover, in section 5.9, the effect of the Stefan control parameter on the rate of melting is studied, and observations on the effect of the aspect-ratio on the system dynamics are added in section 5.10. Finally, we conclude our analysis underlining possible implications and developments of the present study in section 5.11.



5.2. The horizontal convective melting system

The model system considered in this study consists of a solid layer of a pure substance of thickness H_{max} initially at a constant temperature, T_m , equal to the phase-change (melting) temperature. At time $t \geq 0$ the bottom boundary of the solid is heated at a constant temperature $T_0 > T_m$ and a melted fluid layer begins to grow from below.

The density of the fluid is assumed to be a decreasing function of temperature, therefore the bottom heating produces an unstable stratification of the fluid layer.

A cartoon of the model system is shown in Fig. 5.1, the coordinate frame is fixed at the bottom boundary, and the position of the solid/liquid interface is moving in the positive vertical z -direction.

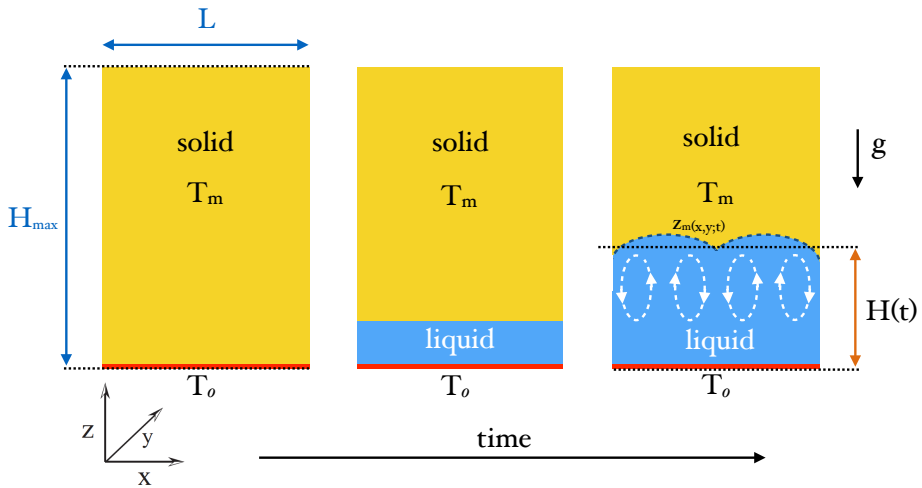


Figure 5.1 – Schematic diagram of the melting system. The system is filled with a pure solid at the temperature of melting (T_m). The temperature at the bottom (T_0) is higher than the melting temperature, consequently the solid turns into liquid for $t > 0$. Due to the thermal expansion coefficient of the liquid, a convection flow may develop in the fluid layer. The local height of interface is denoted with z_m , in general it is a function of spatial coordinates x, y and of time t .

The spatially averaged height is denoted by $H(t)$.

We recall that our model system is dynamically equivalent to the setting mentioned earlier of an Arctic melt pond, although it is an upside-down representation of it. Indeed, in melt ponds, heating occurs at the top rather than at the bottom but warmer water parcels are negatively (instead of positively) buoyant. For thorough information the reader is advised to refer to Chapter 3.

5.2.1. Equations of motion for the convective melting system

We recall the equations for the system of melting that we have derived in chapter 3. Under the assumption that the temperature differences occurring in the system are small such as the Boussinesq approximation holds, the governing equations in the melt layer, are then given by:

$$\rho_0 (\partial_t \mathbf{u} + (\mathbf{u} \cdot \nabla) \mathbf{u}) = -\nabla p + \mu \nabla^2 \mathbf{u} + \rho_L \mathbf{g}, \quad (5.1)$$

$$\nabla \cdot \mathbf{u} = \mathbf{0}, \quad (5.2)$$

$$\rho_L = \rho_0 (1 - \beta(T - T_0)), \quad (5.3)$$

$$\partial_t T + (\mathbf{u} \cdot \nabla) T = \kappa \nabla^2 T, \quad (5.4)$$

where $\mathbf{u}(\mathbf{x}, t)$, $p(\mathbf{x}, t)$ and $T(\mathbf{x}, t)$ denote respectively the fluid velocity, pressure and temperature fields. μ is the dynamic viscosity, ρ_0 the reference density at the temperature T_0 , \mathbf{g} the gravitational acceleration vector, and κ the thermal diffusivity. Note that the density is assumed to depend linearly on the temperature, the volumetric thermal expansion coefficient is $\beta > 0$. Furthermore, the incompressibility of the flow is specified, as a consequence of the Boussinesq approximation.

The boundary conditions associated to the above set of equations are: (i) fixed temperature at the bottom wall together with no-slip condition for velocity, (ii) periodic boundary condition at lateral boundaries, and finally (iii) no slip and melting conditions at the phase-change interface [1]. All together this reads:

$$T|_{\mathbf{x}=(x,y,0)} = T_0 \quad \forall x, y \in [0, L][0, L] \quad (5.5)$$

$$\mathbf{u}|_{\mathbf{x}=(x,y,0)} = \mathbf{0} \quad \forall x, y \in [0, L][0, L] \quad (5.6)$$

$$-\kappa \nabla T|_{\mathbf{x}=\mathbf{x}_m(t)} = \frac{\mathcal{L}}{c_p} \dot{\mathbf{x}}_m(t) \quad \forall \mathbf{x}_m(t) \in \mathcal{I}(t) \quad (5.7)$$

$$\mathbf{u}|_{\mathbf{x}=\mathbf{x}_m(t)} = \mathbf{0} \quad \forall \mathbf{x}_m(t) \in \mathcal{I}(t) \quad (5.8)$$

where \mathcal{L} , c_p are latent heat and specific heat respectively. $\mathbf{x}_m(t)$ are Lagrangian coordinates of points on the fluid-solid interface, denoted $\mathcal{I}(t)$, at time t , and $\dot{\mathbf{x}}_m(t)$ is therefore the velocity of the interface.

The energy conservation equation (5.4) together with the associated phase-change boundary conditions (5.5),(5.7) presented in the previous section, can be reformulated in terms of a single equation for the temperature and a phase field variable, ϕ_l [2]. This reads:

$$\partial_t T + (\mathbf{u} \cdot \nabla) T = \kappa \nabla^2 T - \frac{\mathcal{L}}{c_p} \partial_t \phi_l. \quad (5.9)$$

Here $\phi_l(\mathbf{x}, t)$ represents the volume fraction of the liquid phase, a quantity whose value is null in the solid and one in the fluid. Such a formulation can be derived from the transport equation for the enthalpy field $\mathcal{H}(\mathbf{x}(t); t) = c_p T + \phi_l \mathcal{L}$, which is the sum of the sensible heat and the latent heat associated to the phase-change process [3].

Finally, we note that the local height of liquid melt layer in a specific x, y position can be obtained from the liquid-fraction field as:

$$z_m(x, y, t) = \int_0^{H_{max}} \phi_l(\mathbf{x}, t) dz. \quad (5.10)$$

Similar to the procedure in chapter (3), it is convenient to express the equation of motion of the system in dimensionless form.

By adimensionalizing temperature by the temperature gap $\Delta T = T_0 - T_m > 0$, the density by ρ_0 , the length by H_{max} and finally the time by the diffusive time H_{max}^2/κ , the system of equations becomes:

$$\frac{\partial \tilde{\mathbf{u}}}{\partial \tilde{t}} + (\tilde{\mathbf{u}} \cdot \nabla) \tilde{\mathbf{u}} = -\nabla \tilde{p} + Pr \nabla^2 \tilde{\mathbf{u}} + Ra_{max} Pr \tilde{T} \hat{\mathbf{z}}, \quad (5.11)$$

$$\nabla \cdot \tilde{\mathbf{u}} = 0, \quad (5.12)$$

$$\frac{\partial \tilde{T}}{\partial \tilde{t}} + (\tilde{\mathbf{u}} \cdot \nabla) \tilde{T} = \nabla^2 \tilde{T} - \frac{1}{St} \frac{\partial \phi_l}{\partial \tilde{t}}, \quad (5.13)$$

with the tilded (\sim) quantities denoting here the dimensionless variables.

The obtained set of equations contains three dimensionless groups that can be identified as the three global control parameters:

- i) First, the Prandtl number, defined as the ratio of momentum diffusion (kinematic viscosity $\nu = \mu/\rho_0$) to thermal diffusion:

$$Pr = \frac{\nu}{\kappa}. \quad (5.14)$$

- ii) Second, the Rayleigh number, which is associated with the strength of natural convection in buoyancy-driven flow, and is defined as,

$$Ra_{max} = \frac{\beta \rho_0 g \Delta T H_{max}^3}{\mu \kappa}, \quad (5.15)$$

- iii) and finally the Stefan number, which is the ratio of sensible heat to latent heat,

$$St = \frac{c_p \Delta T}{\mathcal{L}}. \quad (5.16)$$

In the present study we are interested to investigate the dynamics of the system before the melting interface reaches the top boundary of the solid. This, combined to the fact that the initial solid temperature is the melting temperature, tells that the scale H_{max} is not a characteristic scale of the problem. In fact H_{max} plays no role in the dynamics, given the fact that there is no thermal diffusion in the solid phase. For this reason it is more convenient to adopt as a reference scale the instantaneous average height of the melting layer, $H(t)$, which is defined as

$$H(t) = \frac{1}{L^2} \int_0^L \int_0^L z_m(x, y, t) dx dy, \quad (5.17)$$

and it can also be expressed as

$$H(t) = \frac{1}{L^2} \int_V \phi_l d^3x = H_{max} \langle \phi_l \rangle, \quad (5.18)$$

where the notation $\langle \dots \rangle = V^{-1} \int_V \dots d^3x$ indicates a spatial volume average over the entire domain (*i.e.* fluid and solid). The term $\langle \phi_l \rangle$ denotes the global liquid fraction in the system. This allows to introduce the effective Rayleigh number:

$$Ra_{eff} = \frac{\beta \rho_0 g \Delta T H(t)^3}{\mu \kappa} = Ra_{max} \langle \phi_l \rangle^3. \quad (5.19)$$

A further control parameter characterizing the system is the geometrical aspect ratio. Also in this case it makes sense to define an effective aspect ratio,

$$\Gamma_{eff} = \frac{L}{H(t)} = \frac{L}{H_{max}} \frac{1}{\langle \phi_l \rangle} = \frac{\Gamma_{min}}{\langle \phi_l \rangle} \quad (5.20)$$

Note that the convective melting system during its dynamics always explore a range of effective aspect ratios, beginning at $\Gamma_{eff} = +\infty$ and reaching at most $\Gamma_{eff} = \Gamma_{min} = L/H_{max}$.

5.3. Heat-flux

In this section we derive the global relations expressing the vertical heat-flux across the fluid layer. We shall distinguish between the heat-flux across the system from below, we will call it incoming flux, since the heating is from the bottom, and the heat-flux at the fluid-solid interface, that we will call outgoing flux.

5.3.1. Global heat-flux balance

We begin by considering the equation for the temperature in the fluid domain with the moving interface formulation of eqs. (5.4). In conservative form (5.4) reads:

$$\partial_t T + \nabla \cdot (\mathbf{u}T - \kappa \nabla T) = 0. \quad (5.21)$$

We take the volume integral over the fluid domain and apply the divergence theorem

$$\int_{V_l} \partial_t T dx^3 + \int_{\partial V_l} \mathbf{n} \cdot (\mathbf{u}T - \kappa \nabla T) dS = 0. \quad (5.22)$$

By taking into account the velocity and temperature (5.7) boundary conditions:

$$\int_{V_l} \partial_t T dx^3 + \int_0^L \int_0^L \kappa \partial_z T|_{z=0} dx dy + \int_{\mathcal{G}} -\kappa \mathbf{n} \cdot \nabla T|_{x=x_m(t)} dS = 0. \quad (5.23)$$

By normalizing by the horizontal bottom surface (L^2) and rearranging the terms we get:

$$L^{-2} \int_0^L \int_0^L -\kappa \partial_z T|_{z=0} dx dy = L^{-2} \int_{\mathcal{G}} -\kappa \mathbf{n} \cdot \nabla T|_{x=x_m(t)} dS + L^{-2} \int_{V_l} \partial_t T dx^3. \quad (5.24)$$

The left-hand-side term in this equation can be identified with the bottom (incoming) heat flux in the fluid domain normalized by ρc_p , denoted by $Q^{in} = -\kappa \langle \partial_z T|_{z=0} \rangle_A$, where $\langle \dots \rangle_A$ stands for an average over a horizontal plane. The second term is the heat-flux normalized by ρc_p at the upper side of the fluid domain (outgoing), denoted by Q^{out} .

The last term is the total time variation of the temperature in the melt, it represents the global heating of the system, it is the term that results from the non-stationarity of the system dynamics. In the RB system this term can be neglected when a time average is also performed. In short:

$$Q^{in} = Q^{out} + L^{-2} \int_{V_l} \partial_t T dx^3. \quad (5.25)$$

The equation of heat flux (5.25) can be recast in terms of the dimensionless Nusselt number, through normalizing by $\kappa\Delta T/H_{max}$. This gives

$$Nu^{in} = Nu^{out} + \frac{H_{max}}{\kappa\Delta T} \frac{1}{L^2} \int_{V_l} \partial_t T dx^3. \quad (5.26)$$

Similarly to before it seems convenient to introduce here an effective Nusselt number:

$$Nu_{eff} = Nu \frac{H(t)}{H_{max}} = Nu \langle \phi_l \rangle. \quad (5.27)$$

The meaning of Nusselt effective Nu_{eff}^{in} is the usual one: the ratio between the total heat flux and the flux that would be transferred across the scale $H(t)$ with a temperature gap ΔT in a stationary process controlled only by the diffusivity κ . We note that this way of normalising the heat-flux has been first introduced in [4].

In dimensionless units (5.26) leads to:

$$Nu_{eff}^{in} = Nu_{eff}^{out} + \langle \phi_l \rangle^2 \langle \partial_{\tilde{t}} \tilde{T} \rangle_{V_l}, \quad (5.28)$$

where the average over liquid volume has also been introduced

$$\langle \dots \rangle_{V_l} = \frac{1}{V_l} \int_{V_l} \dots dx^3.$$

In order to better appreciate the meaning of the term Nu_{eff}^{out} in our system, we consider the conservation equation for the temperature in the full liquid-solid domain:

$$\partial_t T + \nabla \cdot (\mathbf{u}T - \kappa \nabla T) = -\frac{\mathcal{L}}{c_p} \partial_t \phi_l. \quad (5.29)$$

We perform a volume integral over the whole domain and proceed through the same steps as before. This leads to

$$Nu_{eff}^{in} = \frac{1}{St} \frac{H_{max}^2}{\kappa} \langle \phi_l \rangle \frac{d\langle \phi_l \rangle}{dt} + \frac{H(t)}{\kappa\Delta T} \frac{1}{L^2} \int_V \partial_t T dx^3, \quad (5.30)$$

and in dimensionless units:

$$Nu_{eff}^{in} = \frac{1}{St} \langle \phi_l \rangle \frac{d\langle \phi_l \rangle}{d\tilde{t}} + \frac{\langle \phi_l \rangle}{V} \int_V \partial_{\tilde{t}} \tilde{T} dx^3. \quad (5.31)$$

We now observe that

$$\langle \dots \rangle = \frac{1}{V} \int_V \dots dx^3 = \langle \phi_l \rangle \langle \dots \rangle_{V_l} + (1 - \langle \phi_l \rangle) \langle \dots \rangle_{V_s},$$

and applying this to $\partial_{\tilde{t}} \tilde{T}$ one obtains

$$Nu_{eff}^{in} = \frac{1}{2St} \frac{d\langle \phi_l \rangle^2}{d\tilde{t}} + \langle \phi_l \rangle^2 \langle \partial_{\tilde{t}} \tilde{T} \rangle_{V_l} + (\langle \phi_l \rangle - \langle \phi_l \rangle^2) \langle \partial_{\tilde{t}} \tilde{T} \rangle_{V_s}. \quad (5.32)$$



In the special case in which the solid is initially uniformly at the melting temperature T_m , no conduction occurs in the solid phase and hence $\langle \partial_{\tilde{t}} \tilde{T} \rangle_{V_s} = 0$, one is allowed to directly link the outgoing heat flux with the melting fraction variation over time.

In summary, in the system when the solid is initially at melting temperature we have:

$$Nu_{eff}^{in} = -\langle \partial_{\tilde{z}} \tilde{T} |_{z=0} \rangle_A \langle \phi_l \rangle \quad (5.33)$$

$$Nu_{eff}^{out} = \frac{1}{2St} \frac{d \langle \phi_l \rangle^2}{d\tilde{t}} \quad (5.34)$$

$$Nu_{eff}^{in} - Nu_{eff}^{out} = \langle \phi_l \rangle^2 \langle \partial_{\tilde{t}} \tilde{T} \rangle_{V_l} > 0 \quad (5.35)$$

The last inequality follows from the fact that one expects that not all the heat-flux will flow through the cell, but that a part of it will be used to warm up the liquid to a temperature in between the minimum value T_m and the maximum T_0 .

5.3.2. Scaling relations for the heat flux and melting rate

Before the onset of convection, i.e. for time small enough, the system evolution is governed by heat conduction in the fluid layer and melting at its boundary with the solid. In such conditions, the liquid-solid interface is flat; the incoming and outgoing heat fluxes are respectively given by

$$Nu_{eff}^{in} = \frac{2\lambda^2}{St} e^{\lambda^2} \quad \text{and} \quad Nu_{eff}^{out} = \frac{2\lambda^2}{St}. \quad (5.36)$$

We observe that both *in* and *out* Nusselt numbers are time independent and they differ by a constant factor that is also St number dependent. In the limit of small St , by Taylor expanding (3.29) one can show that $\lambda \simeq \sqrt{St/2}$, therefore simply $Nu_{eff}^{out} \simeq 1$ and $Nu_{eff}^{in} \simeq 1 + St/2$.

In the convective regime, due to the important non-linearities characterizing the system dynamics, the exact expression for the dependence of the global liquid fraction as a function of time, $\langle \phi_l(t) \rangle$, is not available. However, the relations between the Nusselt number and the global fluid fraction, that we have derived in the previous sections, can be used to extract at least some dimensional scaling relations.

Similarly to what is done for turbulent convection in the RB system, one can assume that the effective Nusselt number is a power-law function of the system control parameters. We will consider here the outgoing effective Nusselt number:

$$Nu_{eff}^{out} \sim Ra^\alpha Pr^\delta St^\gamma. \quad (5.37)$$

By using (5.34) and (5.19) and assuming that a scaling relation of the form $\langle \phi_l \rangle \sim \tilde{t}^{\alpha'} Pr^{\delta'} St^{\gamma'}$ also holds, one gets the corresponding scaling for the global melt fraction:

$$\langle \phi_l \rangle \sim \tilde{t}^{\frac{1}{2-3\alpha}} Pr^{\frac{\delta}{2-3\alpha}} St^{\frac{\gamma+1}{2-3\alpha}}. \quad (5.38)$$

Few observations are in order:

- In the conductive case, because Nu_{eff}^{out} is constant one has $\alpha = \delta = \gamma = 0$, Eq. (5.38) gives the already known behaviour $\langle \phi_l \rangle \sim \tilde{t}^{1/2} St^{1/2}$ (where the limit of small St has been taken too).

- In the convective situation, by analogy with the RB system the value $\alpha = 1/3$ may be considered. We remind that in the RB context the $1/3$ Rayleigh exponent corresponds to the so called Malkus scaling [5], a regime where the horizontal thermal boundary-layers are marginally stable or in other words the dimensional vertical heat-flux does not depend on the height of the system [6]. In the CM context the same effective Rayleigh scaling exponent corresponds to a constant average melting front speed $v_m = \frac{d}{dt} \langle \phi_l \rangle = \text{const.}$
- The so called ultimate regime of thermal convection, which is dominated by the flow dynamics in the bulk of the system, and is characterised by $\alpha = 1/2$ and $\delta = 1/2$ would give for the front speed: $v_m \sim Pr \tilde{\tau}$, that is to say a constant acceleration.

Finally we shall note that, we are not aware of systematic studies about the effect of the Stefan number on the global heat-flux in the convective regime. However, we can observe that an independence of Nu_{eff}^{out} from St ($\gamma = 0$) and at the same time $\alpha = 1/3$ would imply a linear dependence of the melting front speed with it, $v_m \sim St$.

5

5.4. Discussion

Because the focus is on water-ice dynamics (melt ponds in the Arctic), we always consider in this study $Pr = 10$, which is close to the one of fresh water just above the freezing point (for water at temperature $0.01^\circ\text{C} < T < 10^\circ\text{C}$, Prandtl is at $9.47 < Pr < 13.67$) [7]. Ulvrova and colleagues [4] addressed the same problem, however for $Pr = 7$, $St = 0.9$ and at $Pr = \infty$, $St = 10$, the former value is suitable for water at 20°C while the latter is a useful approximation for convection in rocks and in the solidified Earth mantle.

The value of Stefan number used in the mentioned study is $St = O(1)$, a value that is advantageous for numerical computations but that is not always realistic for geophysical applications. For exemple the estimated St number appropriate for ice-melt pond is $O(10^{-2})$, for Basal Earth Magma ocean an upper estimate based on temperature differences of 10^3K gives $St = O(1 - 10)$ [4], magmatic chambers and lava lakes are close or less with respect to the latter value. In the present work, for the computational reasons, we perform the majority of simulations at $St = 1$, but we will also present results of computationally more expensive simulations at $St = 10^{-1}$ or faster ones at $St = 10, 100$.

The simulations are initialized by setting the fluid-fraction $\phi_l = 0$ in the whole domain and at the same time the temperature at the melting value $T = T_m$. A small random perturbation ($T_e = 10^{-6}$) is superimposed to trigger the destabilization of the system. The hydrodynamical instability exhibited by the system is of linear type [8] similar to the one in the RB system.

Ensemble average is performed over several simulations to cancel the effect of random noise. In table 5.1 we summarize the most relevant information on all the convective melting simulations performed. We list both the numerical parameters adopted in the LB simulations and the resulting dimensionless control parameters. To guide the reader we also provide an indication on where the obtained data are employed in the figures of the paper.

As far as RB simulations are concerned, the simulations are performed with same or very similar numerical parameters as the melting ones. The Rayleigh number is set by controlling the height of the system (L_z) and we make sure to have always at least 8

5.5. Qualitative description of system dynamics

grid points in the thermal boundary layer. Simulations ran over tenth or hundreds of large-eddy turnover times.

In this context, the turnover time is defined as $T_e = L_x / \overline{u_{rms}}$ with L_x the width of the system and $u_{rms} = \sqrt{\langle \sum_i u_i^2 \rangle_V}$ where the average is taken not only over the volume, $\langle \dots \rangle_V$, but also over time, $\overline{\dots}$.

Note that in the system with melting the appropriate definition of u_{rms} is different from the RB system: First it is inherently time-dependent and hence it should be based only on a spatial average. Second, because the undeformable solid has by definition null velocity it makes more sense to compute such an average on the fluid domain only. This means that:

$$u_{rms, V_l} = \sqrt{\langle \sum_i u_i^2 \rangle_{V_l}} = \sqrt{\langle \sum_i u_i^2 \rangle_V} \langle \phi_l \rangle^{-1/2} = u_{rms} \langle \phi_l \rangle^{-1/2}. \quad (5.39)$$

Such an amplitude will be used for the construction of the global Reynolds number, which will be discussed later on.

	N	L_x	L_z	L_y	ν	κ	β	ΔT	g	\mathcal{L}	c_p	Pr	St	Ra_{max}	Γ_{min}	Fig. n.
2D	8	2000	1000	1	0.2	0.02	0.0005	1	1	1	100	10	100	$1.25 \cdot 10^8$	2	5.14
	8	2000	1000	1	0.2	0.02	0.0005	1	1	1	10	10	10	$1.25 \cdot 10^8$	2	5.11, 5.13, 5.14
	8	2000	1000	1	0.2	0.02	0.0005	1	1	1	1	10	1	$1.25 \cdot 10^8$	2	5.2, 5.3, 5.4, 5.5, 5.7, 5.9, 5.11, 5.13, 5.14
	8	2000	1000	1	0.2	0.02	0.0005	1	1	10	1	10	0.1	$1.25 \cdot 10^8$	2	5.11, 5.13, 5.14
	6	256	1000	1	0.2	0.02	0.0005	1	1	1	1	10	1	$1.25 \cdot 10^8$	0.256	5.15, 5.16a, 5.16b
3D	6	512	512	512	0.2	0.02	0.003	1	1	1	1	10	1	$1.00 \cdot 10^8$	1	5.5, 5.7, 5.8, 5.9, 5.11, 5.14

Table 5.1 – Summary of the parameters values for all convective melting simulations. We provide dimensional and dimensionless control parameters. The dimensional parameters are in numerical units. The second column from left (N) specifies the number of simulations performed, which are employed to estimate the ensemble averages. The last column (Fig. n.) specifies in which figure of the paper the results of the simulations are displayed.

5.5. Qualitative description of system dynamics

We begin by describing the typical evolution of the convective melting model system. Such an evolution passes through different stages.

In the very early stages the melt is produced solely by conduction through an increasing fluid layer and the system closely follow the Stefan solution. There is no noticeable fluid flow in the system and the phase-change interface remains flat all the time.

Due to an initial small numerical perturbation seeded in the temperature field of the full domain, an hydrodynamic instability develops into a convective flow pattern. The nature of such an instability is linear and has been analytically studied in [8], where it was shown that the onset of convection is delayed for increasing values of St number, and the effective critical Rayleigh number of the RB system is recovered only in the vanishing St limit. The convective onset in the system occurs at around $Ra_{eff} \approx 5 \cdot 10^3$ in our 2D simulations.

The flow visualization shown in Fig. 5.2 helps in elucidating the main features of the convective melting dynamics, from the early onset stage on, in a two-dimensional setting.

The onset of convection is marked by a change in the shape of the phase-change interface from flat to a nearly periodic array of semicircular convex arcs, see Fig. 5.2 (a) at $Ra_{eff} = 5 \cdot 10^4$. In this phase the convective rolls grow vertically as if they were stretched along this direction. This stage resembles the steady convection observed immediately after the convection onset in the RB system, in the present case however steadiness of the flow is intrinsically not possible due to the increase over time of the system height.

At $Ra_{eff} = 2.5 \cdot 10^5$, Fig. 5.2 (b), the rolls begin to display lateral oscillations. When oscillations are strong enough convective rolls can merge in pairs. This has a repercussion on the interface shape, which is subsequently shaped by the new flow patterns. This happens however with some time delay.

Indeed at $Ra_{eff} = 2.9 \cdot 10^5$, Fig. 5.2 (c), we see that all the rolls have merged, creating convection cells of doubled or tripled width, while the interface shape is not yet strongly affected. At $Ra_{eff} = 5 \cdot 10^5$, Fig. 5.2(d), the interface has finally lost its previous periodicity and has become smoother, without cusps (*i.e.* discontinuities in the first derivative).

At $Ra_{eff} = 5 \cdot 10^6$, Fig. 5.2 (e), larger convective flow patterns have been established, they have a lateral size approximately doubled with respect to the ones at the lower Ra decade. The interface has now again cusps and it is evident that such special points pin the detachment of cold plumes.

One decade after, at $Ra_{eff} = 5 \cdot 10^7$, the cells are bigger and the flow is manifestly organised in large rolls which strongly fluctuate in time and space, Fig. 5.2 (f).

5.6. Scaling in the 2D system

In order to address quantitatively the system dynamics; we study the intensity of global heat flux Nu_{eff}^{in} as a function of the forcing imposed to the system, which is here parametrised by Ra_{eff} .

The rationale for the choice of the incoming heat-flux instead of the outgoing, is that it makes easier the comparison with the RB system, where the heat flux can be computed exactly in the same way, eq. (5.33). Furthermore, for numerical reasons, the computations of Nu_{eff}^{in} in the convective melting simulations is less affected by spurious numerical noise. We will come back on the discussion of the differences between Nu_{eff}^{in} and Nu_{eff}^{out} at the end of this chapter (section 5.9).

Figure 5.3 shows Nu_{eff}^{in} both for two-dimensional convective melting (CM) and for 2D RB system. We can observe that, apart from the convective onset, that arises at much

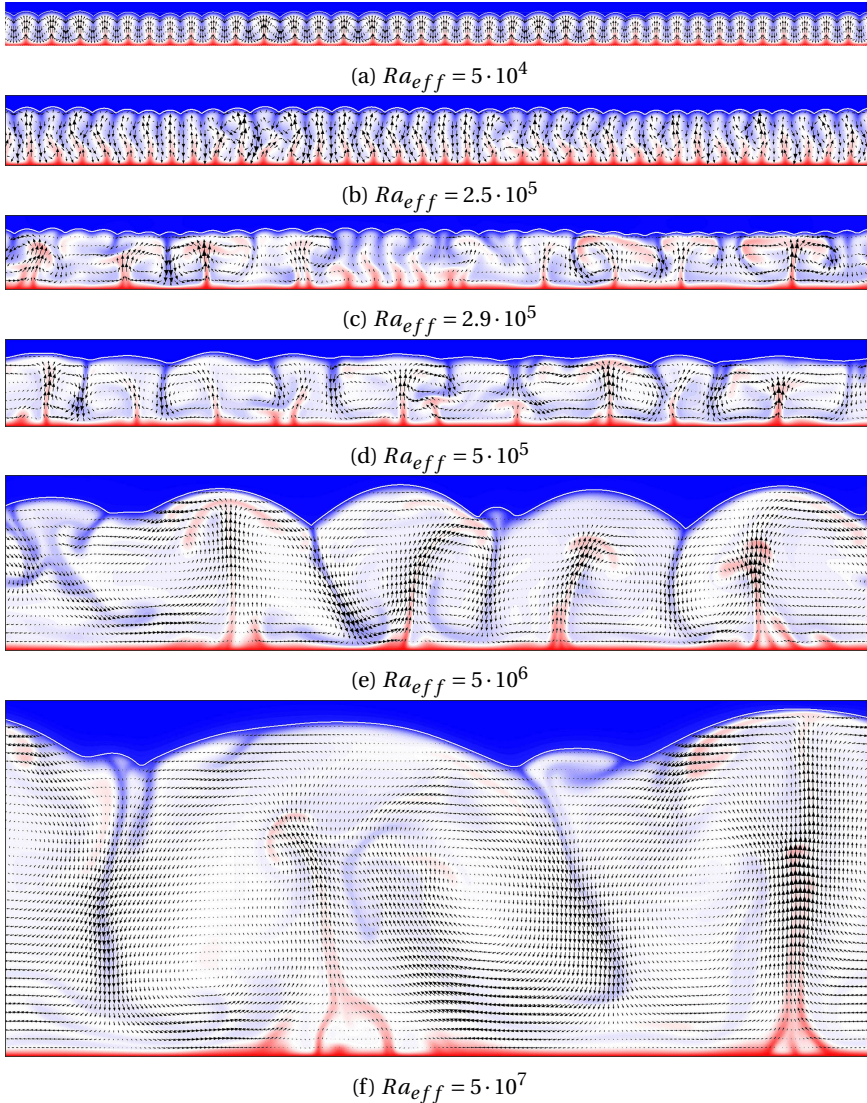


Figure 5.2 – Visualization of the 2D CM system in different stages at increasing effective Rayleigh numbers. The colors represent the temperature field (red $T_{bot} = -0.5$, blue $T_{top} = T_m = 0.5$ and white zero degree), and arrows are the velocity field normalized by the magnitude of the maximum velocity in each field separately. The white line on the top of each visualization is the solid-liquid interface. The global parameters of the system are $St = 1$ and $Pr = 10$. [movie of this simulation is available on request]

lower number in the RB system ($Ra \approx 1708$ as compared to $Ra_{eff} \approx 5 \times 10^3$), the global incoming heat flux trend is very similar for the two systems and the actual value of Nu tends to be indistinguishable as Ra_{eff} is increased.

The same figure reports the numerical results by Ulvrova *et al.* [4], which despite the different conditions (different $Pr = 7$, non-periodic lateral boundary conditions, initial temperature of the solid lower than the melting temperature T_m) they also fall close to our results. Likewise to the RB system, this similarity of results in different conditions attests for the robustness of the $Nu-Ra$ relation also in the CM system.

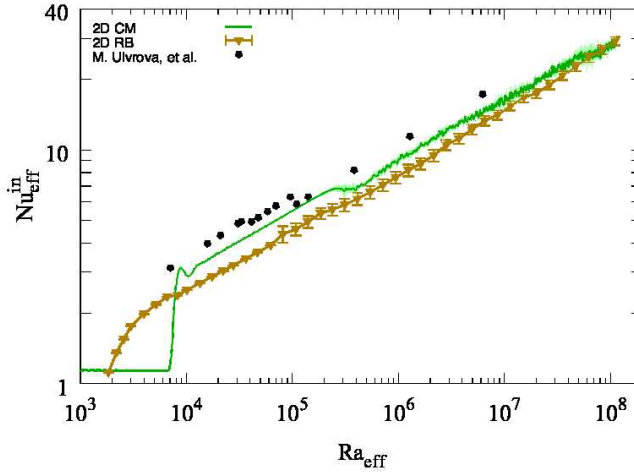


Figure 5.3 – Plot of the incoming dimensionless heat-flux Nu_{eff}^{in} with respect to the Rayleigh number computed using the average height of interface, Ra_{eff} . Results are shown both for the convective melting setup and for the Rayleigh-Bénard system. The minimum aspect ratio for the simulations is $\Gamma_{min} = 2$, *i.e.*, the system is always much larger than deeper. The other control parameters of the melting systems are $St = 1$ and $Pr = 10$. The RB system has also $Pr = 10$ and always the same Γ_{eff} of the corresponding melting system. In addition, we show the result of numerical computation of Ulvrova *et al.* [4] in a laterally bounded box, for $Pr = 7$ and $St = 1$ (circles).

To complement this picture we also look at the scaling of the global kinetic energy of the system. In dimensionless form, this is cast in terms of an effective Reynolds number:

$$Re_{eff} = \frac{u_{rms,V_l} H(t)}{\nu} = \frac{u_{rms} \langle \phi \rangle^{1/2} H_{max}}{\nu}, \quad (5.40)$$

where u_{rms,V_l} is the root-mean-square velocity in the fluid part of the system (5.39) and u_{rms} denotes instead the one over the total solid-and-liquid system volume.

We observe here (Fig. 5.4) that the agreement of the CM behaviour with the RB one is remarkable, particularly in the range $Ra_{eff} \geq 4 \cdot 10^5$. At lower Ra_{eff} the appearing differences in Re_{eff} are due to the delayed transitions occurring in the CM with respect to the RB system. For instance the transition from horizontally steady to lateral oscillating patterns occurs at around $Ra \approx 6 \cdot 10^4$ in the RB system and it is observed at $Ra_{eff} \approx 3 \cdot 10^5$ in the CM system.

A possible explanation for the fact that the magnitude and scaling of global quantities in the RB and CM systems are so close, can be provided on the basis of a com-

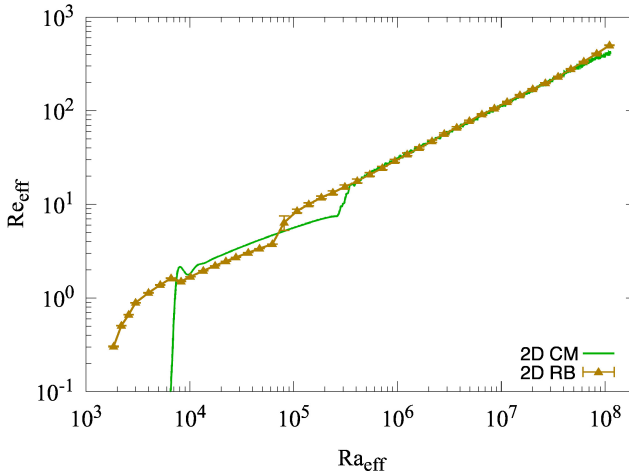


Figure 5.4 – Plot of the effective Reynolds as defined in Eq. (5.40) with respect to the effective Rayleigh number, and comparison with the Rayleigh-Bénard system with the same control parameters $St = 1$ and $Pr = 10$.

5

parison among two characteristic velocity scales in the system. The first scale is the typical flow intensity u_{rms,V_l} , while the second is the mean vertical melt front velocity, $v_m = dH(t)/dt$. It makes sense to conjecture that the CM system will behave as the RB if the melt front moves slowly with respect to the flow intensity, $v_m \ll u_{rms,V_l}$. This relation can be recast in dimensionless form, via (5.34) and (5.40):

$$Nu_{eff}^{out} \ll \frac{Pr Re_{eff}}{St}. \quad (5.41)$$

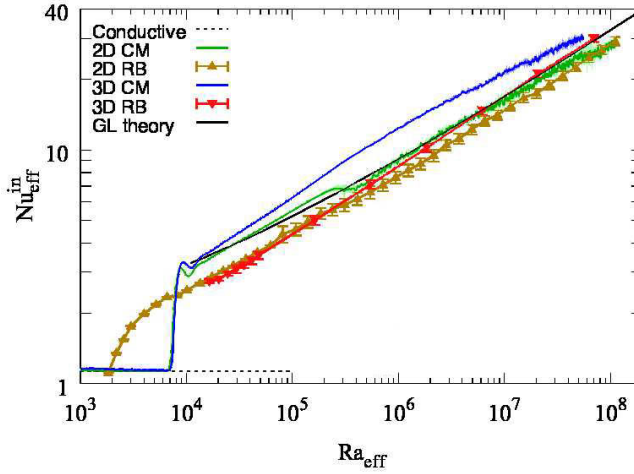
We know from (5.35) that Nu_{eff}^{in} is always larger than Nu_{eff}^{out} . Therefore if the above condition is satisfied for the *in* Nusselt number it will be satisfied also for the *out* one. Because here $Pr/St = 10$, it is easily checked that the criterion is fulfilled at all stages, *i.e.* all Ra_{eff} values, of the CM evolution.

5.7. Scaling in the 3D system

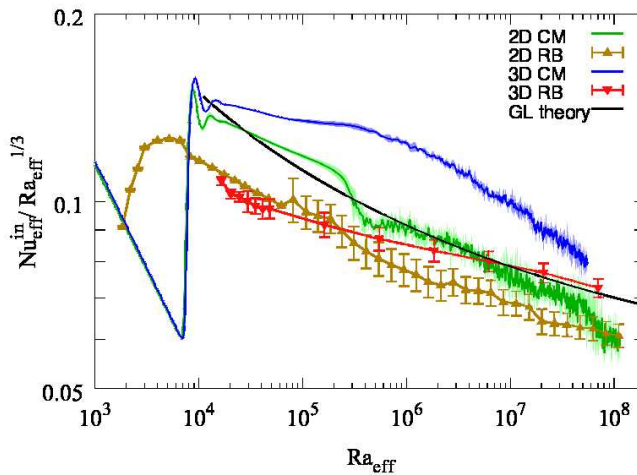
The differences in the functional behaviour of global observables, such as heat-flux or kinetic energy, between the 2D and 3D flows have been investigated at depth for the RB system.

Recently, van der Poel, *et al.*[9] have numerically compared the dynamics of lateral bounded 2D and 3D RB systems. In this study, which reached up to $Ra = 10^8$ with $0.045 \leq Pr \leq 55$ and $\Gamma = 1$, these authors have numerically demonstrated that the dimensionless global heat-flux of the 2D system follows the same scaling laws with respect to Ra as the 3D system, however they differ by an approximately constant multiplicative factor, *i.e.*,

$Nu_{2D} \approx K \cdot Nu_{3D}$ with $K < 1$). The aim of this section is to assess to what extent this observation also holds for the CM system.



(a)



(b)

Figure 5.5 – (a) Inlet effective Nusselt number with respect to the effective Rayleigh number computed according to average height of interface for 2D and 3D systems with the same configuration for the melting system. The $Nu(Ra)$ data for the Rayleigh-Bénard system are also shown. The global parameters of the melting systems are $St = 1$ and $Pr = 10$. The solid black line is the Grossmann-Lohse (GL) theory prediction, calculated as from [10, 11]. (b) same as above but in a compensated plot with respect to $Ra_{eff}^{1/3}$.

As a preliminary numerical test, we perform 2D and 3D RB simulations and check the $Nu - Ra$ dependence for laterally periodic system. We also check the agreement with the Grossmann-Lohse (GL) theory [10–12], which is known to capture the Ra and Pr dependence of Nu and Re over a wide parameter range. Although GL theory is based on the assumption that the system is three-dimensional, laterally bounded by no-slip and adiabatic walls, the agreement with our laterally periodic 3D simulations appears satisfactory and within the statistical accuracy of the numerics (see Fig. 5.5a). Note that in all cases the Nusselt scaling exponent with Ra is always below the $1/3$ value: This is better appreciated in the compensated graph Fig. 5.5b.

Similarly to the previously mentioned 2D-3D comparative study [9] we observe that the two-dimensional RB system is less efficient in transporting heat than the 3D. The highest relative difference among the 3D and 2D Nusselt numbers is of the order of 30% and it occurs at around $Ra_{eff} \sim 3 \cdot 10^5$ (see Fig. 5.6). However, given the limited Ra -range covered, it is presently not possible to make statements on the variation of the scaling exponents with the Rayleigh number (see Fig. 5.5b).

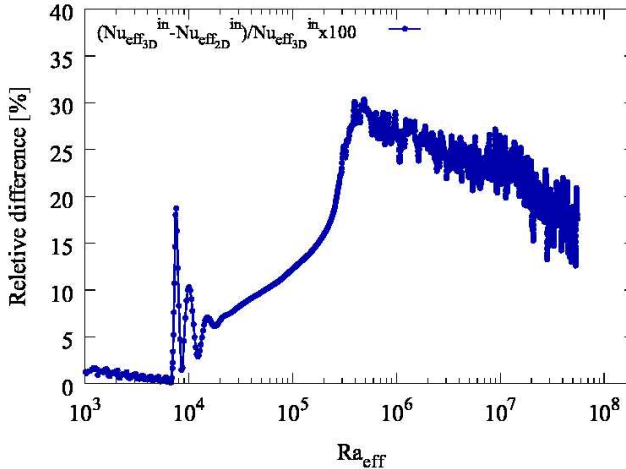


Figure 5.6 – Relative difference in % between the effective Nusselt numbers measured in 3D and 2D simulations at $St = 1$ and $Pr = 10$ and as a function of the effective Rayleigh number.

We now look at the CM system. A equivalent 2D-3D hierarchy is also displayed in this case. The 3D effective Nusselt number is always above the 2D at corresponding Ra_{eff} values. In amplitude the difference appears to be higher than in the corresponding RB situation. Secondly, what seems to be the most remarkable feature is that in the limit of large Rayleigh numbers, the CM systems (either in 2D or 3D) tend to have the same global heat-flux amplitude as the RB system. However, such a feature can be soundly confirmed only by performing simulations at higher Rayleigh numbers (Ra_{eff} and $Ra > 10^8$) than the ones described in the presented study.

We conclude by noting that the Reynolds number, Fig. 5.7, of 3D CM simulations are in nearly perfect agreement both with the 3D RB simulations and with the GL theory.

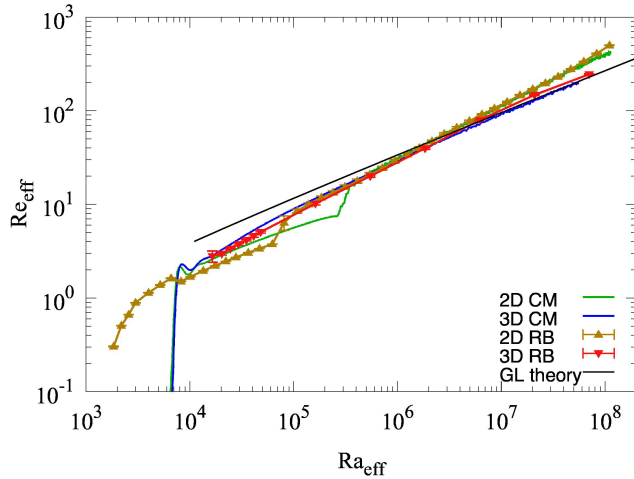


Figure 5.7 – Reynolds number (kinetic energy of the system based on equation 5.40) versus Rayleigh, computed according to average height of interface for 2D and 3D systems with the same configuration, both for melting system and Rayleigh-Bénard. The global parameters of the melting systems are $St = 1$ and $Pr = 10$. The solid black line is the GL prediction [11].

We observe that Re_{eff} in 3D system does not show abrupt amplitude changes, associated to pattern transitions, as noticed in the 2D case. Differently from the Nu number amplitude we observed here that at high- Ra_{eff} the Reynolds number $Re_{2D} > Re_{3D}$. Also this feature, qualitatively agrees with the previous observation in the 2D-3D bounded RB system [9].

In summary, we have shown that the 3D CM system in the range of parameters studied here ($Pr = 10$, $St = 1$) behaves very similarly to a RB system. The trend when increasing its dimensionality from 2D to 3D also closely follows the one of the RB. While the Reynolds number among the two system is nearly identical, the Nusselt number displays a distinctive behaviour, characterized by $Nu_{CM} > Nu_{RB}$ for $Ra_{eff} \in [\sim 10^4, \sim 10^7]$. However, at higher-Ra such a difference seems to reduce and eventually vanish.

5.8. Morphology of the phase-change interface

In this section we aim at a quantitative characterization of the shape of the phase-change interface. The focus is on the trends as a function of the Rayleigh number at fixed Stefan number and at the possible differences connected to the system dimensionality. With this in mind, we deliberately consider simple quantifiers of the boundary roughness that can be applied to both the 2D and 3D systems.

We begin by describing a visualization through contour lines of the phase-change surface in a 3D setup, Fig. 5.8, and contrasting it from a qualitative view point with the 2D case. Even though the convection onset in 2D and 3D systems occurs at the same Ra_{eff} value (see again Fig. 5.5 or Fig. 5.7) we can see from Fig. 5.8a that already at

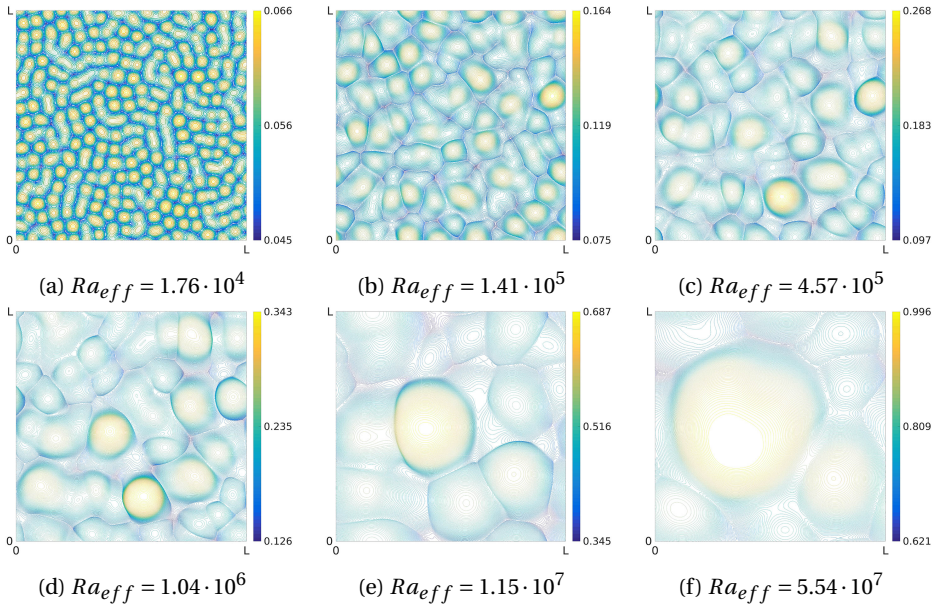


Figure 5.8 – Visualization with isolines contours of the phase-change interface from 3D simulations at different Rayleigh number. Panel (a) corresponds to the stage close to the convective onset where horizontally steady convection patterns are observed. The shape of these convective cells appears to be approximately hexagonal, one can note that few cells have already merged creating elongated patterns. The merging process develops further at higher Rayleigh numbers (panels b-e). Finally, panel (f) is at aspect ratio $\Gamma_{eff} = 1$, where one specific pattern has become dominant. [movie of this simulation is available on request]

$Ra_{eff} = 1.76 \cdot 10^4$ the 3D system displays cellular like (rather than roll like) convection patterns.

This highlights the effect of dimensionality on the dynamics of the system. Indeed the convective melting 3D system displays transiently polygonal patterns that are brought to merge into larger convective cells of similar polygonal shape 5.8c. This merging process continues till the formation of a big cell, limited only by the lateral system size.

Polygonal patterns of the phase-change interface have been already observed in convective melting experiments. Davis *et al.* [13] performed experiments on a horizontal layer of cyclohexane heated from below and cooled from top. These authors observed three different corrugation patterns of the interface, denoted as roll-like, mixed polygonal-roll and hexagonal patterns, (see Fig. 3 of [13]). The criteria for the emergence of different patterns in Davis work was associated to the ratio of the solid to liquid depth layer; a criteria that can not be used in the present model. Sugawara, et al. [14] performed similar experiments on a layer of ice melted from below. In this case, cellular polygonal patterns, called shark-skin, were observed at the solid-liquid interface, (see Fig. 9 of their work). Irregular hexagonal patterns were also reported in the experiments with melting wax by Hill [15] (these results are also described in [16]).

Despite the different conditions (among others different values for Pr and St , and initial solid temperature different from the melting temperature) our numerical results appear to be in qualitative agreement with the above mentioned experimental results.

We have observed that, both in 2D and in 3D, the shape of the phase-change interface at a given time seems to be characterised by well defined length-scales: a horizontal wavelength corresponding to the later size of convective patterns and a typical roughness due to the vertical modulation of the interface.

To quantify the first of these scales, that we call L_c , we make use of the one dimensional auto-correlation function of the local interface height $z_m(x, t)$ in 2D or $z_m(x, y, t)$ in 3D. It reads:

$$C(r, t) = \langle z_m(x+r, t) z_m(x, t) \rangle_A \quad (2D) \quad (5.42)$$

$$C_x(r, t) = \langle z_m(x+r, y, t) z_m(x, y, t) \rangle_A \quad (3D) \quad (5.43)$$

$$C_y(r, t) = \langle z_m(x, y+r, t) z_m(x, y, t) \rangle_A \quad (3D) \quad (5.44)$$

Note that the area mean, $\langle \dots \rangle_A$, denotes an average over x -direction in 2D and over xy -plane in the 3D system along respectively x and y horizontal directions, and since the model system is not confined laterally (periodic boundaries) these functions can be conveniently computed through the Fourier transform.

Let's first observe that, in the hypothetical case of a sinusoidally modulated interface shape, the position of the first minimum of the correlation function identifies the half wavelength of the interface modulation. By analogy we define here such a position as $L_c/2$ and we identify such a longitudinal correlation length, L_c , as the average width of the convective cells in the CM system.

The computed L_c , normalized by $H(t)$, as a function of the Ra_{eff} number is shown in figure 5.9a. As we already know, at small Ra_{eff} , the system dynamics is purely conductive and as a result the interface is flat; and in such a case L_c is not defined. Later on, the onset of convection produce a finite L_c as it drives the formation of recirculating patterns (cells) with an aspect ratio ~ 1.5 . The ratio $L_c/H(t)$ then decreases because the number of convective rolls remain constant while the height of the melt increases. Such a reversed saw-tooth behaviour is more evident for the, more constrained, 2D system than for the 3D cases.

Asymptotically there is a tendency towards the formation of rolls of typical aspect ratio 1 and this appears to be independent of the dimensionality of the system. The latter one is a feature also present in (flat-wall) RB systems [9].

The average roughness of the liquid-solid interface can be quantified by means of the standard deviation of the fluid-solid boundary height, z_m , which reads:

$$\sigma_{z_m}(t) = \sqrt{\langle (z_m(t) - H(t))^2 \rangle_A} \quad (5.45)$$

where the average, $\langle \dots \rangle_A$, is the same as before.

The evolution of the normalized fluctuation $\sigma_{z_m}(t)/H(t)$ with respect to Ra_{eff} is shown in Fig. 5.9c. First we measure an average roughness amplitude of about 5 to 15 percent of the melt height. We can remark that the 3D system is characterised by larger roughness, up to three times, as compared to the 2D. The saw tooth profile is clearly

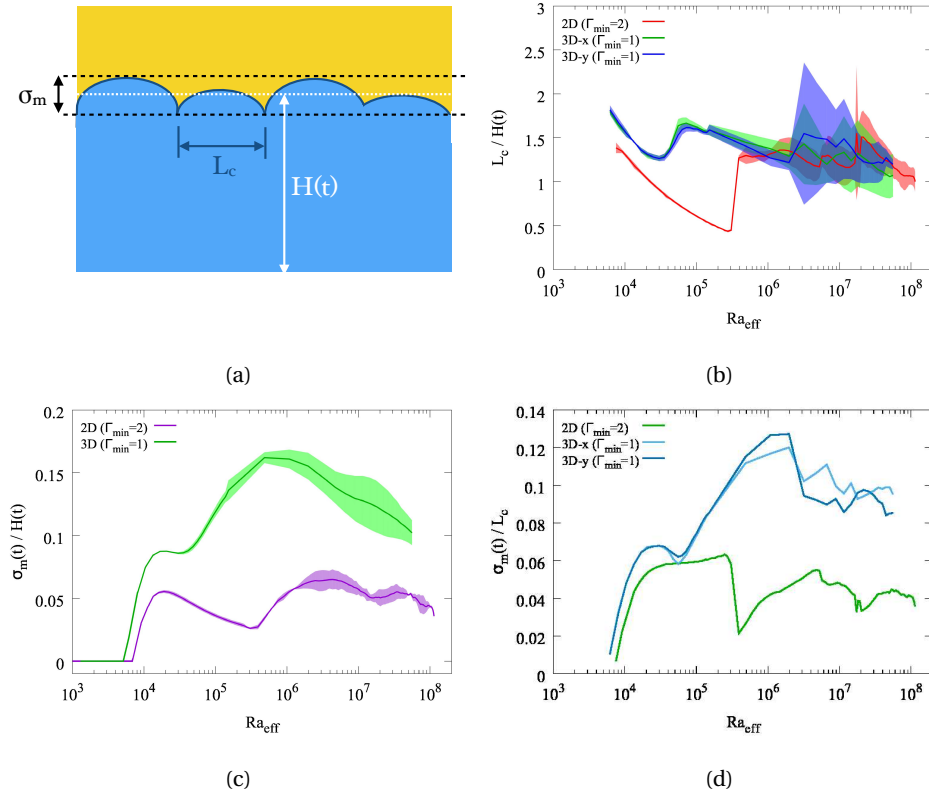


Figure 5.9 – (a) Schematic view of the melt layer with relevant interface length scales: horizontal correlation length $L_c(t)$, roughness $\sigma_m(t)$, mean height $H(t)$. (b) Correlation length versus Ra_{eff} . In all different cases $L_c(t)$ is at most slightly larger than one half of the domain width L (at the end of the simulations). (c) Roughness versus Ra_{eff} . (d) Ratio of the roughness to the correlation length, σ_m/L_c . In panels (b-d), the curves are obtained from ensemble averages; the shaded areas in (b) and (c) account for the spreading of the measured values over different realizations, computed as the difference between the maximum and minimum values. The large spreading at large Ra_{eff} in panel (b) is due to limited statistics.

noticeable in the 2D system. However the 3D system behaviour get closer to the 2D at the highest Rayleigh numbers explored.

The roughness of the interface has been studied by Davies [13] and more recently by Hill [15] and by Ulvrova [16]. In the latter work roughness has been defined as the difference between the maximum and the minimum value of the interface.

In Fig. 5.9d we also show the evolution of the ratio of the roughness over horizontal correlation length of the interface, $\sigma_{z_m}/L_c(t)$. We observe that such a ratio is relatively stable over the last three Ra_{eff} decades of the simulation, and in 3D is approximately double as compared to the 2D system.

It has been long known that tiny variation in the bounding geometry of a convective

tive cell can affect the thermal and kinetic boundary layers and as consequence produce variations on the intensity of the mean heat-flux [17, 18]. The matter has been addressed first experimentally, by introducing in the RB system controlled walls roughness either on one or both horizontal plates. Different types of corrugated walls have been employed and in the majority of the cases this has lead to an increase of the Nusselt number, confirmed also by numerics [19] (see [6] for a recent review covering the role of roughness).

More recently, [20] and [21] have systematically investigated the effect of a top-wall sinusoidal bounding geometry (of given depth but variable wave-length). An optimal wavelength, which was about 1/7 of the cell height, was found to maximally enhance the intensity and the Ra -scaling of the total heat flux. In this study the amplitude of the sinusoidal roughness was kept fixed to 1/10 of the maximum cell height. Given these finding, it is plausible to guess that the shape of the upper bounding geometry in the convective system have a role in the perceived difference on the heat-flux among the 2D and 3D system.

5.9. Effect of Stefan number

This section focuses on the effect of the Stefan number both on global and morphological quantities. We remind that the Stefan number parametrizes the ratio of the substance heat capacity over the latent heat. A high value of Stefan corresponds to a material for which melting is energetically inexpensive while the opposite is true for St smaller than a unit value. Rather counterintuitively the stability analysis [8] as well as our simulations shows that the convective instability arises later for higher St numbers. However the larger is St , the higher is the average speed of the melting front v_m .

Before analyzing the dependency of heat flux on the Stefan number, we qualitatively observe St dependency of the melting system. Figure (5.10) shows the advancement of solid-liquid interface for four Stefan numbers of $St = 0.01, 0.1, 1$ and 10 . Independent of magnitude of the Stefan number, all the systems go through three stages of conduction, transition and convection. The transition (onset of convection) is highly dependent to St in a way that for smaller Stefan number the onset of convection delays in time.

In the convection regime, however, two stages can be distinguished. The first stage is where the convection plays regular behaviour, and number of rolls appears in the liquid layer. However, this regularity fades away as the interface progress in time (which we addressed previously by Ra number). In the second stage of convection, the behaviour of flow is rather irregular, which means rolls start to merge and create bigger rolls.

The convective dynamics can again be conveniently examined in term of the function $Nu_{eff}^{in}(Ra_{eff}, St)$. In figure 5.11 (a) we show that at increasing St there is a small but detectable increase of the inlet effective heat flux for equal values of the Rayleigh number. Such a difference is better quantified by inspecting the ratio between $Nu_{eff}^{in}(Ra_{eff}, St)$ and $Nu_{eff}^{in}(Ra_{eff}, St = 1)$ which we take here as a reference. We see in Fig. 5.11 (b) that the convective regime shows always a reduced excursion as compared to the conductive one, although they are of the same order of magnitude. We have also attempted to perform a power-law fit of the form $Nu_{eff}^{in}(Ra_{eff}, St) = Nu_{eff}^{in}(Ra_{eff}, St = 1) \cdot A St^B$ with A, B fitting parameters. This leads to A close to 1 within percent and to a scaling exponents of roughly 0.05.

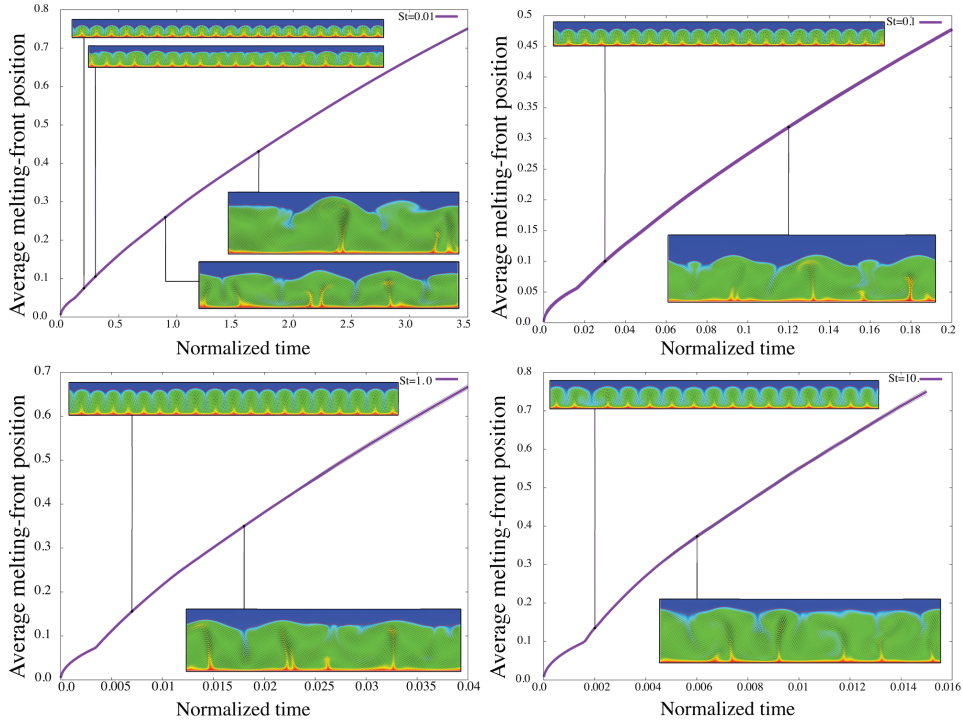


Figure 5.10 – The average height of melting front for $St = 0.01, 0.1, 1$ and 10 together with visualization velocity and temperature field at different stage in time. The interface is normalized by total height of the system (H_{max}) and the time with convective time scale (H_{max}^2/κ)

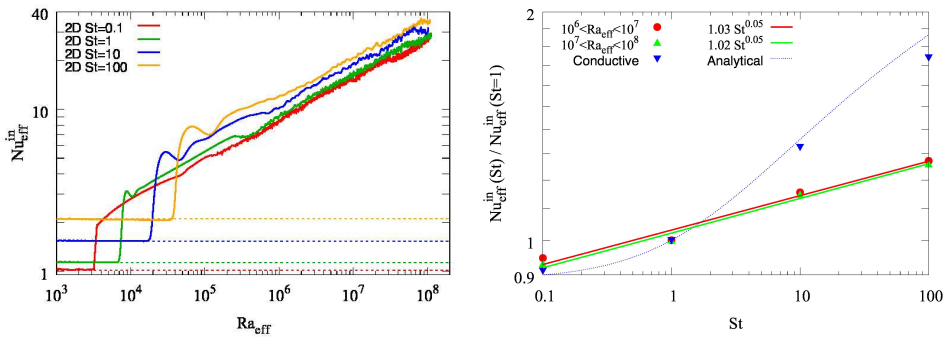


Figure 5.11 – (a) Inlet Nusselt number as a function of the effective Rayleigh at $St = 0.1, 1, 10$ and 100 for 2D CM systems. The horizontal dotted lines give the corresponding conductive value (5.36). (b) Ratio of Nu_{in} for $St = 0.1, 1, 10$ and 100 over Nu_{in} at $St = 1$. Comparison of the conductive trend with the trend detected in the convective regime in the intervals $Ra_{eff} \in [10^6, 10^7]$ and $Ra_{eff} \in [10^7, 10^8]$ and estimate of their power-law dependencies.

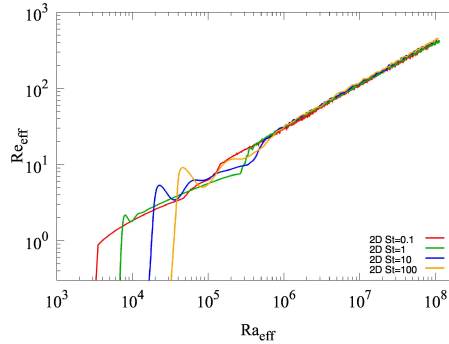


Figure 5.12 – Reynolds number (kinetic energy of the system) as a function of the effective Rayleigh at $St = 0.1, 1, 10$ and 100 for 2D CM systems.

5

We note that the observations provided so far are derived by 2D simulations but we can confirm that the same picture holds in 3D settings, where we have performed a comparison at $St = 0.1, 1, 10$ (not shown here).

In term of the kinetic energy of the system, we observe that apart from the onset of convection, the behaviour of the melting systems for different St is almost identical (see Fig. 5.12)

We now inspect the global features of melting interfaces. The averaged longitudinal correlation length as well as the fluctuation $\sigma(z_m)$ confirm that the St effect is weak. In figure 5.13, while differences in the low- Ra regime are present, all becomes within the estimated uncertainty range for high- Ra . Asymptotically with Ra , in 2D simulations, the cell patterns seem to approach from above a unit aspect ratio with a roughness that is as low as 4% of the height of the melt. It is of interest to look also at the behaviour of $\sigma(z_m)/L_c$, because this quantity share some similarity with the ratio of roughness amplitude over roughness-wavelength (h/λ) which has been used to investigate the effect of non-flat boundaries on the RB convection [20].

In a recent numerical study it has been observed that the heat-flux enhancement induced by wall-roughness reaches a maximum when $h/\lambda \simeq 1$, while such an effect monotonically decreases for larger or smaller values of the same ratio [20, 21]. Such an observation seems to apply also to the present case, see figure 5.14a, where the ratio $\sigma(z_m)/L_c$ which is always small, decreases further at increasing Ra_{eff} . We shall therefore expect that any heat-enhancement effect with respect to the RB system will decrease as the Rayleigh number is increased (or in other words as time progresses).

Finally we address the question of the inequality between the heat-fluxes Nu_{eff}^{in} and Nu_{eff}^{out} , that we mentioned earlier in this chapter. Such a mismatch is connected to the time instationarity of the CM system and it is therefore present even when the average of Nu over different system realisations (ensemble average) is performed. On the contrary the RB system is statistically stationary in time and such a difference, although instantaneously present, is zero on average (in time or in ensemble sense). In the CM system a fraction of the incoming heat flow is used to raise the global temperature of the cold

5.9. Effect of Stefan number

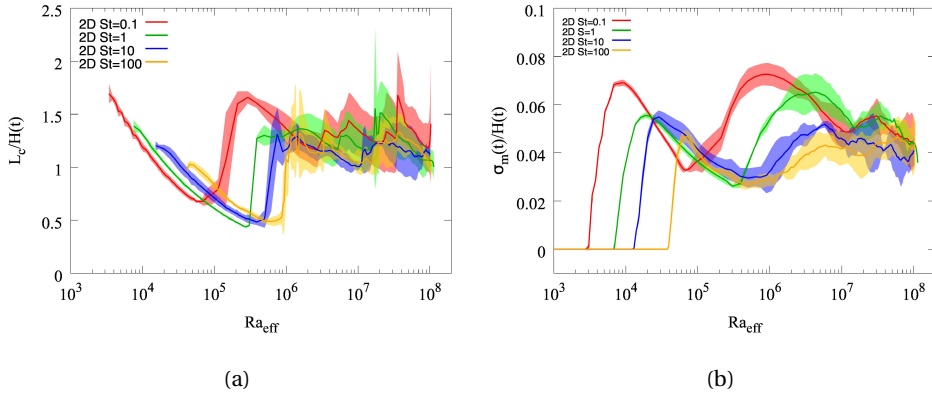


Figure 5.13 – (a) Horizontal correlation length of fluid-solid interface L_c normalized by the average height of melt layer $H(t)$ versus the effective Rayleigh number for simulations at different Stefan numbers and minimal aspect ratios. (b) Same as before but for the standard deviation of z_m .

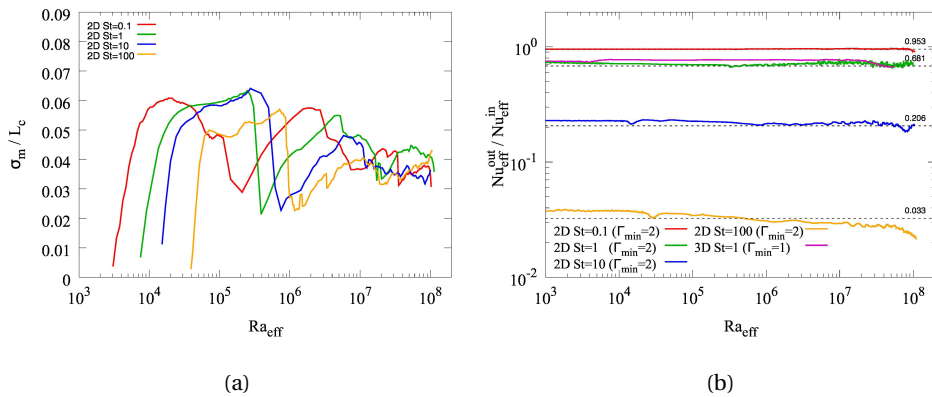


Figure 5.14 – (a) Ratio of the standard deviation of melting interface over the horizontal correlation length at increasing Ra_{eff} for the same St number values. (b) Ratio between outgoing and incoming heat flux in the system with respect to Rayleigh for 2D systems for $St = 1, 0.1$ and 0.01 . The dashed lines give the corresponding value in conductive (no flow) conditions $e^{-\lambda^2}$.

fluid released from the melting process.

Intuitively one can expect that the Nusselt fraction $Nu_{eff}^{out}/Nu_{eff}^{in}$ will be small in systems where the melt process is rapid, because most of the heat will be needed to warm up the fluid. Note that such a mismatch already exists in the conductive regime of melting, where it can be computed analytically and has the value $Nu_{eff}^{out}/Nu_{eff}^{in} = e^{-\lambda^2}$.

The fraction of transmitted heat $Nu_{eff}^{out}/Nu_{eff}^{in}$ as a function of Ra_{eff} range is shown in Fig. 5.14b, where we traced both results from 2D and 3D simulations at different Stefan

numbers. First, we notice that as expected such a ratio is decreasing at increasing St . Furthermore, the values result to be always close to the corresponding conductive ones. This implies that the warm up of the liquid is here driven by a diffusional process, rather than by a convective one, even in the high- Ra regime. A feature that we presume to be connected to the value of the Prandtl number, $Pr \gg 1$ and hence to the fact that the thermal boundary layer is thinner than the kinetic one. The possibility of linking the behaviour of Nu_{eff}^{in} and Nu_{eff}^{out} has implications for the extrapolation of our results; even on St regimes which we did not explore numerically. For instance the St number of interest for water-ice phase-change in arctic ponds are $\sim 10^{-2}$, a condition where the incoming and outgoing heat flux can be considered as essentially equal in magnitude.

5.10. Effect of aspect ratio

Apart from Stefan, Rayleigh and Prandtl numbers that control the dynamic of melting system directly through influence in governing equations, there is one more control parameter that does not affect the equations, however, it is defined by the size of the domain of simulation. The ratio of the height of the system to its width is known as aspect ratio, which is defined by Eq. (5.20).

In this section we consider two identical systems except with different widths. The summary of parameters used for comparing two systems with different aspect ratio is in table (5.1).

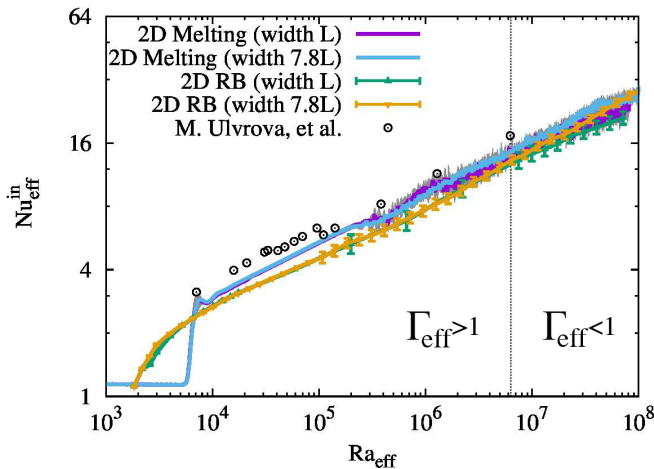


Figure 5.15 – Plot of inlet heat flux versus Rayleigh number for two identical melting systems with different widths. Relative to each melting system, corresponding RB is also computed and included in this figure. The dotted line corresponds to the point in time where aspect ratio of the system is unity.

Similar to previous sections, the first comparison would be the incoming heat flux and the effect of aspect ratio on the heat budget. Fig. 5.15 shows the inlet heat flux as a

5.11. Conclusion

form of the Nusselt number, for two melting systems with different widths. In addition, for comparing reason, Fig. 5.15 contains relative RB system to each melting system. For both CM systems, the initial aspect ratio is very large (the height of the liquid layer is zero initially), however for the system with smaller width, it reaches one at some point, which is indicated by vertical dotted line.

The comparison does not show significant changes in heat coming into the system with respect to aspect ratio. However, as the melting system approaches aspect ratio of unity, the velocity fields will be constrained laterally. In order to see the effect of aspect ratio on velocity field, we can look in the total kinetic energy of the two systems (Fig. 5.16a). As it can be seen the two systems behave similarly, except where the aspect ratio of the system with smaller width becomes smaller than one (dotted line).

In order to see the effect of aspect ratio on the components of velocity, one can consider the ratio of average vertical velocity to horizontal one, which is shown in Fig. 5.16b. Clearly, the two systems behave differently for aspect ratio smaller than one. As one can see, the magnitudes of horizontal and vertical velocities have same order as long as the aspect ratio is larger than one. However, when the aspect ratio is less than unity, the horizontal velocity becomes more dominant. Therefore, more heat is transferred laterally, due to greater horizontal velocity.

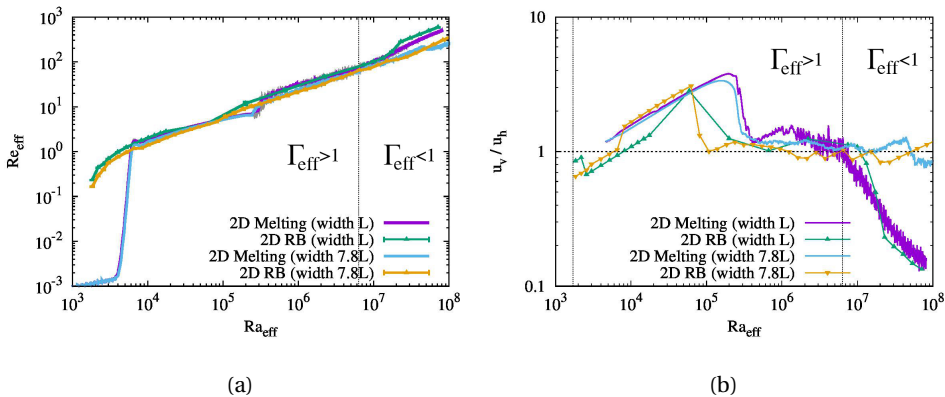


Figure 5.16 – (a) Plot of Reynolds number versus changes in Rayleigh effective for two identical 2D melting system with different widths. (b) Plot of relative vertical velocity to horizontal one for melting systems with different aspect ratio.

5.11. Conclusion

In this chapter the dynamics of the melting process of a horizontally heated pure substance under the effect of conduction and natural convection has been numerically studied. The analysis has focused on the scaling of extensive quantities, global heat flux and global kinetic energy, at varying the control parameters in the system and on the effects linked to its dimensionality. We have exploited the knowledge of the paradigmatic Rayleigh-Bénard system in order to have a better insight on the observed model system and to draw possible similarities.

It has been shown that CM and RB have close behaviour in terms of the $Nu(Ra)$ and the $Re(Ra)$ functional dependencies. While both systems show almost identical trends for the Reynolds number, it was observed that Nu_{CM} is slightly higher than Nu_{RB} . However, such differences seem to vanish as convection intensity is increased, *i.e.*, for high values of the effective Rayleigh number (or equivalently asymptotically in time), indicating that in turbulent conditions the phenomenology of the RB system can give quantitatively good predictions for the CM system dynamics. Similarly to RB convection, the 2D CM system has a weaker global heat flux as compared to the 3D CM setting.

Visualizations of the melting front in 3D revealed the appearance of convective patterns with approximately hexagonal, and more often irregular polygonal, cross section. As Rayleigh increases, *i.e.* as the fluid layer grows, such cells undergo a coarsening process. Investigating the morphological properties of the liquid-solid interface with statistical indicators, we found that this is characterized by larger roughness in 3D than in 2D, which can account for the differences detected in the 3D and 2D heat flux behaviours. However, the roughness reaches at most 15% in 3D (respectively 5% in 2D) of the melt height and, independent of the space dimensionality, it further decreases at sufficiently high Rayleigh numbers. Such low values of the melting front roughness again point to strong similarities between the CM and the flat-wall RB systems.

The Stefan number dependency has been investigated in 2D for the range of values $0.1 \leq St \leq 100$. Although increasing St significantly delays the onset of convection, very small differences were observed in the dimensionless global heat flux in the high Rayleigh number regime. This finding is of potential interest for numerical studies, because it allows to extrapolate results of fast simulations at high- St values to conditions of small St values that would be otherwise unattainable in direct numerical simulations. Small values of the Stefan number correspond to slowly advancing melting fronts or quasi-adiabatic cases, which are closer to the RB configuration. We remark that the typical condition of ice melt ponds corresponds to a Stefan number ($St \sim O(10^{-2})$).

Finally, we addressed the question of the difference between the instantaneous global inflow and outflow in the system, which is connected to the mean temporal variation of the temperature of the fluid. We have shown that such a gap is essentially controlled by a diffusive process and that is more pronounced in systems where the melt process is faster, hence for larger values of the Stefan number.

The model system studied in this work represents a rudimentary approximation of a real melt pond. Among others, one major approximation is the fact to neglect the thermal forcing due to radiation heating, which correspond to a bulk temperature source term in the fluid. A second approximation concerns the presence of a wind drafts at the air-water interface that can greatly perturb and affect the instability and the evolution of convective patterns in the ponds. Such effects will be addressed in the next chapters.

References

- [1] V. Alexiades, *Mathematical modeling of melting and freezing processes* (CRC Press, 1992).
- [2] A. Faghri and Y. Zhang, *Transport Phenomena in Multiphase Systems* (Academic Press, Elsevier, 2006).



- [3] W. Shyy, H. Udaykumar, M. Rao, and R. Smith, *Computational Fluid Dynamics with Moving Boundaries*, Dover Books on Engineering (Dover Publications, 2012).
- [4] M. Ulvrová, S. Labrosse, N. Coltice, P. Råback, and P. Tackley, *Numerical modelling of convection interacting with a melting and solidification front: Application to the thermal evolution of the basal magma ocean*, *Physics of the Earth and Planetary Interiors* **206**, 51 (2012).
- [5] W. V. R. Malkus, *The heat transport and spectrum of thermal turbulence*, *Proc. Royal Soc. A* **225**, 1161 (1954).
- [6] F. Chillà and J. Schumacher, *New perspectives in turbulent Rayleigh-Bénard convection*, *The European Physical Journal E* **35**, 58 (2012).
- [7] E. D. Skyllingstad, C. A. Paulson, and D. K. Perovich, *Simulation of melt pond evolution on level ice*, *Journal of Geophysical Research: Oceans* **114**, (2009), c12019.
- [8] M. C. Kim, D. W. Lee, and C. K. Choi, *Onset of buoyancy-driven convection in melting from below*, *Korean Journal of Chemical Engineering* **25**, 1239 (2008).
- [9] E. P. van der Poel, R. J. A. M. Stevens, and D. Lohse, *Comparison between two- and three-dimensional Rayleigh-Bénard convection*, *Journal of Fluid Mechanics* **736**, 177–194 (2013).
- [10] S. Grossmann and D. Lohse, *Scaling in thermal convection: a unifying theory*, *Journal of Fluid Mechanics* **407**, 27 (2000).
- [11] R. J. A. M. Stevens, E. P. van der Poel, S. Grossmann, and D. Lohse, *The unifying theory of scaling in thermal convection: the updated prefactors*, *Journal of Fluid Mechanics* **730**, 295–308 (2013).
- [12] G. Ahlers, S. Grossmann, and D. Lohse, *Heat transfer and large scale dynamics in turbulent Rayleigh-Bénard convection*, *Reviews of modern physics* **81**, 503 (2009).
- [13] S. H. Davis, U. Müller, and C. Dietsche, *Pattern selection in single-component systems coupling Bénard convection and solidification*, *Journal of Fluid Mechanics* **144**, 133–151 (1984).
- [14] M. Sugawara, E. Tamura, Y. Satoh, Y. Komatsu, M. Tago, and H. Beer, *Visual observations of flow structure and melting front morphology in horizontal ice plate melting from above into a mixture*, *Heat and Mass Transfer* **43**, 1009 (2006).
- [15] X. Hill, *La convection sous un solide. Applications aux planètes*, Ph.D. thesis, Université Paris 7 (1996), thèse de doctorat, Institut de Physique du Globe de Paris.
- [16] M. Ulvrová, S. Labrosse, N. Coltice, T. Alboussière, C. Jaupart, C. Sotin, and C. Farnetani, *Dynamique des fluides et des transports appliquée à la Terre primitive*, Ph.D. thesis, Lyon, École normale supérieure (2012), thèse de doctorat Sciences de la Terre Lyon, École normale supérieure 2012.
- [17] Y. Shen, P. Tong, and K.-Q. Xia, *Turbulent convection over rough surfaces*, *Phys. Rev. Lett.* **76**, 908 (1996).
- [18] S. Ciliberto and C. Laroche, *Random roughness of boundary increases the turbulent convection scaling exponent*, *Phys. Rev. Lett.* **82**, 3998 (1999).
- [19] G. Stringano, G. Pascazio, and R. Verzicco, *Turbulent thermal convection over grooved plates*, *Journal of Fluid Mechanics* **557**, 307–336 (2006).
- [20] S. Toppaladoddi, S. Succi, and J. S. Wettlaufer, *Tailoring boundary geometry to optimize heat transport in turbulent convection*, *EPL (Europhysics Letters)* **111**, 44005 (2015).

- [21] X. Zhu, R. J. A. M. Stevens, R. Verzicco, and D. Lohse, *Roughness-facilitated local 1/2 scaling does not imply the onset of the ultimate regime of thermal convection*, Phys. Rev. Lett. **119**, 064501 (2017).
- [22] A. V. Getling, *Rayleigh-Bénard convection: structures and dynamics*, Vol. 11 (World Scientific, 1998).



6

Convective melting system with a moving boundary

In addition to having natural convection, the CM system can be subject to further constraints, *e.g.* having an external moving boundary, which can represent the existence of wind or stream in the pond. Regarding any CM problem, the first question one can ask is the predictability of the evolution of the melting-rate which is connected to the heat-flux dynamics determined by the flow in the system. The problem of CM due to natural convection has been addressed thoroughly in the previous chapter. In this chapter, we present the behaviour of CM system at turbulent, *i.e.* high Rayleigh number, natural convection coupled with an external moving boundary.

6.1. Convective melting system with a moving boundary

In order to study the effect of a moving boundary on the dynamics of the CM system, similar to our model in the Chapter 5, we consider a solid layer initially at a constant temperature T_m . We start to heat the system with a constant temperature $T_0 > T_m$ from the bottom and simultaneously a horizontal velocity V_x is applied on the bottom boundary. Consequently, while the solid starts to melt, the velocity field in the liquid layer take effects from the velocity on the bottom boundary. A schematic of the model system is shown in Fig. 6.1.

6.1.1. Equation of motion for the phase-change problem: moving boundary formulation

The governing equations for the system of melting coupled with a moving boundary are the same as pure CM system (Eq. (5.1-5.4)), except for the bottom boundary. For this model, the boundary conditions for the bottom wall are: (i) fixed temperature and (ii)



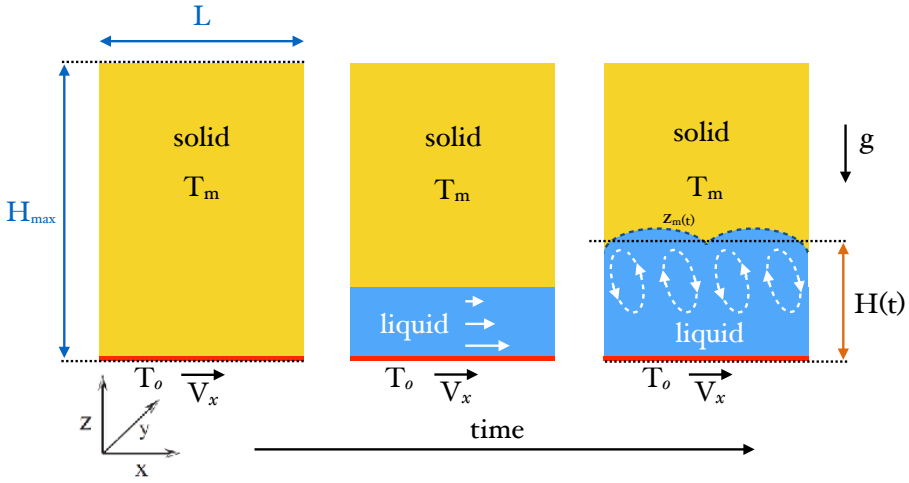


Figure 6.1 – Schematic diagram of the melting system. The system is the same as Fig.5.1, however in addition to the bottom (T_0), velocity V_x is applied on the bottom boundary.

6

imposed constant horizontal velocity V_x ,

$$T|_{\mathbf{x}=(x,y,0)} = T_0 \quad \forall x, y \in [0, L][0, L] \quad (6.1)$$

$$\mathbf{u}|_{\mathbf{x}=(x,y,0)} = (V_x, 0, 0) \quad \forall x, y \in [0, L][0, L] \quad (6.2)$$

$$(6.3)$$

The remaining boundary conditions are (i) periodic boundary condition at lateral boundaries, and (ii) no slip and melting conditions at the phase-change interface (Eq.(5.7) and (5.8)).

6.2. Discussion

In this section, we look at the result of numerical simulations computed by DNS code developed based on Lattice-Boltzmann method. For each simulation, all the parameters, except the shear velocity at the bottom boundary, are kept fixed. The values of parameters are summarized in Table (6.1). In order to reduce the effect of initial perturbation applied on each simulation, for each shear velocity, ensemble average over 6 simulations are employed.

In order to investigate the effect of the wall velocity, we perform several simulations with different velocities (V_x), which we present in dimensionless form

$$\tilde{V} = \sqrt{Fr}, \quad (6.4)$$

where Fr is Froude number, which is a ratio of inertial and gravitational forces, and is defined as

$$Fr = \frac{\rho V_x^2}{\Delta \rho g H_{max}} = \frac{V_x^2}{\beta \Delta T g H_{max}}. \quad (6.5)$$

number of runs	L_x	L_y	ν	κ	β	ΔT	g	\mathcal{L}	c_p	Pr	St	Ra_{max}
6	2000	1000	0.2	0.02	$5 \cdot 10^{-4}$	1	1	1	1	10	1	$1.25 \cdot 10^8$
6	2000	1000	0.2	0.02	$5 \cdot 10^{-4}$	1	1	10	1	10	0.1	$1.25 \cdot 10^8$

Table 6.1 – Summary of the parameters values for all convective melting simulations. We provide dimensional and dimensionless control parameters. The dimensional parameters are in numerical units.

The last equality is due to substituting density variation from $\rho = \rho_0(1 - \beta\Delta T)$.

Similar to pure melting system, apart from the wall velocity, we have three other dimensionless parameters that can be identified as the global control parameters; the Rayleigh number (Ra) (Eq.5.15), the Prandtl number (Pr) (Eq.5.14) and the Stefan number (St) (Eq.5.16).

By considering the global liquid fraction, similar to the case of melting, we can introduce the effective Rayleigh number (Eq. 5.19). As in chapter 5, in order to quantify the results, we look to heat budget in form of the dimensionless Nusselt number, which we measure at the bottom boundary (Eq. 5.33).

Before presenting the results in a quantitative fashion, the behaviour of the CM system with and without existence of shear velocity is addressed qualitatively. Comparing Fig. 6.2 (pure CM system) and Fig. 6.3 (CM system with a moving boundary), one can observe the decrease in the number of rolls in Fig. 6.3. Moreover, the shape of the rolls are more distorted in the direction of shear velocity. The second observation is the shape of the solid-liquid interface, which is much flatter in Fig. 6.3. We will address these observations quantitatively in the following sections.

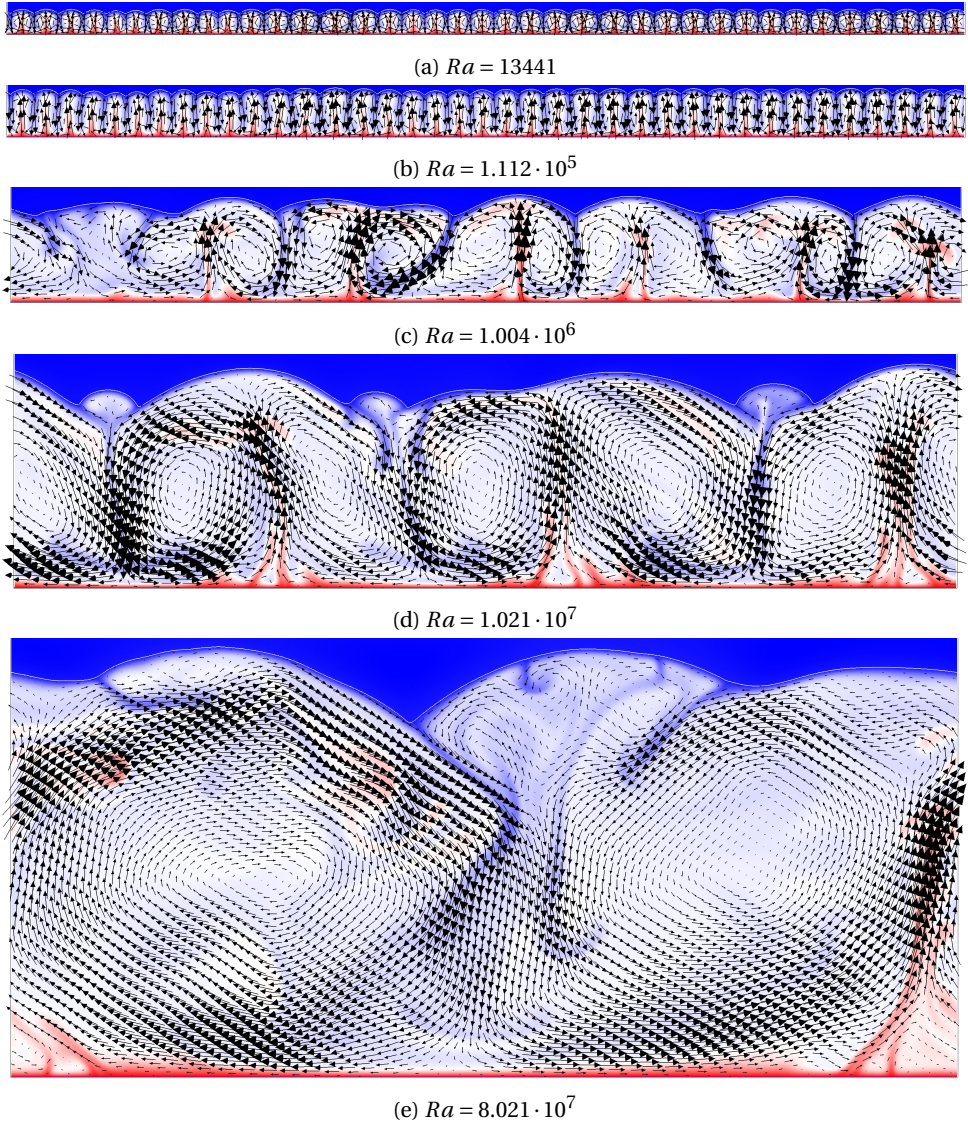
The results presented in this section are categorized into two different analyses. Firstly, the effect of the global control parameters on the dynamics of the system. And secondly, the characterization of interface roughness and morphology, and its coupling effects on flow in the liquid layer.

6.2.1. Results on global quantities

Before quantitatively address the dynamics of the CM system with a moving boundary, it is important to have a better perspective of the magnitude of wall velocity. The maximum wall velocity in our simulations is $\tilde{V} = \sqrt{2} \times 10^{-1}$, which corresponds to a very small wind velocity $3 \times 10^{-4} \text{m s}^{-1}$ on the surface of a melt-pond with depth 20cm. Such a small velocity was adopted in order to avoid numerical issues in the simulations. It is known that when the wind velocity is high enough, the buoyancy plays a marginal role and the system is dominated by wind effects.

Skyllingstad *et al.* [1] addressed the problem of melting coupled with moving boundary through applying constant wind stress of 0.01N m^{-2} which corresponds to wall velocity of 0.1m s^{-1} . However, they considered constant rate of melting in their model, instead of estimating rate of melting through the internal dynamics of the system. Reader is advised to refer to chapter 2 for further information.

In order to address quantitatively the system dynamics, we study the intensity of the



6

Figure 6.2 – Visualization of the 2D CM system in different stages at increasing effective Rayleigh numbers for the CM system without an external moving boundary ($\tilde{V} = 0$). The colors represent the temperature field (red $T_{bot} = -0.5$, blue $T_{top} = T_m = 0.5$ and white zero), and the arrows are the velocity field normalized by the magnitude of the maximum velocity in each field separately. The white line on the top of each visualization is the solid-liquid interface. The global parameters of the system are $St = 1$ and $Pr = 10$.

global heat flux Nu_{eff}^{in} (Eq. (5.27)) as a function of the forcing imposed to the system, which is here parameterized by Ra_{eff} (Eq. (5.19)). Similarly to the discussion in chapter

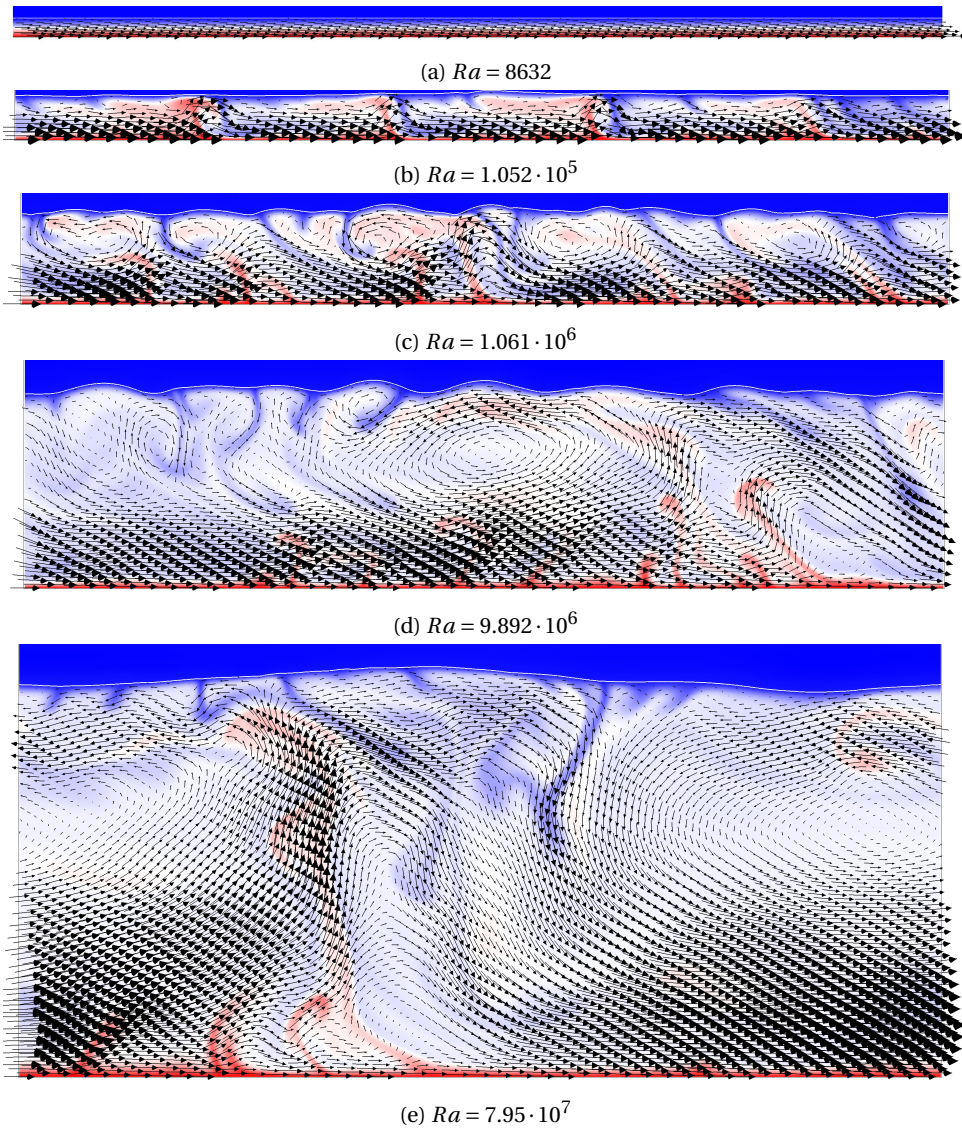


Figure 6.3 – The description of the figures is the same as Fig. 6.2, however, with an external moving boundary with fixed velocity $\tilde{V} = \sqrt{2} \times 10^{-1}$.

5, the choice of the incoming heat-flux instead of the outgoing, is for numerical reasons.

Figure 6.4 shows Nu_{eff}^{in} for two-dimensional convective melting (CM) with different shear velocities and for two Stefan numbers of $St = 0.1$ and $St = 1$. We can see that the onset of convection is dependent to the magnitude of shear velocity, and for higher \tilde{V} the convective onset is delayed. This fact indicates that, higher shear velocity stabilizes

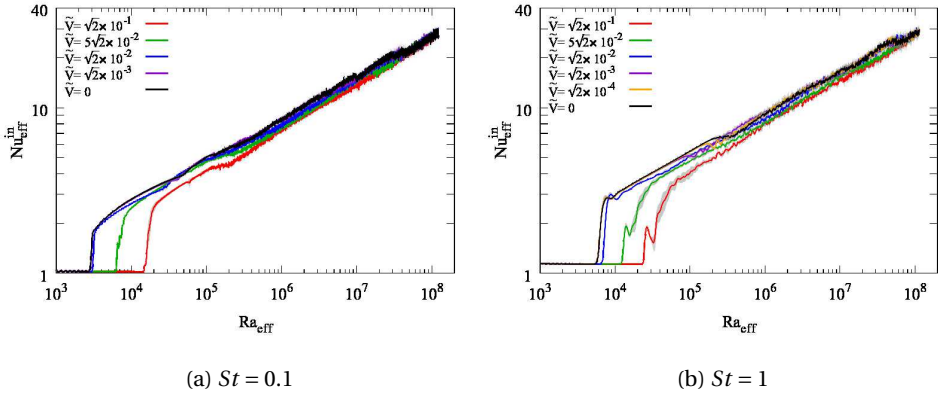


Figure 6.4 – Plot of inlet Nusselt number as a function of the effective Rayleigh for shear velocity $\tilde{V} = 0$ for reference and various shear velocities for two Stefan numbers of $St = 0.1$ and $St = 1$ for 2D CM systems.

the system, or in other words, higher buoyancy force is needed to destabilize the system into the convective regime. Similar behaviour has been observed in the stability analysis of the thermal Couette system¹ and reported by Joseph *et al.* [2]. Moreover, higher Stefan number also delays the onset of convection, as it can be observed in Fig.6.4.

The influence of the magnitude of \tilde{V} is very much reduced as Ra_{eff} increases, *i.e.* in the regime where buoyancy prevails. This indicates that, the behaviour of system tends to stay identical when the height of liquid fraction is advanced enough.

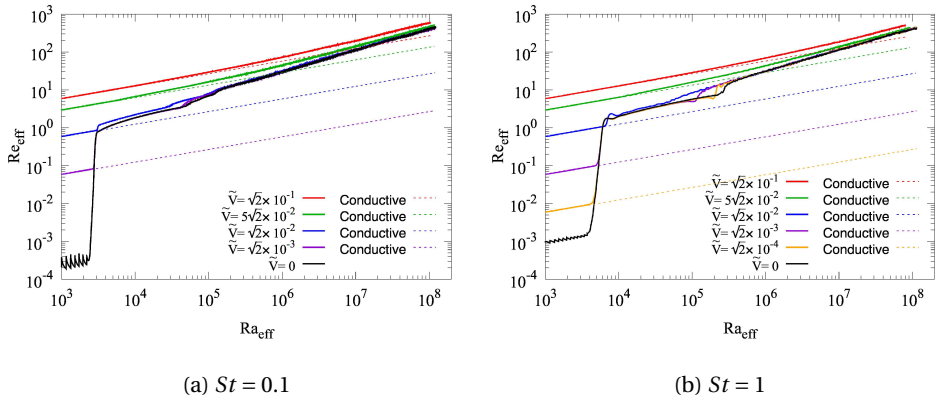


Figure 6.5 – Plot of the effective Reynolds with respect to the effective Rayleigh number, for shear velocity $V_x = 0$ as reference and various velocities of moving boundary for two Stefan numbers of $St = 0.1$ and $St = 1$ for 2D CM systems.

¹In fluid dynamics, Couette flow is the flow of a viscous fluid in the space between two surfaces, one of which is moving tangentially relative to the other.

6.2. Discussion

In order to complete this discussion, similar to what we did in chapter 5, we also look at the scaling of the global kinetic energy of the system, which in dimensionless form is defined as Reynolds number (Eq. (5.40)).

We observe from Fig. 6.5, that the agreement of the CM behaviour with different shear velocities is remarkable, particularly in the range $Ra_{eff} \geq 10^6$. At lower Ra_{eff} (particularly conductive regime) the appearing differences in Re_{eff} are due to the initial shear velocity; which can be computed analytically from Eq. (3.36) and using Eq. (5.39). We denote the analytic solution in Fig. 6.5 by dotted lines.

The total kinetic energy of the system of melting without moving boundary starts with relatively low value, and it follows with a jump at the onset of convection. The jump in the kinetic energy is induced from buoyancy force that triggers convection in the melting system. However, having velocity \tilde{V} at the moving boundary introduces additional velocities in the liquid layer. When the shear velocity exceeds certain value, it dominates buoyancy force, and the jump in the profile of kinetic energy disappears. The latter case can be seen for $\tilde{V} = 5\sqrt{2} \times 10^{-2}$ and $\tilde{V} = \sqrt{2} \times 10^{-1}$ in Fig. 6.5. To appreciate this effect, we can look in the relative changes of vertical kinetic energy ($u_{rms,z} H(t)/\nu$) to horizontal one ($u_{rms,x} H(t)/\nu$), which is shown in Fig. 6.6 for two values of Stefan number of $St = 0.1$ and $St = 1$.

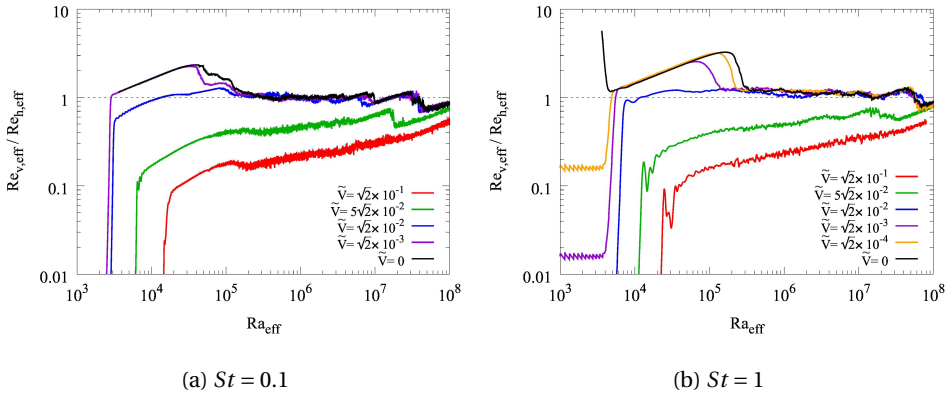


Figure 6.6 – Plot of relative vertical to horizontal effective Reynolds with respect to the effective Rayleigh number, for different shear velocity $\tilde{V} = 0$ as reference and $\tilde{V} = \sqrt{2} \times 10^{-1}$, $5\sqrt{2} \times 10^{-2}$, $\sqrt{2} \times 10^{-2}$, $\sqrt{2} \times 10^{-3}$, and $\sqrt{2} \times 10^{-4}$ for 2D CM systems.

In the case of an intensive wall velocity, although initially horizontal velocity is dominant, the advancement of the height of the liquid layer (*i.e.* increasing Ra_{eff} through the process of melting) promotes the buoyancy force, and consequently, the profile of kinetic energy marginally approaches to the one of melting system without shear velocity (Fig. 6.5). In other words, by advancing the melting front, the ratio of vertical to horizontal velocities approaches one (Fig. 6.6).

In summary, we have shown that different shear velocities affect the behaviour of the 2D CM system (in the range of parameters studied here $Pr = 10$, $St = 0.1$ and $St = 1$) for small values of Ra_{eff} , however, at higher Ra_{eff} such a difference seems to reduce

and eventually vanish.

6.2.2. Morphology of the interface

Apart from the dependency of the dynamics of the system to global control quantities, the shape of the solid-liquid interface can also be characterized quantitatively. Similarly, the focus is on the trends as a function of the Rayleigh number at fixed Stefan number and various velocities of the moving boundary.

Before analyzing the interface quantitatively, the advancement and behaviour of the interface can be observed qualitatively. Figure 6.7 shows the growth of interface stroboscopically. Two regimes of conduction and convection are separated by color code (red and blue) and each line represent different time steps. It can be observed that the convective roll patterns disappear with the increase of \tilde{V} .

As in chapter 5, for different velocities of the moving boundary, we characterize the shape of the solid-liquid interface at a given time by one dimensional auto-correlation function of local interface height (Eq. (5.42)), and the roughness of the interface (Eq. (5.45)).

The computed L_c , normalized by the average height of the liquid fraction ($H(t)$), as a function of the Ra_{eff} is shown in figures 6.8a and 6.8b for two Stefan numbers, $St = 0.1$ and $St = 1$ respectively. As we already know, at small Ra_{eff} , the system dynamics is purely conductive and as a result the interface is flat, in such a case L_c is not defined. Later on, the onset of convection produce a finite L_c as it drives the formation of recirculating patterns (cells) with an aspect ratio ~ 1.5 . The ratio $L_c/H(t)$ decreases because the number of convective rolls remain constant while the average height of the melted layer increases.

The behaviour of solid-liquid interface, however, depends highly on the magnitude of moving boundary. As we observed in the previous section, there is a transition in the behaviour of system for great shear velocity (Fig. 6.6). In case of intensive velocity of the moving boundary, the horizontal force is more dominant. Therefore, the melting in the interface takes place more horizontally at the onset of convection, and consequently the correlation length (L_c) increases significantly.

Asymptotically, by increase of height of interface, the vertical force (buoyancy) increases. Therefore, the elongation of rolls gradually diminishes, and eventually correlation approaches commonly seen state, which is typical aspect ratio 1 and this appears to be independent of the dimensionality of the system. The latter one is a feature also present in (flat-wall) RB systems [3].

Similarly, the average roughness of the liquid-solid interface can be quantified by means of the standard deviation of the fluid-solid boundary height, z_m , and is defined by Eq. (5.45). The evolution of the normalized fluctuation $\sigma_{z_m}(t)/H(t)$ with respect to Ra_{eff} is shown in figures 6.8c and 6.8d.

Similar to correlation function, the roughness of solid-liquid interface behaves differently with respect to strong shear velocity. However, in this case, the roughness of interface reduces for stronger velocity on the moving boundary. As we discussed previously, the incoming heat flux into the system varies little for different shear velocities. Consequently, rate of overall melting stays constant. Therefore, elongation in one direction (here horizontally) will be followed by shortening in another direction (vertically).

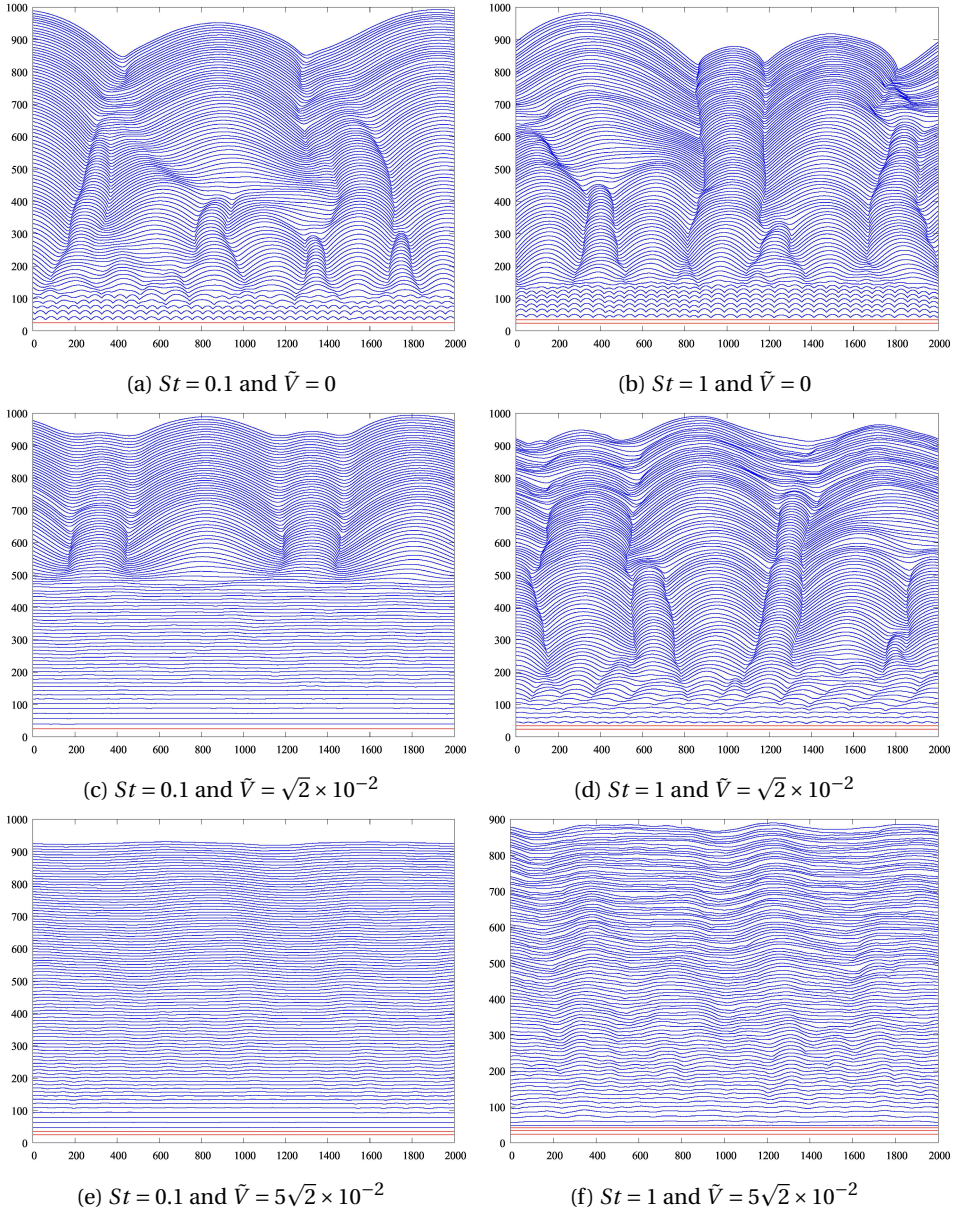


Figure 6.7 – Stroboscopic visualization of advancement of solid-liquid interface for Stefan number $St = 0.1$ and 1 , and shear velocities $\tilde{V} = 0$, $\tilde{V} = \sqrt{2} \times 10^{-2}$ and $5\sqrt{2} \times 10^{-2}$. The red lines indicate conductive and blue one the convective regimes

In summary, we saw that the morphology of the interface depends on the magnitude of velocity of the moving boundary. When the shear velocity is high enough, the

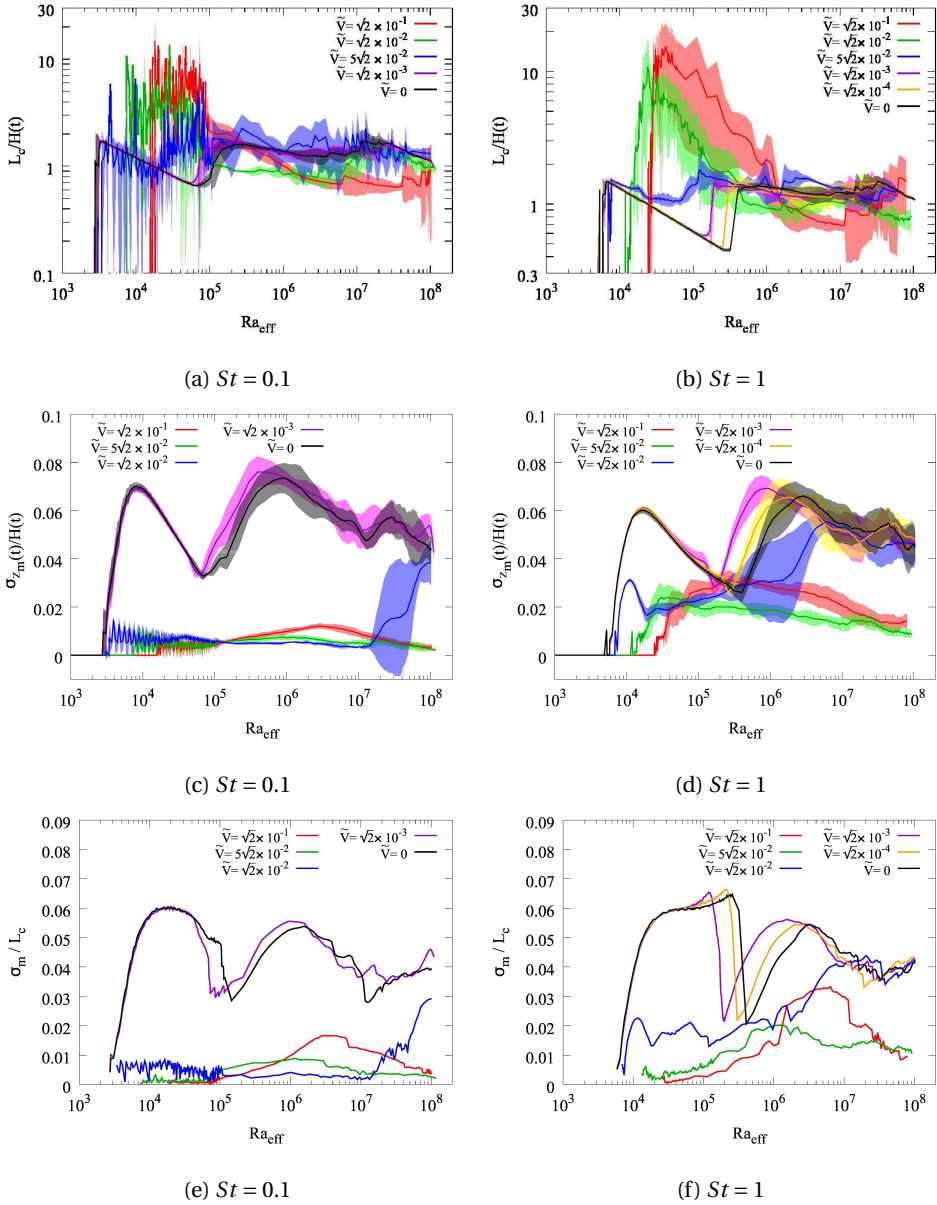


Figure 6.8 – Ensemble averaged auto-correlation length and deviation of melting interface for 2D simulation versus Ra_{eff} for different shear velocities and Stefan number $St = 0.1$ and $St = 1$. For simulations, the domes do not reach the width of the system, i.e., $L_c/W < 1$. The shaded area is the range between minimum and maximum of the all instances of simulations. The axis are the width and height of the simulations, which for simplicity are shown in grid size.

6.3. Conclusion

horizontal kinetic energy surpasses the buoyancy force, and the roll formation would be elongated horizontally. Consequently, the number of rolls appearing in the liquid layer reduces relatively. This can be identified by having larger correlation of interface. On the other hand, the horizontal velocity field induced by velocity of moving boundary, flattens the interface and make the deviation smaller.

6.3. Conclusion

In this work, we addressed the problem of Convective Melting (CM) coupled with a moving boundary condition with different intensities. We observed that when the velocity of the moving boundary is high enough so that horizontal kinetic energy is dominant, the CM system shows different behaviour in terms of the Reynolds and the Nusselt numbers at low Rayleigh. However, at ultimate high Ra such a difference seems to reduce and eventually vanish. Moreover, we presented direct dependency between intensity of shear velocity with delay in onset of convection.

In addition we studied the morphology of the interface for different velocities of moving boundary, and we again observed direct dependency between intensity of shear velocity and elongation of rolls. Moreover, elongated rolls curve less vertically in the solid-liquid interface. Consequently the thickness of melting front reduces by increase in the intensity of velocity of moving boundary.

Wind may play an important role when considering laterally bounded ponds, as it introduces an asymmetry on the melting rate of the side walls. The effects of introducing a moving boundary on the laterally confined CM system is a natural extension of the work presented in this chapter, and may shed light on the influence of wind shear on the evolution of melt ponds.

References

- [1] E. D. Skillingstad and C. A. Paulson, *A numerical study of melt ponds*, Journal of Geophysical Research: Oceans **112** (2007).
- [2] D. D. Joseph, *Variable viscosity effects on the flow and stability of flow in channels and pipes*, The Physics of Fluids **7**, 1761 (1964).
- [3] E. P. van der Poel, R. J. A. M. Stevens, and D. Lohse, *Comparison between two- and three-dimensional Rayleigh-Bénard convection*, [Journal of Fluid Mechanics](#) **736**, 177–194 (2013).



7

Convective melting with volumetric heat source

The heat exchange between earth and space is maintained by two great fluxes of radiative energy, incident solar radiation and leaving longwave radiation from the earth's surface and atmosphere. These fluxes are usually much larger than other terms in the energy budget, such as evaporation, sensible heat exchange, and advection [1]. The incident fluxes can be classified into shortwaves and longwaves, and among the two the shortwave flux is the most relevant one. [2]

The shortwave solar radiation is absorbed in the liquid layer of melt-ponds inhomogeneously, in particular it decreases with the depth. The macroscopic absorption law that is most commonly used is the Beer-Lambert law [3]. Skyllingstad *et al.* [4] adopted this law in their work in form of

$$F_r(z) \downarrow = P_m F_{rn} (1 - e^{-K_m z}), \quad (7.1)$$

where F_r is solar flux parametrization using a radiative transfer equation developed by observation during SHEBA experiment (Pegau [5]), and F_{rn} represents the solar flux as the net shortwave radiation at the sea surface. Moreover, P_m is the proportion of shortwave energy in the band m , K_m is the diffuse extinction coefficient, and z is the depth below the surface. Information on the band characteristics is provided in Table 7.1.

Shortwave radiation reaching the pond bottom is either reflected upward by the ice under the pond or transmitted below the pond. Similarly, Skyllingstad *et al.* [4] proposed

$$F_r(z) \uparrow = P_m a_b F_r(z_b) (1 - e^{-K_m [(z_b - z)]}), \quad (7.2)$$

as absorption of radiation reflected off the bottom, with $F_r(z_b)$ the radiation intensity at the bottom of the pond, z_b depth, and a_b the pond bottom albedo. Using $F_r(z) \downarrow$ and $F_r(z) \uparrow$, the total amount of the heat absorbed in the melt-pond can be calculated as a function of depth by integrating the downwelling and upwelling radiation

$$Q_r = \int_h F_r(z) \downarrow + \int_h F_r(z) \uparrow. \quad (7.3)$$



Therefore, in this method, the conservation of energy reads

$$\rho c_p \partial_t T + \mathbf{u} \cdot \nabla T = \Lambda \nabla^2 T + \partial_z F_r(z) \downarrow + \partial_z F_r(z) \uparrow, \quad (7.4)$$

where Λ is thermal conductivity.

In the present work we consider a simplifying assumption of a constant radiative heat source on the pond, and homogeneous solar flux parametrization (\bar{q}), which represents mean solar flux of non-homogeneous model. Therefore, we have

$$\bar{q} = \frac{1}{z_b} \int_0^{z_b} \partial_z F_r(z) \downarrow + \partial_z F_r(z) \uparrow dz \quad (7.5)$$

$$= \frac{1}{z_b} (F_r(z_b) \downarrow - F_r(0) \downarrow) + \frac{1}{z_b} (F_r(z_b) \uparrow - F_r(0) \uparrow) \quad (7.6)$$

$$= \frac{1}{z_b} \left(F_{rn} \sum_m P_m (1 - e^{-K_m z_b}) \right) - \frac{1}{z_b} \left(a_b F_r(z_b) \sum_m P_m (1 - e^{-K_m z_b}) \right) \quad (7.7)$$

$$= \frac{F_{rn}}{z_b} \left(1 - a_b \sum_m P_m (1 - e^{-K_m z_b}) \right) \left(\sum_m P_m (1 - e^{-K_m z_b}) \right), \quad (7.8)$$

which in non-dimensional form reads

$$\bar{Q} = \frac{\bar{q} z_b^2}{\Lambda \Delta T}. \quad (7.9)$$

In order to have better understanding of different bulk-heating intensity, one can estimate the corresponding depth of melt-pond by using Eq. (7.9) and table 3.5. In our computation, we use representative value of 160 W/m^2 for the solar flux (F_{rn}), which is taken from measurements done by Pegau and Paulson [5]. The plot of Eq. (7.9) with respect to melt-pond depth with bottom pond albedo $a_b = 0.6$ is shown in Fig. 7.1. It can be seen that homogeneous and constant bulk-heating coefficients $Q = 50$ and $Q = 250$, which we use in our simulations, correspond to melt-pond of depths 40 cm and 1.57 m with non-homogeneous radiative heat source in the pond, respectively.

Wavelength Range	350 – 700 nm, $m = 1$	700 – 900 nm, $m = 2$	900 – 1100 nm, $m = 3$	> 1100 nm, $m = 4$
P_m	0.481	0.194	0.123	0.202
K_m	0.18	3.25	27.5	300

Table 7.1 – Band characteristics used to determine the shortwave radiation absorbed in a freshwater layer. P is a function of cloud conditions, and K is a function of material in the water.

The table is courtesy E.Skylingstad *et al.* [4]

In this chapter, we analyze the behaviour of the CM system heated through both thermal boundary condition and constant volumetric heat source. Similar to previous chapters, we present the behaviour of CM system at turbulent state, *i.e.* high Rayleigh number, and address the characterization of the shape of the solid-liquid phase-change interface.

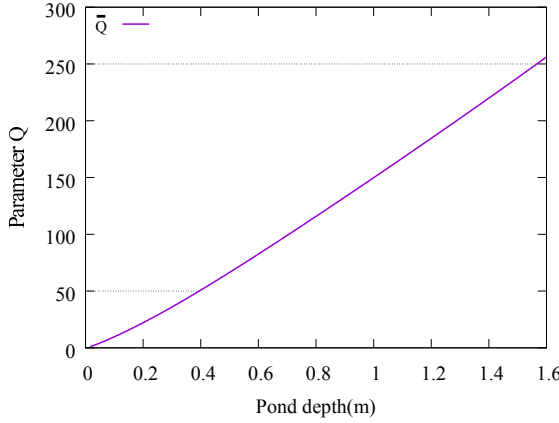


Figure 7.1 – Plot of corresponding solar flux for different melt-pond depths.

7.1. Convective melting system with volumetric heat source

For the study of effect of volumetric heat source (also called bulk heating) on dynamics of melting system, we consider a model system which consists of a solid layer of a pure substance of thickness H_{max} initially at a constant temperature T_m . We start to heat the system with a constant temperature T_0 , and simultaneously when the liquid layer appears in the system, the constant volumetric heat q is added to the liquid part. Here q is considered as the radiative power flux of solar radiation.

7.1.1. Equations of motion

The equations describing the dynamics of the system are Navier-Stokes (Eq. (5.1), (5.2) and (5.3)), together with temperature equations with constant bulk heating coefficient, which is Eq. (3.61). For the boundary condition associated to CM system with bulk heating are: (i) fixed temperature at the bottom wall together with no-slip condition for velocity, (ii) periodic boundary condition at lateral boundaries, and finally (iii) no slip and melting conditions at the phase-change interface. Equations describing the boundary conditions are (5.5)-(5.8).

Similar to what we did in chapter 5, the temperature equation (3.61) together with the associated phase-change boundary conditions (5.7) can be reformulated in form of a single equation. This results in

$$\frac{\partial T}{\partial t} + (\mathbf{u} \cdot \nabla) T = \kappa \nabla^2 T - \frac{\mathcal{L}}{c_p} \frac{\partial \phi_l}{\partial t} + \frac{q}{\rho_0 c_p} \phi_l, \quad (7.10)$$

which by non-dimensionalizing temperature by the temperature difference $\Delta T = T_0 - T_m > 0$, the density by ρ_0 , the length by H_{max} and finally the time by the diffusive time H_{max}^2/κ , results in

$$\frac{\partial \tilde{T}}{\partial \tilde{t}} + (\tilde{\mathbf{u}} \cdot \nabla) \tilde{T} = \nabla^2 \tilde{T} - \frac{1}{St} \frac{\partial \phi_l}{\partial \tilde{t}} + Q \phi_l, \quad (7.11)$$

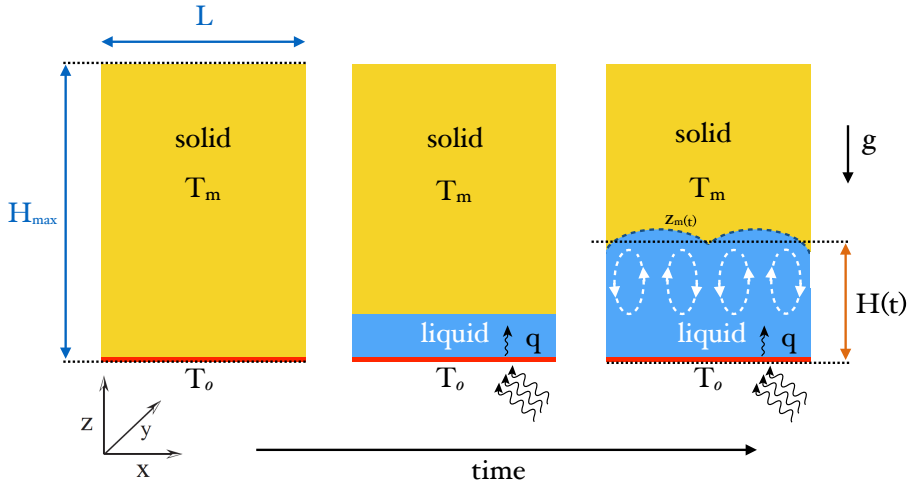


Figure 7.2 – Schematic diagram of the melting system. The system is filled with a pure solid at the temperature of melting (T_m) and the bottom at temperature T_0 which is higher than the melting temperature. When the liquid layer starts to grow in the system, constant volumetric heat q is added homogeneously to the liquid part.

where Q is radiative over conductive flux ratio, and can be identified as the global control parameter for the system melting coupled with volumetric heating, and is defined as

$$Q = \frac{H_{max}^2}{\kappa \Delta T} \frac{q}{\rho_0 c_p}. \quad (7.12)$$

Other global parameters are as we saw in previous chapters: the Prandtl number (Pr) (Eq. (5.14)), the Rayleigh number (Ra) (Eq. (5.15)), and the Stefan number (St) (Eq. (5.16)).

7.1.2. Global heat-flux balance

We begin by considering the equation for the temperature in the fluid domain with the moving interface formulation of Eq. (7.10). In conservative form (7.10) reads:

$$\partial_t T + \nabla \cdot (\mathbf{u}T - \kappa \nabla T) + \frac{\mathcal{L}}{c_p} \frac{\partial \phi_l}{\partial t} - \frac{q}{\rho_0 c_p} \phi_l = 0. \quad (7.13)$$

We take the volume integral over the whole domain and apply the divergence theorem

$$\int_V \partial_t T dx^3 + \int_{\partial V} \mathbf{n} \cdot (\mathbf{u}T - \kappa \nabla T) dS + \frac{\mathcal{L}}{c_p} \int_V \frac{\partial \phi_l}{\partial t} dx^3 - \int_V \frac{q}{\rho_0 c_p} \phi_l dx^3 = 0. \quad (7.14)$$

In Eq. (7.14), due to having lateral periodic boundary condition, no-slip boundary condition at the bottom, and constant temperature in the solid part ($\nabla T = 0$ in solid),

7.2. Discussion

the second term will vanish. Moreover, as the volumetric heating is only introduced in the liquid layer, the last integral reduces to liquid domain. By having also constant bulk-heating coefficient, Eq. (7.14) simplifies to

$$\int_V \partial_t T dx^3 - L^2 \left\langle -\kappa \frac{\partial T}{\partial z} \right\rangle_{z=0} + L^2 H_{max} \frac{\mathcal{L}}{c_p} \langle \phi_l \rangle \frac{\partial \langle \phi_l \rangle}{\partial t} - L^2 H(t) \frac{q}{\rho_0 c_p} \langle \phi_l \rangle = 0. \quad (7.15)$$

By normalizing by the horizontal bottom surface (L^2), temperature by the temperature gap $\Delta T = T_0 - T_m > 0$, the density by ρ_0 , the length by H_{max} and finally the time by the diffusive time H_{max}^2/κ , and rearranging the terms and using the definition of Stefan number and $H(t)$ we get:

$$-\left\langle \frac{\partial \tilde{T}}{\partial \tilde{z}} \right\rangle_{\tilde{z}=0} \rangle_A = \langle \partial_{\tilde{t}} \tilde{T} \rangle + \frac{1}{St} \langle \phi_l \rangle \frac{\partial \langle \phi_l \rangle}{\partial \tilde{t}} - Q \langle \phi_l \rangle^2. \quad (7.16)$$

Similar to the discussion in chapter 5, we define

$$Nu_{eff}^{bot} = -\left\langle \frac{\partial T}{\partial z} \right\rangle_{z=0} \rangle_A \langle \phi_l \rangle, \quad (7.17)$$

$$Nu_{eff}^{top} = \frac{1}{St} \langle \phi_l \rangle \frac{\partial \langle \phi_l \rangle}{\partial \tilde{t}} = \frac{1}{2St} \frac{\partial \langle \phi_l \rangle^2}{\partial \tilde{t}}, \quad (7.18)$$

which are the dimensionless average heatflux at the bottom boundary and solid-liquid interface. Moreover, in the present study, we address the rate of incoming heat into the system through volumetric heating, and we are interested in effective quantities. Therefore, with respect to equation (7.16), we define

$$Q_{eff} = \langle \phi_l \rangle^2 Q, \quad (7.19)$$

which is total incoming bulk heating in the liquid part, and consequently, the system.

7.2. Discussion

In this section, we look at the result of numerical simulations computed by our DNS. For each simulation, all the parameters, except the constant volumetric heat ($\frac{q}{\rho_0 c_p}$), are kept fixed. The values of parameters are summarized in table 7.2. In order to reduce the effect of initial perturbation applied on each simulation, for each volumetric heating parameter, ensemble average over several simulations are employed.

By considering the global liquid fraction, similar to the case of melting, we can introduce the effective Rayleigh number (Eq. (5.19)). Likewise, in order to quantify the results, similar to Rayleigh-Benard system, we look to heat budget in form of the dimensionless Nusselt number, which we measure at the bottom and the solid-liquid interface through equations (7.17) and (7.18) respectively.

Before presenting the results in quantitative scheme, similar to previous fashion, we look in the behaviour of CM system with volumetric heating (Fig. 7.3) with the system of CM (Fig. 6.2) qualitatively. First observation is the shape of solid-liquid interface, which is more distorted vertically in the CM system coupled with bulk heating. The depth of

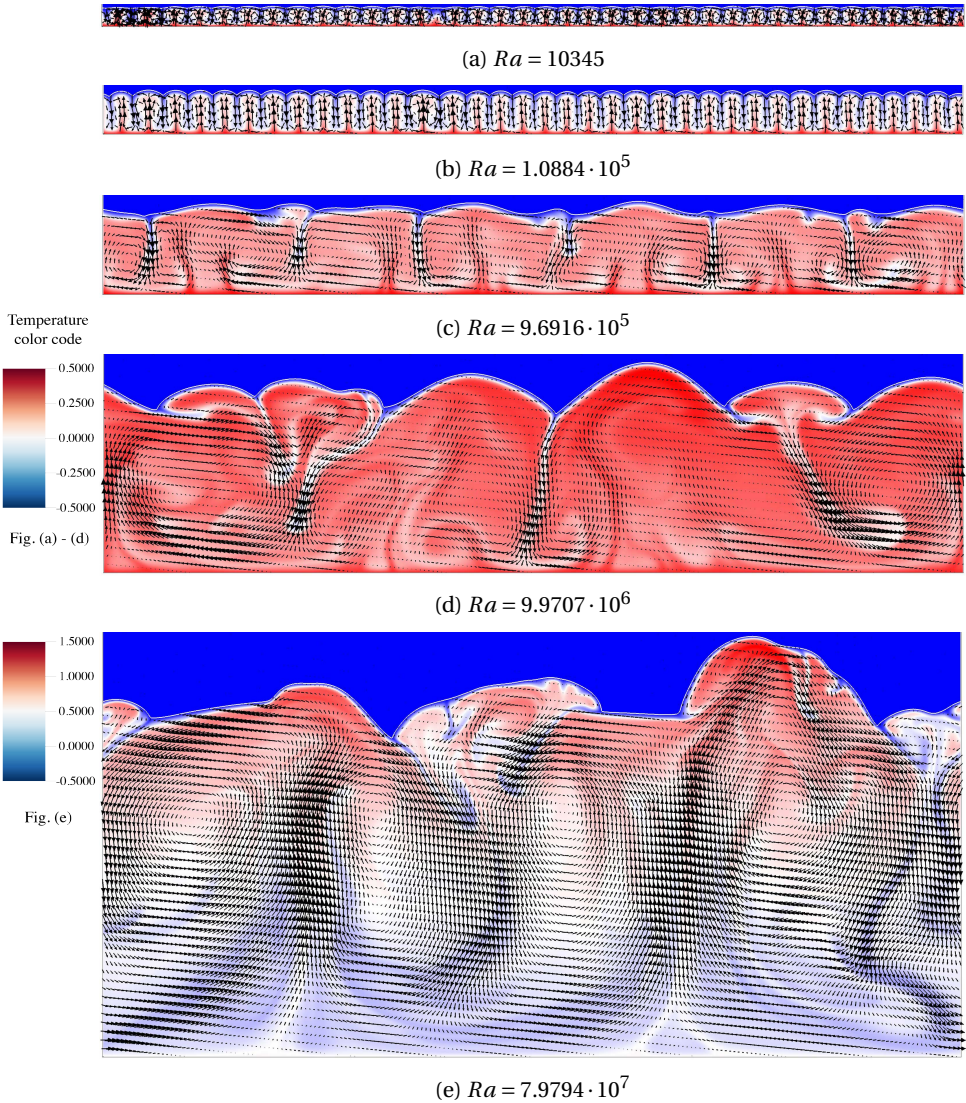


Figure 7.3 – Visualization of the 2D CM system in different stages at increasing effective Rayleigh numbers. The global parameters of the system are $St = 1$, $Pr = 10$, and $Q = 250$. The colors represent the temperature field, and the arrows are the velocity field normalized by the magnitude of the maximum velocity in each field separately. The white line in each visualization is the solid-liquid interface. The temperature field for figure (a-d) is in range -0.5 to 0.5 , whereas for the figure (e), the color code for the temperature is from -0.5 to 1.5 .

the domes in the solid-liquid interface is relatively higher for the system of melting with volumetric heating. We will address these observations more quantitatively later, in form

<i>number of runs</i>	L_x	L_y	ν	κ	β	ΔT	g	\mathcal{L}	c_p	Pr	St	Ra_{max}	Q
6	2000	1000	0.2	0.02	$5 \cdot 10^{-4}$	1	1	1	1	10	1	$1.25 \cdot 10^8$	0
6	2000	1000	0.2	0.02	$5 \cdot 10^{-4}$	1	1	1	1	10	1	$1.25 \cdot 10^8$	50
6	2000	1000	0.2	0.02	$5 \cdot 10^{-4}$	1	1	1	1	10	1	$1.25 \cdot 10^8$	250
6	2000	1000	0.2	0.02	$5 \cdot 10^{-4}$	1	1	1	1	10	1	$1.25 \cdot 10^8$	500

Table 7.2 – Summary of the parameters values for all convective melting simulations. We provide dimensional and dimensionless control parameters. The dimensional parameters are in numerical units. The time-step is fixed $\delta t = 1$ for all simulations. The second column from left (*number*) specifies the number of simulations performed, which are employed to estimate the ensemble averages.

of analyzing the solid-liquid interface. Second observation is the location of center of largest vortices in the liquid layer, which has shifted higher and closer to the melting front. This observation is more evident especially in fully developed system, e.g. Fig. 7.3e compared to Fig. 6.2e.

In order to analyze the system of melting coupled with bulk heating, the results presented in this section are categorized into two different analysis. The first one is the effect of global quantities on the dynamics of the system. And secondly, the characterization of interface roughness and morphology, and its coupling effects on flow in the liquid layer.

7.2.1. Results on global quantities

In order to address quantitatively the dynamics of the bulk heated CM system we study the intensity of global heat flux Nu_{eff}^{top} as a function of the forcing imposed to the system, which in this case is parameterized not only by Re_{eff} but also by Q_{eff} . The rationale for the choice of the heat-flux at the solid-liquid interface is the presence of volumetric heating, which may affect in a relevant way the melt-rate. Conversely an investigation on Nu_{eff}^{bot} , as done in the previous chapters, would not provide here a direct information of the advancement of the phase-change process. A minor drawback of this approach is that we have to cope with more noisy signal, due to numerical discretization effects which are unavoidably present at the phase-change interface

Figure 7.4 shows Nu_{eff}^{top} for two-dimensional CM with different bulk-heating intensities for Stefan number $St = 1$. Few observations are in order:

First of all, the behaviour of Nu_{eff}^{top} can be roughly categorized into two regimes. The first regime is where internal heating is weak with respect to heating coming to the system through bottom boundary (the air-water interface in the pond system). Therefore, we have scaling of $Nu \sim Ra^{1/3}$, which we already know from the analysis of CM system without bulk heating (Chapter 5), and a dynamics that is very close to the one of the RB system. The second regime is when the homogeneous internal heating dominates over the inlet heat from the bottom surface. In this regime, we see the emerging of the behaviour of $Nu \sim Ra^{2/3}$.

In order to explain this novel regime, we observe (again from figure 7.4) that the

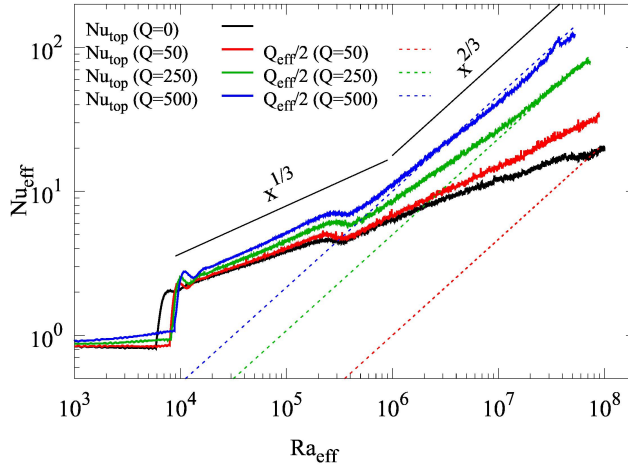


Figure 7.4 – Plots of heat flux measured as Nusselt number at the solid-liquid interface as a function of the effective Rayleigh number for different volumetric bulk-heating intensities for 2D CM systems, together with the plot of half volumetric bulk-heating. The two black lines indicate two scaling of $1/3$ and $2/3$ which are described in the text.

in the asymptotic Ra_{eff} limit the Nu_{eff}^{top} seems to approach the value of $Q_{eff}/2$. This observation indicates that the heat going out through the solid-liquid interface is, in fact, approximately half of the internal heating in the system. Therefore, for large Ra , the following relation holds:

$$\frac{1}{St} \langle \phi_l \rangle \frac{\partial \langle \phi_l \rangle}{\partial \bar{t}} \approx \frac{1}{2} \langle \phi_l \rangle^2 Q, \quad (7.20)$$

which by simplifying and considering the solution of the ordinary differential equations of the form $\partial_t u = u$ one obtains:

$$\langle \phi_l \rangle \sim e^{St Q \bar{t}/2}. \quad (7.21)$$

Equation (7.21) shows that, in the presence of internal heating, the melt process can advance much faster than in the RB-like convective regime. The change is from a constant melt front velocity (v_m) in the contact heating dominated regime to an exponential velocity. This behaviour is shown in Fig. 7.5 with exponential fitting to the plots, showing that the velocity of the interface increases exponentially by the intensity of the volumetric heating. The fitting is of the form $A e^{B St Q \bar{t}/2}$, where in Fig. 7.5 the coefficient A is not shown. Our computation shows that B is of order one, and decreases for larger internal heating coefficient.

It can be seen in Fig. 7.5 that, the exponent for $Q = 500$ is clearly twice the case for $Q = 250$. This behaviour is consistent with the theory, in which we have the dependency of the heat-flux to the half internal heating. We shall note that, such a melting regime to our knowledge has never been reported before.

Finally we can put forward an explanation for the $Nu \sim Ra^{2/3}$ scaling relation by

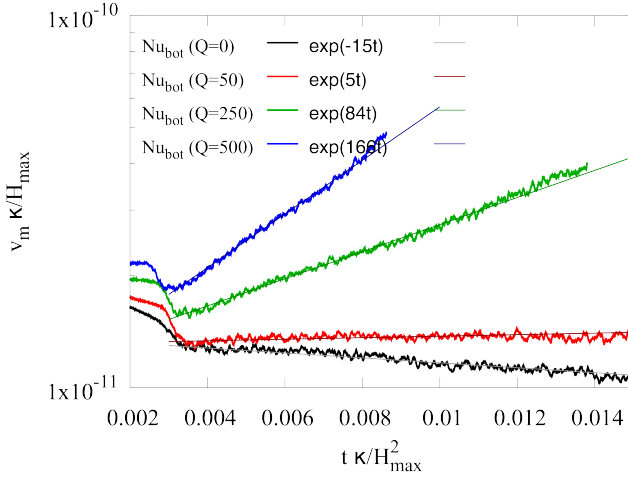


Figure 7.5 – Plot of the velocity of the interface for different volumetric bulk-heating intensities for 2D CM systems. In the case $Q = 0$ we have no special reason to fit with an exponential

using the fact that Nu_{eff}^{top} approaches to $Q_{eff}/2$ at high Ra_{eff} . We have

$$Nu_{eff}^{out} \sim \langle \phi_l \rangle^2 Q. \quad (7.22)$$

Similar to what we did in Chapter 5, one can substitute $\langle \phi_l \rangle$ with the one from the definition of Rayleigh number (*i.e.* $Ra_{eff} = \langle \phi_l \rangle^3 Ra_{max}$, Eq. (5.19)). This results in

$$Nu_{eff}^{out} \sim Ra_{eff}^{2/3} Q. \quad (7.23)$$

The fact that the heat going out through the solid-liquid interface is half the internal heating in the system is probably just a rough approximation. Goluskin *et al.* [6, 7], who carefully investigated the case of thermal convection due to the sole internal heating in the system of Rayleigh-Bénard concluded that an asymmetry is indeed present, and that the heat-flux at top is slightly larger than the one going through the bottom.

We now look at the behaviour of the global kinetic energy of the system, which in dimensionless form takes the form of the Reynolds number (Eq. (5.40)).

The Reynolds number as a function of the effective Rayleigh number for different Q values is reported in Fig. 7.6. As for the Nusselt number one can distinguish two regimes. A first one where the effect of internal heating is negligible and the system shows the $Re_{eff} \sim Ra_{eff}^{1/2}$ scaling, already known from the RB system, and a second one where the scaling increases to $Re_{eff} \sim Ra_{eff}^{5/6}$. The latter effect can be attributed to a high buoyancy force which stems from greater temperature differences, provoked by internal heating in the liquid.

The two scalings originate from different relevant velocity scales. While in the RB case one can hypothesize that the magnitude of the velocity is given by the so called

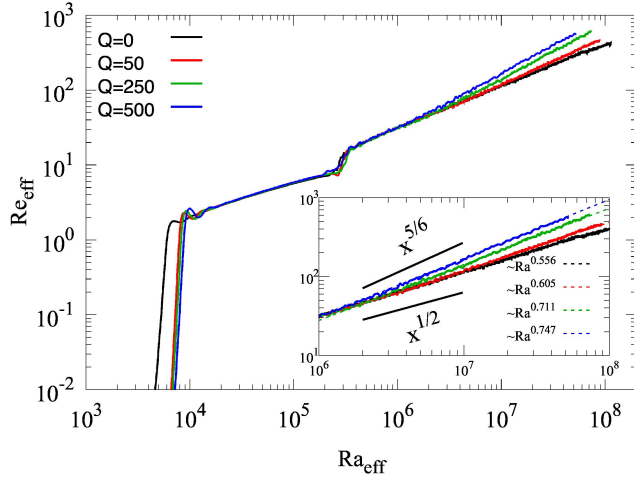


Figure 7.6 – Plot of the effective Reynolds as defined in eq.(5.40) with respect to the effective Rayleigh number for different volumetric bulk-heating intensities for 2D CM systems.

free fall velocity, which originates from temperature differences imposed by the system boundaries and reads:

$$v_{temp} = \sqrt{\beta g \Delta T H(t)}, \quad (7.24)$$

in the second regime the temperature differences are originated by the volumetric heat rate, as follows:

$$v_{bulk} = \sqrt{\beta g \frac{q}{c_p \rho_0 \kappa} [H(t)]^3}. \quad (7.25)$$

Substituting the two above definitions in Eq. (5.40), and using the definition of Ra_{eff} (Eq. (5.19)), result in two scalings of

$$Re_{temp} \sim [H(t)]^{3/2} \sim Ra_{eff}^{1/2}, \quad (7.26)$$

for when temperature difference is dominant, and

$$Re_{bulk} \sim [H(t)]^{5/2} \sim Ra_{eff}^{5/6}, \quad (7.27)$$

in case where bulk heating is dominant. The second regime corresponds to a state of high-mixing in the liquid layer, and so of high homogenization of temperature in a hypothetical pond. These two extremes are illustrated in figure 7.6.

7.2.2. Morphology of the interface

Apart from the dependency of the dynamics of the system to global control quantities, the shape of the solid-liquid interface also can be characterized quantitatively. Similarly, the focus is on the trends as a function of the Rayleigh number at fixed Stefan number

7.2. Discussion

and various volumetric bulk-heatings. With this in mind, we deliberately consider simple quantifiers of the boundary roughness that can be applied to systems with different Q intensity.

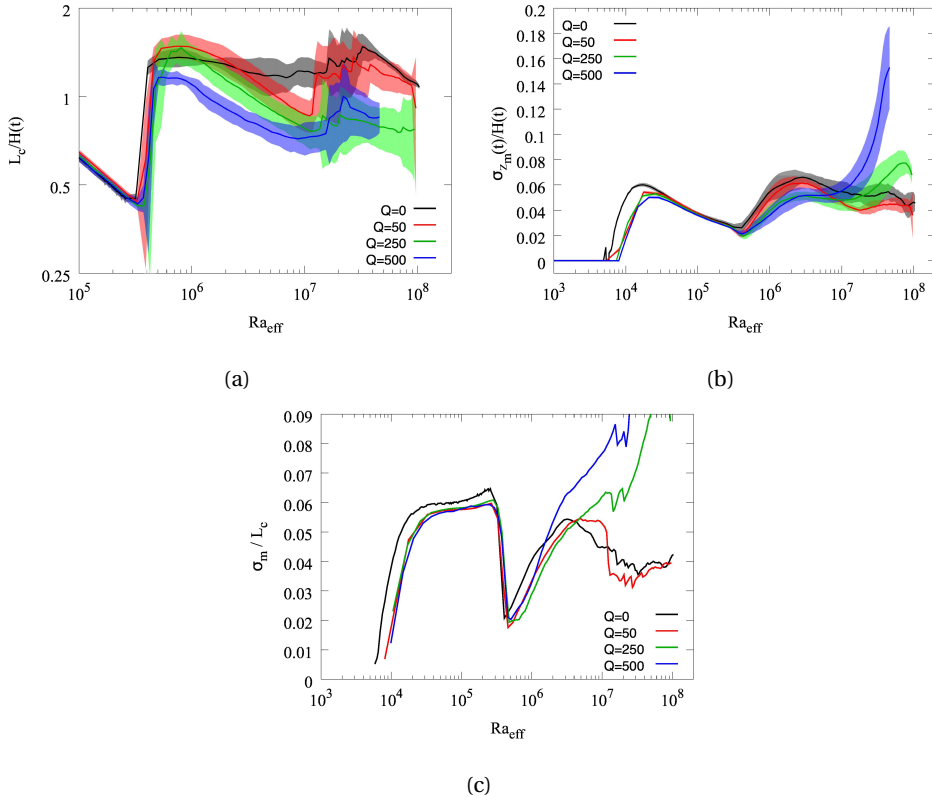


Figure 7.7 – Ensemble averaged auto-correlation length and deviation of melting interface for 2D simulation versus Ra_{eff} for different volumetric bulk heating intensities. For simulations, the domes do not reach the width of the system, i.e., $L_c/W < 1$. The shaded area represents the range between minimum and maximum of the all instances of simulations.

In a similar fashion to previous chapters, we quantify the behaviour of the interface by looking at the correlation length and the deviation of the interface.

The computed L_c , normalized by average height of the liquid fraction ($H(t)$), as a function of the Ra_{eff} number is shown in figure 7.7a. As we already know, at small Ra_{eff} , the system dynamics is purely convective and as a result the interface is flat, in such a case L_c is not defined. Later on, the onset of convection produce a finite L_c as it drives the formation of recirculating patterns (cells) with an aspect ratio ~ 1 . The ratio $L_c/H(t)$ decreases because the number of convective rolls remain constant while the average height of the melted layer increases.

Although the overall behaviour of correlation function of melting system with volumetric bulk heating is similar to pure melting system, however for ultimate large Ra

regime, the aspect ratio of the cells has tendency to stay below unity (< 1). This tendency is coming from the fact that bulk-heating introduces stronger vertical forces, which is due to existence of higher temperature differences, which in return follows with higher buoyancy force.

Similarly, the average roughness of the liquid-solid interface can be quantified by means of the standard deviation of the fluid-solid boundary height, z_m , which is defined by Eq. (5.45).

The roughness of solid-liquid interface depends highly to the magnitude of bulk-heating. Unlike slip velocity, which produces stronger horizontal force, bulk-heating introduces stronger vertical force. Therefore, the solid-liquid interface in the system of melting with bulk-heating shows higher roughness, especially at high Ra . This roughness at ultimate high Ra is due to having large liquid fraction, which in return causes more intensive absorption and accumulation of heat from internal heating.

In summary, we saw that the morphology of the interface depends on the magnitude of volumetric bulk-heating. When the bulk-heating coefficient is present, it induces higher vertical forces due to the existence of larger temperature differences, which in return produce larger buoyancy force. This vertical force elongates rolls vertically, especially for ultimate high Ra , where liquid fraction is large enough to absorb larger bulk-heating.

7.3. Conclusion

In this chapter, we addressed the problem of Convective Melting (CM) coupled with internal heating through volumetric heating with different intensities. The analysis presented in this work, categorized into two sections; effect of global control parameters and morphology of the interface.

We observed that when bulk heating coefficient is high enough so that vertical kinetic energy due to buoyancy force is dominant, the CM system shows different behaviour. However, while the Reynolds and the Nusselt numbers at low Rayleigh are similar to pure convective melting, at ultimate higher Ra the system of melting coupled with bulk heating shows a higher rate of melting.

Also, we observed that by the advancement of the solid-liquid interface, the internal heating dominates the heating through bottom interface. Consequently, the implication of this result is the two-third scaling relation of the outgoing heat to Ra . In addition, kinetic energy of the system shows scaling of five-sixth at ultimate high Rayleigh.

Moreover, we presented that in the system of melting heated internally, the velocity of the solid-liquid interface behaves exponentially with respect to magnitude of volumetric bulk heating and Stefan number. This result indicates a new regime, which has not been considered in any large-scale model.

Apart from the internal dynamics of the system, we studied the morphology of the interface for different bulk heating intensity, and we again observed direct dependency between intensity of bulk heating coefficient and vertical elongation of roll.



References

- [1] M. Sandells and D. Flocco, *Introduction to the Physics of the Cryosphere*, IOP Concise Physics: A Morgan & Claypool Publication (Morgan & Claypool Publishers, 2014).
- [2] R. G. Allen, L. S. Pereira, D. Raes, M. Smith, *et al.*, *Crop evapotranspiration-guidelines for computing crop water requirements-fao irrigation and drainage paper 56*, **FAO, Rome 300, D05109 (1998)**.
- [3] D. Calloway, *Beer-lambert law*, *J. Chem. Educ* **74**, 744 (1997).
- [4] E. D. Skyllingstad and C. A. Paulson, *A numerical study of melt ponds*, *Journal of Geophysical Research: Oceans* **112** (2007).
- [5] W. S. Pegau, *Inherent optical properties of the central arctic surface waters*, *Journal of Geophysical Research: Oceans* **107** (2002).
- [6] D. Goluskin and E. A. Spiegel, *Convection driven by internal heating*, *Physics Letters A* **377**, 83 (2012).
- [7] D. Goluskin and E. P. van der Poel, *Penetrative internally heated convection in two and three dimensions*, *Journal of fluid mechanics* **791** (2016).



8

Conclusion and perspectives

One of the main challenges of climate science today is the prediction of rate of ice melt in the Arctic. The dynamics of melting in the sea ice is linked to the amount of reflection of solar radiation, which is known as albedo. Lighter areas, for instance snow covered surface of ice, reflect more radiation than darker areas. One of the most important dark surfaces in the Arctic are melt-ponds; that covers large portions of sea ice during summer time.

Several models have been proposed to quantify the influence of melt-ponds on albedo feedback as well as their distributions on sea ice. However, in most of the models, the internal dynamics of melt-ponds (fluid dynamics and turbulence) has been neglected. The aim of this thesis was to investigate in great details the aspects related to convection coupled to phase-change of a single melt pond, and we were interested in obtaining more quantitative predictions for the melt-rate (evolution of depth of pond) and for the shape of the pond (one has to recall that depth of melt-pond is the most important parameter in determining the albedo). Therefore, in the present work, we investigated the behaviour of a model system in which a pure substance initially in the solid state is progressively melted by a horizontal heat source. The melt fluid layer is thermally unstable and quickly develops convective motion of progressively higher intensity as the depth of the melt layer increases. This simple realization of basal-heating driven convective melting allowed thorough analyses of the dependencies of global flow observations, such as the total heat flux and the total kinetic energy, on the varying melt fluid layer depth. It also allowed to reveal the possible links between the flow and the phase-change interface shaped by it.

To start our analysis, we introduced and described the mathematical equation of melting under conduction, which is known as Stefan problem in chapter 3. The analytical solution for the Stefan problem is known and is well described in the first part of chapter 3. The solution of the Stefan problem is later used for validation of numerical computation, and that is the reason we start our discussion with a relatively simple case of conductive melting.

We continued the discussion of conductive melting by applying one more constraint on the flow, moving boundary. Moving boundary in the configuration of melt pond can



be seen as having wind draft on the water-air boundary (top of melt pond). Similar to merely conductive melting, solutions of melting system coupled with moving boundary in conductive regime is also analytically computable, and was used to validate more complicated numerical solutions.

In order to investigate the behaviour of melting system more realistically, as second configuration, we introduced equations describing volumetric heating, which can be interpreted as internal bulk heating of liquid layer through solar radiation.

In the system of melting, when the depth of the liquid layer is large enough, the buoyancy force plays distinct role in the internal dynamics of the melting system. Due to density differences, that stems from temperature differences of near top warm water and cold water in contact with bottom ice, the liquid part of the melting system shows convection. Through this convective behaviour, the heat-budget exchange in the liquid part will increase and more heat will reach the icy bottom of the melt pond. Consequently, one can expect difference in the rate of melting in convective regime.

Due to the nature of equations describing the system of melting, analytical solution for the convective melting system does not exist. However, one can estimate the solution through numerical simulations. Consequently, to continue analysis of the melting system by the mean of direct numerical simulation, we continued the discussion of chapter 3 by introducing the governing equations of system of melting.

In order to extend our primary analysis in conductive configuration, a code has been developed based on the Lattice-Boltzmann method to further investigate the behaviour of melting system in convective regime. However, for the reason of validating the numerical code, we used the existing analytical solutions of conductive mode together with or without moving boundary; and compared our convective setup with previously computed results of other researchers.

In chapter 5, we examined the dynamics of the melting process of a pure solid substance horizontally heated from below under the effect of conduction and natural convection by means of numerical simulations. The analysis has focused on the scaling of global quantities like the heat flux and the kinetic energy at varying control parameters (the effective Rayleigh number Ra_{eff} and the Stefan number St), as well as on the effects linked to space dimensionality. We have conducted an extensive comparison with the paradigmatic Rayleigh-Bénard system in order to gain insight on the possible similarities and differences with its dynamics.

We have shown that CM and RB systems have similar behaviours in terms of the functional dependencies of the (effective) Nusselt and Reynolds numbers on the effective Rayleigh number. The Re_{eff} trends have been found to be almost identical in the CM and RB setups. Concerning the heat flux, Nu_{eff} resulted to be slightly larger in the CM case, but the differences tend to vanish as convection intensity increases (or, equivalently, asymptotically in time); a possible reason for this was identified in the low values of the melting interface speed with respect to the typical fluid velocity fluctuations. Furthermore, similarly to what happens in RB convection, the global heat flux is weaker in 2D than in 3D in the CM setting. Altogether, these findings suggest that, in turbulent conditions, RB phenomenology can provide useful information to give quantitative predictions for CM dynamics and that this is more true for more intense turbulence. These hypotheses, in fact, are already made in geophysical communities, however, the exact re-

lation is not taken into account, and our model shows that we cannot simplify the scaling relation to $1/3$.

Visualizations of the melting front in 3D revealed the appearance of convective patterns with approximately hexagonal, and more often irregular polygonal, cross section. As the Rayleigh number increases, i.e. as the fluid layer grows, such cells undergo a coarsening process. Investigating the morphological properties of the liquid-solid interface with statistical indicators, we found that this is characterized by larger roughness in 3D than in 2D, which can account for the differences detected in the 3D and 2D heat flux behaviours. However, the roughness reaches at most 15% in 3D (respectively 5% in 2D) of the melt height and, independent of the space dimensionality, it further decreases at sufficiently high Rayleigh numbers. Such low values of the melting front roughness again point to strong similarities between the CM and the flat-wall RB systems.

The Stefan number dependency has been mainly investigated in 2D in the range $0.1 \leq St \leq 100$. Although increasing St significantly delays the onset of convection, only quite small differences were observed in the dimensionless global heat flux, notably for high Rayleigh numbers. With rather good accuracy, the heat flux scaling with St was found to be given by a power law of small exponent (0.05) over a broad range of Ra_{eff} values. This result has potentially important consequences for numerical approaches, because it means that it is possible to extrapolate results of high- St fast simulations to small- St conditions that would be otherwise unattainable in direct numerical simulations.

In addition, we addressed the question of the difference between the instantaneous global inflow and outflow in the system, which is connected to the mean temporal variation of the temperature of the fluid. We have shown that such a gap is essentially controlled by a diffusive process and that is more pronounced in systems where the melt process is faster, hence for larger values of the Stefan number.

Finally, we addressed the effect of aspect ratio of the system to the internal dynamics of the flow. We observe that as long as the aspect ratio of the liquid layer is below one, the behaviour of the system is identical. However, for larger aspect ratio the horizontal velocity tends to become more dominant. This effect is mainly due to having periodic lateral boundary in our configuration.

The model analyzed in chapter 5 can be seen as a simple description of ice melt ponds dynamics. In our opinion the present results indicate that the heat flux measured in a corresponding RB system would give a reasonable approximation of the one occurring in a melt pond. Indeed, after the initial phase of the melting process, controlled by conduction, the non-stationary character of the CM system appears to play a minor role, due to the slow motion of the liquid-solid interface. Moreover, for a pond, based on the estimate $St = O(10^{-2})$, the corrugation of its bottom icy wall (the roughness of the top boundary in our model) can be expected to be small. In parallel to the previous observations, this should tend to have a virtually negligible impact after the initial conductive regime.

In chapter 6, we addressed the problem of Convective Melting (CM) coupled with moving boundary condition with different intensities, and for two Stefan numbers. We characterized the wall velocity in dimensionless form by Froude number, which deals with the relationship between gravity and inertial forces. The effect of moving boundary



was well-presented in our simulations; although the intensity of velocities under investigation were relatively small (maximum 3×10^{-4}) with respect to regular speed of winds happening in the Arctic.

We investigated the effect of presence of shear velocity qualitatively as well as quantitatively, and observed that when wall velocity is high enough, which in return causes dominant horizontal kinetic energy. The CM system shows different behaviour in several ways.

First, intensive shear velocity delays the onset of convection and this observation is in qualitative agreement with the behaviour of other similar systems, *e.g.* Couette system. It has been well-known that dominant horizontal velocity field tends to stabilize the system, and prevent transition to convection.

Furthermore, we observed that, velocity of moving wall introduces initial kinetic energy in the system, which can be computed analytically. In addition we observed that there is a direct relation between delay in onset of convection and the magnitude of wall velocity. If the intensity of shear velocity is high enough that initial kinetic energy of the system surpasses what we expect from CM system, the system shows delay in the onset of convection.

Moreover, we observed that, while the Reynolds and the Nusselt numbers at low Rayleigh are different, at ultimate higher Ra such a difference seems to reduce and eventually vanish. This is especially observable in the relative ratio of componentwise average of velocity field (relative ratio of vertical velocity to horizontal one).

In addition, we studied the morphology of the interface for different slip velocities, and we similarly observed direct dependency between intensity of slip velocity and elongation of rolls formation. Moreover, elongated rolls carve less vertically in the solid-liquid interface. Consequently the thickness of melting front reduces by increase in the intensity of slip velocity.

In chapter 7, we addressed the problem of Convective Melting (CM) coupled with internal heating through volumetric bulk heating with different intensities. In our computation, we used constant bulk-heating coefficient instead of considering Beer-Lambert law, which states that the attenuation of light relates to the properties of the material through which the light is traveling. The model presented in this work can be related to the one using Beer-Lambert law by computing depth of the representing melt-pond.

In theoretical section, we presented that Nusselt measured at the solid-liquid interface with respect to Rayleigh has the scaling relation of order $2/3$, where for system of melting without internal heating the scaling reads $1/3$. In fact, the change in scaling relation is a relevant feature and deserves further studies by taking Beer-Lambert law into account.

Moreover, we presented that in the system of melting heated internally at ultimate high Ra heat flux at the melting front approaches marginally to half of the heat flux due to bulk heating. The implication of such dependency is exponential relation of melting-front to the intensity of internal heating. In addition, kinetic energy of the system shows scaling of five-sixth at ultimate high Rayleigh and bulk-heating.

We observed that when bulk heating coefficient is high enough so that vertical kinetic energy due to buoyancy force is dominant, the CM system shows different behaviour. However, while the Reynolds and the Nusselt numbers at low Rayleigh are sim-

ilar to pure convective melting, at ultimate higher Ra the system of melting coupled with bulk heating shows a higher rate of melting.

Furthermore, we presented that in the system of melting heated internally, the velocity of the solid-liquid interface behaves exponentially with respect to magnitude of volumetric bulk heating and Stefan number. This result indicates a new regime, which has not been considered in any large-scale model.

Apart from the internal dynamics of the system, we studied the morphology of the interface for different bulk heating intensity, and we again observed direct dependency between intensity of bulk heating coefficient and vertical elongation of rolls formation.

8.1. Future perspectives

The model of pond that we have considered in this work is highly idealized. However, there are several elements that can increase level of realism. Some of them are easy to be implemented in our framework, whereas others may be more complex. Elements which can be straight-forward to implement are, study of the lateral boundaries and initial pond geometries (for instance cavity).

In the present work, all numerical simulations have been performed with periodic lateral boundary conditions. In order to address the problem of melting more realistically, further analysis of existence of lateral boundary is needed. Additionally in reality, cavities can have complex geometries. However, our preliminary analysis on rectangular and hemispherical shapes shows significant effect on the internal structure of flow in liquid layer and the shape of solid liquid interface (see figure 8.1). In this setup, what is also the important aspect is the distribution of fluxes in horizontal and vertical directions, which has not been addressed in this work.

Another element, which is easy to consider in our model is the temperature of solid. In the present work, temperature of solid has been set to the temperature of melting. In this fashion, the out-going heat is the amount of heat used to transform matter from solid to liquid. However, when the temperature of solid is below melting point, the solid needs to be warmed up to the point of melting, and then the transformation of solid to liquid will take place. It has been observed that temperature of solid has effect on onset of convection [1], however, more analysis is needed to unravel its effects on the internal structure of liquid and solid-liquid interface.

In reality, melt-ponds consist of both fresh and salty water. Salinity level has effect on the density of liquid, and therefore density will be function of both temperature and salinity. Moreover, existence of salt results in formation of brines in solid region, which in advance makes the solid layer porous. Effect of porosity is more observable in first year ice in the Arctic. The process of melting of porous ice results in formation of mushy layer at the melting interface, and may accelerate or decelerate the rate of melting. Further investigation is needed to understand the behaviour of existence of porosity and salinity. (see figure 8.2)

In order to construct large scale models of the type, for instance, Lüthje *et al.*[2], the knowledge about the relation of Nusselt versus Rayleigh, that we have acquired, can be used. In the model of Lüthje *et al.*, there is a term which describes the melt-rate and is considered constant (1cm per day). However, Nusselt-Rayleigh relation allows to have better parametrization of the melt rate. Therefore, results presented in this work can be

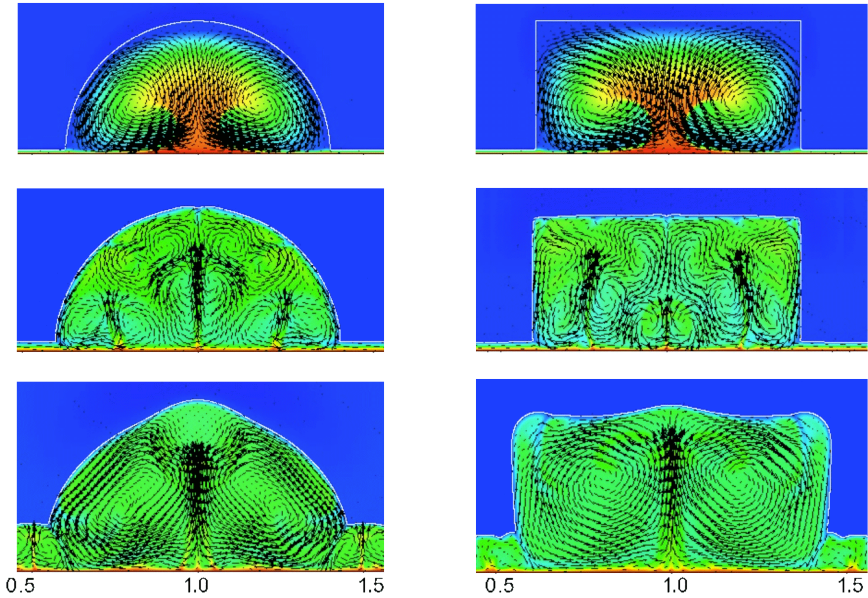


Figure 8.1 – Plot of simulation of melting system with pre-existent cavity. [movie available on demand]

used to provide information on models which are at large scale.

The analysis performed for the system of melting with existence of wind draft and internal heating is in two-dimensional configuration. For the future work, more analysis

8

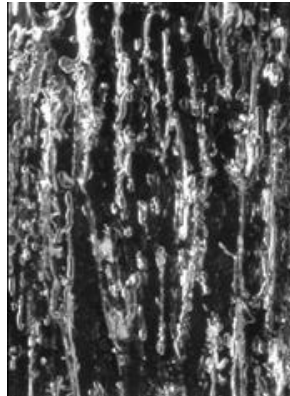


Figure 8.2 – A photograph in natural light showing elongated tubes that form as brine pockets trapped between the ice crystals. The image is 5 millimeters in width. Photo courtesy of Ted Maksym, United States Naval Academy.

is needed for the 3D system of melting coupled with an external moving boundary and bulk heating. Also, we considered constant volumetric heating in our model. However, considering radiation as a function of depth of melt-pond (Beer-Lambert Law) is needed to better understand the behaviour of the system.

Finally, the realistic boundary condition that geophysicists commonly consider for melt-pond system is radiative boundary condition, in which temperature is not imposed, and is dynamically dependent to the height of the melting system. This kind of boundary condition is used in Skillingstad model [3], and implementation of such boundary condition in our model is needed.

References

- [1] S. H. Davis, U. Müller, and C. Dietsche, *Pattern selection in single-component systems coupling Bénard convection and solidification*, *Journal of Fluid Mechanics* **144**, 133–151 (1984).
- [2] M. Lüthje, D. Feltham, P. Taylor, and M. Worster, *Modeling the summertime evolution of sea-ice melt ponds*, *Journal of Geophysical Research: Oceans* **111** (2006).
- [3] E. D. Skillingstad and C. A. Paulson, *A numerical study of melt ponds*, *Journal of Geophysical Research: Oceans* **112** (2007).



A

About the author

Babak Rabbanipour Esfahani has been spending the majority of his life learning and doing research. His research experiences in Fluid Mechanics can be summarized into two important stages in his life; his master program at the University of Groningen in Applied Mathematics, and working as a researcher and PhD student at the University of Lille, France. Through following paragraphs, we try to scratch the surface of his journey over the last six years.

Ten years ago, when he finished his Bachelor, he thought like the majority of the people; start a job, settle down and create a family. He started as a manager at a bank in Iran, which not only was prestigious but also stable and secure. However, something was missing, a sense of curiosity, a passion to learn more. Therefore, he decided to not only continue his education but to do it in another country.

For the Master he managed to receive fund from Nuffic (The Dutch organization for internationalization in education) and started his Master at the University of Groningen in Applied Mathematics. It was during this period that he learned more about fundamentals of fluid mechanics, numerical modeling and governing equations. He learned more about programming, e.g. language C in parallel environment (OpenMPI), and performing post processing using Matlab and Python. Due to the nature of Mathematics programs in the Netherlands, he participated in several courses related to different methods of discretizing continuous equations, e.g. Navier-Stokes and Maxwell, from the universities of Groningen, Utrecht and TU Delft.

For the final thesis of his Master, he dedicated eight months working on none-linear stability of plane Poiseuille flow in periodic condition. The model was created in Matlab environment and consisted of several parts for computing steady state and stability of the plane Poiseuille flow. The method that he used for this modeling was Finite Difference Method (FDM) and Arclength for traveling along steady curve. Global parameters of interest were traveling waves, wavenumber, and Reynolds number. Due to the necessity of accuracy and resolving small scale dissipating energy (Kolmogorov scale) for stability analysis, the model constructed over large scale non-uniform mesh, and was run over 32 processors.



After finishing his Master, he received another fund from National Research of France (ANR) and started his PhD working on melt-ponds in the Arctic during summer time (melting due to thermal convection) based on the Lattice-Boltzmann method. To perform numerical simulation, he co-developed a fully parallel program using C in Open-MPI which was tested on 1024 processors and its efficiency has been well observed. Besides the numerical simulation, analytical analysis on the onset of convection showed interesting promises and was in good agreement with numerical outcome. The global parameters of interest were Stefan number (rate of melting), Rayleigh number and aspect ratio of the system. Additionally, similarity between the melting system and the Rayleigh-Bénard system for high Rayleigh number and dependency on Stefan number has been observed, and the publications of results are in progress.

The doctoral program is near the end (March 2018) and for the next stage, he likes to continue gaining more experience by participating in research programs as post-doctor. Having worked on large scaled systems, especially handling simulations related to fluid mechanics and having sufficient knowledge about numerical methods, along with good knowledge of programming in C, Fortran, Python and Matlab; he is well-prepared to step up and work as a researcher.



Scientific Contributions

Publications:

Year	Title	State
2018	Basal melting driven by turbulent thermal convection	Under consideration for publication on <i>Physical Review Fluid</i> (arXiv:1801.03694)
	Convective melting with a moving boundary	in preparation
	Convective melting coupled with volumetric bulk heating	in preparation

Conferences:

Year	Title	Conference
12/9/2016	Melting from below driven by thermal convection	11 th European Fluid Mechanics conference, Seville, Spain
16/8/2017	Dynamics of turbulent melting from below driven by thermal convection	Turbulent Mixing and Beyond, Trieste, Italy

Oral presentations:

Year	Title	Place
2015	Evolution of Sea Ice in Arctic During Summers	Journée des Doctorants, Université d'Artois
2015	Melting process of Sea Ice in Arctic	Laboratoire de Mécanique de Lille
2016	Melting driven by thermal convection	Journée des Doctorants, Ecole des Mines de Douai

Oral presentations by co-authors:

Year	Title	Conference
1/3/2017	Melting driven by turbulent thermal convection	Dynamics of Interfaces in Complex Fluids and Complex Flows, Erlangen, Germany
14/5/2018	Basal melting driven by turbulent thermal convection	International conference of Rayleigh-Bébard turbulence, Enschede, the Netherlands



Avenue Paul Langevin
59650 Villeneuve-d'Ascq
France

+33 (0)7 83 04 02 36

✉ rabbanipour@hotmail.com

🌐 <https://www.linkedin.com/in/rabbanipour/>



Babak Rabbanipour Esfahani

Education

- 2015–2018 **PhD in Mechanical Engineering**, *Université Lille 1 - Sciences et Technologies*, Lille, France.
- 2011–2013 **MSc Applied Mathematics**, *Rijksuniversiteit Groningen*, Groningen, the Netherlands.
Major: Computational Science and Numerical Mathematics
- 2000–2004 **BSc Applied Mathematics**, *University of Isfahan*, Esfahan, Iran.
Major: Numerical Analysis and Image processing
- 1997–2000 **High-school Diploma**, *Harati High School*, Esfahan, Iran.
Passed with distinction

PhD thesis

- title *Turbulent convection and melting process with applications to sea ice melt ponds*
- supervisors Mohamed-Najib OUARAZI, Enrico CALZAVARINI, Silvia HIRATA
- description Melting and solidification coupled with convective flows are fundamental processes in the geophysical context. A key question related to these phenomena is the prediction of the evolution of the melting-rate, a quantity that is tightly connected to the heat-flux dynamics at the liquid-solid interface. In order to shed light on this process and in particular on its scaling laws, we study here the stages of the dynamics of a model system.

Master thesis

- title *Stability Analysis of 2D Poiseuille Flow*
- supervisors Fred WUBS
- description Computing various Hopf bifurcations in the two-dimensional plane Poiseuille problem, for several values of the wavenumber α . We obtain the branch of periodic flows which are born at the Hopf bifurcation of the laminar flow.

Scientific Contributions

Publication

- 2018 **Basal melting driven by turbulent thermal convection**, *Phys.Rev.Fluids*, under review.
Convective melting with a moving boundary, *in preparation*.
Convective melting coupled with volumetric bulk heating, *in preparation*.

Conferences

- 12/09/2016 **Melting from below driven by thermal convection**, *11th European Fluid Mechanics conference*, Seville, Spain.
- 16/08/2017 **Dynamics of turbulent melting from below driven by thermal convection**, *Turbulent Mixing and Beyond*, Trieste, Italy.

Oral Presentations

- 2015 **Evolution of Sea Ice in Arctic During Summers**, *Journée des Doctorants*, Université d'Artois.
- 2015 **Melting process of Sea Ice in Arctic**, *Laboratoire de Mécanique de Lille*.
- 2016 **Melting driven by thermal convection**, *Journée des Doctorants*, Ecole des Mines de Douai.

Experiences

Vocational

- 2015–2018 **Research Assistant**, *Université Lille 1 - Sciences et Technologies*, Villeneuve d'Ascq.
Main Duties:
- Code developing and analyzing Convection melting;
 - Data analyzing using Matlab and Python;
 - Advising students at bachelor level.

Researches

- Linear and non-linear stability analysis of convection with phase change
- Lattice Boltzmann method for simulating fluid behavior and melting process
- 2D Simulating Navier-Stokes equations in Matlab by discretizing with FVM
- Simulation of water behavior by SPH method in 3D
- Simulation of collision of waves by SPH in 3D
- Bifurcation analyze of Navier-Stokes equations with periodic boundary conditions
- Simulating Maxwell's equations by FEM and BEM
- Ability to program by "Visual C++" and "Visual Basic"
- Using Computer Processing Unit for large scaled system of equations
- Ability to use "DirectX", "OpenGL", and "CUDA" platforms
- Research in image processing by the mean of Matlab
- Several years experience of working in Windows and Linux environments

Skills

Development

Languages, C, C++, Fortran, Python.

Parallel Programming, OpenMPI, MPICH, CUDA, OpenGL.

Operating Systems, Windows, Linux, Mac OS.

Interests and hobbies

Reading novels, Solving puzzles, Swimming, Hiking

Languages

English **Fluent**
Persian **Fluent**
French **Basic**
Dutch **Basic**
German **Basic**

IELTS 7
Mother tongue
Level A1
Level A1
Level A1

References

- **Prof.Mohamed-Najib OUARZAZI**

Laboratoire de Mécanique de Lille
Université de Lille 1
najib.ouarzazi@univ-lille1.fr
tel: +33(0)6 89 56 73 81

- **Dr.Enrico CALZAVARINI**

Laboratoire de Mécanique de Lille
Université de Lille 1
enrico.calzavarini@polytech-lille.fr
tel: +33(0)3 28 76 73 73

- **Dr.Silvia Hirata**

Laboratoire de Mécanique de Lille
Université de Lille 1
silvia.hirata@univ-lille1.fr
tel: +33(0)3 20 43 65 39